NASA Contractor Report 152174

Investigation of Impingement Region and Wall Jets Formed by the Interaction of High Aspect Ratio Lift Jets and a Ground Plane

D.R. Kotansky and L.W. Glaze

McDonnell Aircraft Company
McDonnell Douglas Corporation
St. Louis, Missouri

Prepared for
Ames Research Center
under Contract NAS2-9646

NASA
National Aeronautics and
Space Administration

1978

1. Report No. NASA CR-152274	2. Government Accession No.	3. Recipient's Catalog No.

4. Title and Subtitle Investigation of Impingement Region and Wall Jets Formed by the Interaction of High Aspect Ratio Lift Jets and a Ground Plane	5. Report Date 19 September 1978
	6. Performing Organization Code
7. Author(s) Donald R. Kotansky Lloyd W. Glaze	8. Performing Organization Report No.
	10. Work Unit No.
9. Performing Organization Name and Address McDonnell Aircraft Company P.O. Box 516 St. Louis, Missouri 63166	11. Contract or Grant No. NAS2-9646
	13. Type of Report and Period Covered Final Technical 9/19/77 - 9/19/78
12. Sponsoring Agency Name and Address National Aeronautics and Space Administration AMES Research Center Moffett Field, California 94035	14. Sponsoring Agency Code

15. Supplementary Notes

16. Abstract

An experimental investigation was conducted of the flow field characteristics of impinging turbulent jets emanating from rectangular exit area converging nozzles of exit area aspect ratio four, six and eight. The primary emphasis was placed on the determination of the azimuthal distribution of the radial momentum flux of the wall jet about the impingement region of single jets. The measured azimuthal distributions of wall jet radial momentum flux in the ground plane were found to be strongly directional and sensitive to rectangular nozzle exit area aspect ratio, jet impingement angle and height above ground, H/D. In addition to the basic investigation of impinging rectangular jets, the effects of jet exit velocity profile non-uniformities were investigated, and a limited number of dual nozzle (two jet) jet impingement flow field investigations were conducted.

The data obtained from the single nozzle rectangular jet impingement investigations were incorporated into an existing VTOL aircraft ground flow field computer program. This provides an extended jet impingement data base for the computation of ground flow fields which was previously based solely on the impingement characteristics of round jets. This computer program together with the Douglas Neumann program modified for V/STOL applications may be used for the analysis and prediction of flow fields and resulting forces and moments on multi-jet V/STOL aircraft hovering in ground effect.

17. Key Words (Suggested by Author(s)) V/STOL Ground effects Jet impingement Non-axisymmetric jets	18. Distribution Statement

19. Security Classif (of this report) Unclassified	20. Security Classif (of this page) Unclassified	21. No. of Pages 85	22. Price

FOREWORD

This report was prepared by the Aerodynamics Department of the McDonnell Aircraft Company (MCAIR), St. Louis, Missouri, for the Ames Research Center of the National Aeronautics and Space Administration. The objectives of the study were to investigate experimentally certain characteristics of impinging turbulent jets emanating from rectangular exit area nozzles of high aspect ratio and to incorporate the experimental results into a VTOL ground flowfield computer program developed originally for the Naval Air Development Center. Specifically, the primary data required were the azimuthal distributions of turbulent wall jet radial momentum flux about the impingement region of the rectangular jets. The inclusion of these data into the ground flowfield computer program provides an extended jet impingement data base for the computation of ground flow fields which was previously based solely on the impingement characteristics of round jets. This computer program together with the Douglas Neumann program modified for V/STOL applications may be used for the analysis and prediction of flow fields and resulting forces and moments on multi-jet V/STOL aircraft hovering in ground effect.

The principal investigator of this study was Dr. Donald R. Kotansky of the McDonnell Aircraft Company Aerodynamics Department. The NASA Ames technical monitor was David G. Koenig of the Large Scale Aerodynamics Branch of the Flight Systems Research Division.

TABLE OF CONTENTS

LIST OF TABLES

LIST OF ILLUSTRATIONS

LIST OF ILLUSTRATIONS (Continued)

NOMENCLATURE

D	Rectangular nozzle exit width
E	Voltage
ΔE	Voltage difference ($E_2 - E_1$) between HFA channels 1 and 2
$f(\phi)$	Momentum distribution about jet impingement region
H	Nozzle exit height above ground
HFA	Hot film anemometer
L	Rectangular nozzle exit length
L/D	Rectangular nozzle exit area aspect ratio
$\dot{M}$	Momentum flux
$\dot{m}$	Mass flow
N	Normal distance above ground plane
NPR	Nozzle pressure ratio
P	Pressure
R	Radius measured from real or apparent jet impingement point
Re_D	Reynolds number based on rectangular nozzle exit width, $Re_D = \frac{V_{je} D \rho}{\mu}$
S	Nozzle exit centerline spacing between long axes
T	Temperature
U	Wall jet velocity
V	Jet velocity
V_∞	Freestream velocity
X,Y,Z	Cartesian coordinates
Z	Jet centerline coordinate
α_j	Jet impingement angle measured in pitch (rotation about short nozzle exit axis, see figures 1 and 34)
θ_j	Jet impingement angle measured in roll (rotation about long nozzle exit axis, see figures 1 and 43)

ρ	Density
ϕ	Azimuthal angle measured around periphery of jet impingement region. For $\alpha_j \neq 90°$ or $\theta_j \neq 90°$, $\phi = 0°$ in direction of horizontal component of jet mean flow (see figures 1, 34 and 43)
ψ	Wall jet flow angularity with respect to a radial line through the jet impingement point

Subscripts

1,2	Anemometer channels
amb	Ambient conditions
e	Jet exit station
j	Jet
max	Maximum value
N	Nozzle
p	Probe
T	Total properties
1/2	Half-velocity point

INVESTIGATION OF IMPINGEMENT REGION AND WALL JETS FORMED BY THE INTERACTION OF HIGH ASPECT RATIO LIFT JETS AND A GROUND PLANE

DONALD R. KOTANSKY AND LLOYD W. GLAZE

SUMMARY

An experimental investigation was conducted of the flow-field characteristics of impinging turbulent jets emanating from rectangular exit area converging nozzles of exit area aspect ratio four, six and eight. The primary emphasis was placed on the determination of the azimuthal distribution of the radial momentum flux of the wall jet about the impingement region. Both vertical and oblique impingement were investigated for various values of the ratio of height above ground to nozzle exit width, H/D. The oblique impingement conditions included simulated nozzle rotations about the short axis of the nozzle exit opening (pitch) and also about the long axis of the nozzle exit opening (roll). However, simultaneous combinations of pitch and roll were not investigated. The measured azimuthal distributions of wall jet radial momentum flux in the ground plane were found to be strongly directional. They were found to be sensitive to rectangular nozzle exit area aspect ratio, jet impingement angle and height above ground, H/D.

Reynolds number effects were investigated by determining the non-dimensional shape of the wall jet velocity profiles for fixed test conditions while varying only the Reynolds number (nozzle pressure ratio) over a range of low nozzle pressure ratios to avoid compressibility effects. The jet exit Reynolds number range investigated was from 146,000 to 275,000 based on the rectangular nozzle exit width. Reynolds number effects were found to be insignificant over this range. The effects of a flow spoiler inserted in the exit plane of the aspect ratio four nozzle were investigated over a limited range of jet impingement test conditions to identify the possible influence of jet exit velocity non-uniformities on the azimuthal distributions of wall jet radial momentum flux. These effects, also, were

found to be insignificant.

Additional measurements of azimuthal distributions of wall jet radial momentum flux were conducted for rectangular nozzle pairs of exit area aspect ratio eight which produced dual jets impinging vertically for two values of the height above ground to nozzle width ratio, H/D. This was accomplished for three values of nozzle exit centerline spacing (between the long axes of the nozzle exit openings) ratioed to nozzle exit opening width. The selected combinations of jet exit spacing, S/D, and height above ground, H/D, that were investigated resulted in no significant merging of the jets prior to ground impingement. A significant flux of wall jet radial momentum in the ground plane was identified along the ideal stagnation line formed by the interaction of the two jet flows for these cases.

INTRODUCTION

Recent studies have revealed the complexity of the viscous flowfield produced by the multiple lift jet systems of V/STOL aircraft in ground effect. Test data have shown the sensitivity of the net forces and moments acting on the vehicle to the geometry of the airframe and the propulsive lift jet system in combination with the ground surface. A number of recent studies have been directed specifically at the development of engineering methodologies for the prediction of induced forces and moments on arbitrary multi-jet V/STOL aircraft both in and out of ground effect. Pertinent recent work in these areas is summarized in a "V/STOL Aerodynamic Technology Assessment" published by the Naval Air Development Center (NADC), reference 1.

Most of the experimental and analytical work to date has been concerned with multi-jet flows emanating from axisymmetric (round) nozzles, since these types of nozzles have been associated with CTOL and V/STOL aircraft historically. Only recently has serious effort been expended on the design and development of non-axisymmetric nozzles. This is largely a result of investigations of potential benefits associated with the substitution

of non-axisymmetric nozzles for round nozzles in CTOL and lift-plus-lift-cruise V/STOL aircraft propulsion systems and the direct requirement for rectangular nozzles in certain STOL and VTOL systems such as upper surface blowing and thrust augmenting ejector systems. The work described herein expands a needed empirical data base on turbulent jet impingement characteristics from that currently available for round jets to rectangular exit area jets of aspect ratio four, six and eight.

The computation and prediction of the viscous (turbulent) flowfield between a multi-jet V/STOL aircraft and the ground is strongly dependent on the mean structure (geometry) of the flows in the turbulent jets. The significant jet mean flow geometry and overall flowfield geometry includes:

- o The two dimensional mean velocity distribution at the nozzle exit, $V_{je}(X_N, Y_N, Z_N = 0)$ (this specification includes nozzle exit shape);
- o Lift jet system arrangement including the number of jets, jet exit spacings and jet exit orientation with respect to the aircraft axes (including vector and splay angles); and
- o Aircraft orientation and height above ground.

Most of the above geometric variables were taken into account in the development of a ground flowfield prediction computer program by the McDonnell Aircraft Company for NADC which is described in detail in reference 2. However, this work was based on the fundamental free jet flow development and impingement characteristics of round jets which, for the most part, were available in the published literature. Specifically, the free jet entrainment data of Kleis and Foss (reference 3) and the geometric and kinematic properties of free and impinging round jets established by Donaldson and Snedeker (reference 4) were utilized extensively. The data of Donaldson and Snedeker were also utilized to determine required analytical expressions for wall jet entrainment.

A key element in the modelling of the ground surface flowfield below a hovering V/STOL aircraft is the local distribution of momentum flux about the individual jet impingement points on the ground plane. The data of Donaldson and Snedeker show that this distribution for a round turbulent jet is sensitive to the jet impingement angle and relatively insensitive to the ratio of height above ground to nozzle exit diameter (H/D). These distributions of momentum flux together with the magnitudes of the total momentum fluxes emanating from the nozzle exits establish the location and (momentum) strength of the fountains in the flowfield below the aircraft.

The primary purpose of this study was to determine experimentally the azimuthal distributions of wall jet radial momentum flux about the impingement points of high aspect ratio rectangular jets as a function of nozzle exit area aspect ratio, jet impingement angle and nozzle exit height above ground. Additionally, Reynolds number effects, non-uniformities in rectangular jet exit velocity profiles and dual nozzle impingement including jet exit spacing effects were investigated.

This data base for high aspect ratio rectangular nozzles was then incorporated into the ground flowfield computer program originally developed for round jets for NADC and delivered to NASA Ames. This computer program together with the Douglas Neumann potential flow program modified for V/STOL applications (reference 5) may then be used in the analysis and prediction of induced forces and moments on multi-jet V/STOL aircraft hovering in ground effect as described in reference 2.

EXPERIMENTAL TEST PROGRAM

The experimental test program was designed to provide data on the rectangular nozzle free jet characteristics and jet impingement characteristics over a meaningful range of pertinent parameters associated with the operation of a V/STOL aircraft in the hover mode in ground effect. The baseline nozzle configuration and test parameter variations are summarized in table 1. The purpose of the free jet surveys was primarily to establish

the quality of the flow emanating from the high aspect ratio rectangular nozzles in terms of velocity profile shape and flow symmetry achieved. Reynolds number effects were investigated by determining wall jet velocity profiles for a fixed set of flow geometry while varying only nozzle pressure ratio at low pressure ratio levels to avoid the effects of compressibility.

The desired wall jet momentum flux distributions about the rectangular jet impingement points were established by surveying the turbulent wall jet velocity profiles about the periphery of the jet impingement region for vertical and oblique jet impingement. In the oblique impingement experiments, pure pitch (about the nozzle exit short axis) and pure roll (about the nozzle exit long axis) were investigated, but combinations of pitch and roll were not investigated. In the case of vertical impingement, one quarter of the periphery was surveyed since two planes of flow symmetry existed, and in the case of oblique jet impingement, one half of the periphery was surveyed since in this case only one plane of symmetry existed. The wall jets were surveyed at 15° increments in azimuth (ϕ) over the region of interest about the jet impingement point. Figure 1 defines the geometry and the coordinate systems for the jet impingement tests. It should be noted that the rectangular exit area nozzle width, D, was a fixed physical dimension of 2.0 cm. for all nozzles throughout the test program.

Nozzle exit flow velocity profile non-uniformities and their effect on the azimuthal distribution of wall jet radial momentum flux about the rectangular jet impingement point were investigated with the aspect ratio four nozzle at the lowest height above ground (H/D = 2), for both vertical and oblique jet impingement. The flow non-uniformity was produced by placing a circular rod (0.47 cm. diameter) along the long axis of the aspect ratio four nozzle at the center of the nozzle exit plane. Free jet profiles were determined with the flow disturbance in place to quantify the extent of the velocity profile non-uniformity produced. Wall jet surveys were then conducted to identify the effects of the flow disturbance on the wall jet momentum distributions.

The final segment of the test program consisted of surveys of wall jet momentum flux distributions about the impingement region of pairs of aspect ratio eight rectangular jets. This was accomplished for three values of nozzle exit spacing between the nozzle exit long axes (S/D = 4, 6, 8) with vertical impingement of both jets for two values of height above ground (H/D = 2, 8). The flowfield surveys obtained during the test program are summarized in table 2.

TEST FACILITIES, HARDWARE AND INSTRUMENTATION

Test Facilities

Test operations were conducted utilizing the multiple jet interaction test apparatus of the Inlet Simulator (IS) test cell, which is a part of the McDonnell Aircraft Company (MCAIR) Propulsion Subsystem Test Facility (PSTF). The PSTF was designed and developed specifically to allow a wide range of exploratory static testing to be accomplished rapidly and economically. The facility utilizes high pressure (4137 kP_a) air, sharing the air storage system of the MCAIR Polysonic Wind Tunnel and vacuum sources of low pressure facilities.

The jet interaction test apparatus utilizes the pressure control system of an adjacent PSTF test cell to set, and automatically hold, nozzle pressure ratio. Two 48.3 cm. ID settling chambers are supplied with high pressure air to provide uniform flow to the nozzle plenums. The settling chambers have conical and normal screens. The nozzle plenums are "D" shaped with the flat side toward the test model. The plenums are provided with two internal screens and removable nozzle mounting plates that are compatible with various nozzle configurations. A special nozzle mounting plate was fabricated for this test to accommodate the three, high aspect ratio rectangular nozzles. In addition, this nozzle mounting plate provided the capability of setting three nozzle centerline spacings (S/D = 4,6,8) for the dual nozzle configurations through the use of appropriate spacer plates.

Nozzles

Five, high aspect ratio, rectangular nozzles were fabricated for this test. The nozzles were constructed of fiberglass which was permissible because of the low nozzle pressure ratios selected for the test program. Three of these nozzles, shown schematically in figure 2 (L/D = 4,6,8), were used for the single jet configurations and had internal flow area contraction ratios of 10.00, 8.33 and 7.50 respectively. The two nozzles (L/D = 8) used for the dual jet configurations in which the effects of jet spacing were investigated had internal flow area contraction ratios of 3.96. Photographs of the nozzles are shown in figures 3 and 5. The aspect ratio four nozzle shown in figure 3 is shown with the nozzle exit flow spoiler in place. Details of the flow spoiler installation are shown schematically in figure 4. The aspect ratio eight and six single nozzles and the aspect ratio eight dual nozzle pair are shown in figure 5. The individual nozzles in the nozzle pair used for the jet spacing investigation were structurally reinforced with a fiberglass ring around the periphery of the converging section near the nozzle exit as can be seen in figure 5.

Ground Board

A 150 cm. diameter, circular ground board, fabricated from aluminum, was used to simulate the ground plane. The ground board was mounted on a motor driven, rotational bearing which allowed for 360° azimuthal (ϕ) rotation. In addition, the bearing was mounted on a gimballed frame affixed to a movable cart with which variations in ground board height, H/D, could be established. The gimballed frame made possible jet impingement pitch angles, α_j, of 60°, 75° or 90° (see figure 6). With a 90° rotation of the base of the gimballed frame on the cart, ground board roll angle, θ_j, settings of 60°, 75° or 90° were obtainable. Use of the gimbal system permitted changes in ground board pitch and roll angle while maintaining the center of the ground board coincident with the jet centerline as projected from the fixed nozzle exit location which was

established by the plenum and support system. Height above ground was defined as the distance from the center of the nozzle exit to the ground plane measured perpendicularly to the ground plane.

In making a wall jet velocity profile survey, a two component hot film anemometer probe was traversed through a .508 cm. hole in the ground board, in a direction normal to its surface, using a remotely controlled, one degree-of-freedom, probe traverse device. This probe drive device was mounted on the back of the ground board adjacent to the five radial hole positions (R/D = 6.5, 14.0, 21.5, 29.0, 36.5). The five holes were located at five different azimuthal positions on the ground board with a 72° azimuthal spacing between radial positions as shown in figure 6. This was done to prevent any flow disturbance from an upstream hole on a downstream measurement station.

Hot Film Anemometer

The free jet and wall jet velocity profile surveys were accomplished with two component, directionally sensitive hot film anemometer probes. The selected probe configuration was the Thermo-Systems Model 1240-20 "Cross-Flow" probe used in conjunction with a two-channel Thermo-System Model 1050-2C anemometer unit. The plane of the sensor cross was parallel to the ground board resulting in the measurement of velocity and flow direction in the R, ϕ plane. Angularity was sensed with respect to the local ϕ = constant reference at the five ground board hole positions. The local angularity zeroing technique for the probe sensors is discussed in the Data Acquisition section. A total of four dual sensor "Cross-Flow" probes were consumed during the experimental test program; two probes were lost to identifiable electrical malfunctions and two were lost due to identifiable mechanical damage.

All probes were calibrated for mean flow velocity and flow angularity in a modified Thermo-Systems Model 1125 Calibrator. Angularity data were obtained with the calibrator supported on a manually adjusted turntable which allowed the calibrator to be rotated about the probe support axis. The zero angularity reference position for each probe was established by nulling out the

difference between the two sensor outputs at a selected mean velocity level. Calibrations were performed at an anemometer overheat ratio of 1.5 for mean velocities in the range of 0 to approximately 90 m/sec and for yaw angularity, ψ, of $\pm 25°$ at four selected mean flow velocity magnitudes. A set of actual mean flow and yaw angularity calibration curves are shown in figures 7 and 8 for probe no. B576. These calibration curves were fit with polynomial expressions for inclusion in the data reduction program.

DATA ACQUISITION AND REDUCTION

Data Acquisition

Hot film anemometer probe sensor outputs and the probe sensor position potentiometer output were recorded on magnetic tape by the PSTF data acquisition system as the probe was traversed through the free jets and the wall jets for each test condition. The data acquisition system (DAS) is shown schematically in figure 9. The DAS scanned all data channels continuously at a scan rate of ten scans per second. The anemometer output signals were filtered with a low pass filter to 2 Hz. Probe data were recorded continuously for two second intervals at the rate of twelve data intervals per minute during all traverses. The traverse rate was preset on the remote control unit of the traverse drive motor and varied from approximately 3 to 8 cm.. per minute depending on the wall jet thickness. For the wall jet surveys, the traverses were begun slightly below the ground plane level and continued through the wall jet until the anemometer output reached a preselected minimum level. In addition to recording the hot film anemometer output and probe position on the PSTF DAS, an on-line X-Y-Y plotter was wired into the test instrumentation system to provide graphical displays of both channels of anemometer output as a function of probe position. Both types of data recording were used for all velocity profile surveys in the test program. The X-Y-Y plotter output allowed on-line monitoring of the quality and repeatability of the data.

Prior to each azimuthal (ϕ) sweep series of velocity profile surveys, the anemometer bridge was balanced to insure compatibility with the overheat ratio of the hot film probe calibration performed prior to the test. Since changes in flow temperature affect the probe output, it was periodically monitored throughout each series of runs, and the anemometer bridge was rebalanced if a significant temperature change was indicated. To further check the quality of the data recorded, the first survey of an azimuthal sweep series was repeated at the end of the series (and, in some cases, a whole series of runs was repeated) to insure the repeatability of the hot film data.

In order to properly align the anemometer probe with the flow, the probe calibration chamber was mounted to the circular ground board such that the chamber centerline coincided with a radial line connecting the ground board center with the probe center. With the anemometer probe extended through the ground board and aligned with the calibration chamber nozzle flow, conditions corresponding to a point on the mean velocity calibration curve were reproduced, and the probe was rotated until no voltage difference was indicated between the two channels of the anemometer, indicating zero flow angularity. This procedure was followed each time the probe was moved to a new radial station.

Data Reduction

The wind tunnel test data reduction program is shown in block diagram form in figure 10. The data reduction program, executed on the CDC Cyber 175 computer, summed and averaged each two second interval of data scans to produce single point hot film anemometer and probe position data. The averaged hot film data were then input to the calibration curves with the resulting output being mean velocity and yaw angularity. The program also integrated the velocity and velocity squared profiles using the trapezoid rule with the upper limit of integration (N_1) predetermined as a common value for each run in an azimuthal sweep series. These integrated values were then used in the calculation of wall jet mass flow, $\dot{m}$, and wall jet momentum flux, $\dot{M}$, as follows:

$$\frac{\dot{dm}}{d\phi} = \rho \int_{N=0}^{N_1} U \quad RdN$$

$$\frac{\dot{dM}}{d\phi} = \rho \int_{N=0}^{N_1} U^2 RdN$$

Additional data output by the data reduction program included nozzle configuration, nozzle height above the ground board (H/D), jet impingement angle (α_j or θ_j), nozzle pressure ratio (NPR), probe radial position (R/D), ground board azimuthal angle (ϕ), and ambient temperature (T_{amb}) and pressure (P_{amb}).

EXPERIMENTAL RESULTS

The objectives of the experimental test program were discussed in the section entitled Experimental Test Program. The test was conducted in six phases corresponding to the six major items in table 1. The results of the experimental investigation will be presented in that same order largely through the presentation of plots of the experimental test measurements.

Free Jet Characteristics

Free jet surveys were performed to investigate the shape of the velocity profile produced at the nozzle exit and to examine the symmetry of the jet flows. Velocity profile surveys were obtained for the test conditions given in table 1 under Free Jet Characteristics. In all cases, the velocity profile data indicated acceptable nozzle exit flow conditions. Figures 11 and 12 present the jet exit velocity profiles for the aspect ratio four and eight rectangular nozzles. Data are presented at four positions (X_N/L) across the nozzle exit plane from the nozzle midplane ($X_N/L=0$) to the edge of the nozzle ($X_N/L=0.50$). A slight non-uniformity in velocity level is noted in the aspect ratio eight nozzle (internal contraction ratio of 7.50) at the X_N/L = 0.17 survey position. The effects of the turbulent shear stress on the edge of the velocity profile (at the $X_N/L=0.50$ survey position) can be clearly seen in both figures 11 and 12.

Reynolds Number Effects

Reynolds number effects were investigated by determining the characteristic shape of the wall jet non-dimensional velocity profiles for a constant set of parametric test conditions while only the Reynolds number (nozzle pressure ratio) was varied. Three Reynolds numbers were investigated: 146,000; 205,000 and 275,000 corresponding to nozzle pressure ratios, NPR, of 1.07; 1.15 and 1.28. Figures 13, 14 and 15 present non-dimensional wall jet velocity profiles for the aspect ratio six nozzle at H/D = 8.0. These data were measured at R/D = 14.0 and ϕ = 0° which corresponded to a radial position in the ground plane that was perpendicular to one of the short sides of the rectangular exit area nozzle. Figures 16, 17 and 18 show similar data for the ϕ = 90° position (in a radial direction in the ground plane perpendicular to one of the long sides of the nozzle exit). Figures 19 through 24 show a similar set of data for the same nozzle and test conditions with the velocity profiles obtained at the R/D = 29.0 radial position. From these data and corresponding data on the aspect ratio four and eight nozzles, it was concluded that no significant Reynolds number effects were present. This result is consistent with the observations of Ricou and Spalding, reference 6, who noted that for free jet exit Reynolds numbers in excess of approximately 30,000, flow characteristics were insensitive to Reynolds number.

Vertical Impingement

The basic characteristics, including azimuthal distributions of wall jet radial momentum flux, for vertically impinging jets emanating from rectangular exit area nozzles of aspect ratio four, six and eight were obtained for the test conditions given in table 1. Figures 25 through 33 present the azimuthal distributions of wall jet radial momentum flux measured in this phase of the test program. On each curve, the independent variable is the azimuthal angle, ϕ, over a range of one quarter of the jet impingement region periphery from a perpendicular to a short nozzle side at ϕ = 0° to a perpendicular to a long nozzle side at ϕ = 90° in the ground plane. The measurements at radial stations R/D = 14.0 and R/D = 29.0 are presented.

The data in figures 25 through 33 clearly indicate that the preferential direction of momentum flux is perpendicular to the long side of the rectangular nozzle exits, and that this directional bias is a function of H/D decreasing with increasing H/D. However, even at H/D = 16, this preferential direction is still present indicating that the impinging free jets were strongly non-axisymmetric even for the lowest aspect ratio. Most of the data show a decrease in the magnitude of the radial momentum flux with increasing R/D from R/D = 14.0 to R/D = 29.0.

Oblique Impingement

The azimuthal distributions of wall jet radial momentum flux for oblique impingement are shown in figures 34 through 42 for oblique impingement caused by rotation about the short axis of the nozzle exit (pitch) and in figures 43 through 51 for oblique impingement caused by rotation about the long axis of the nozzle exit (roll). In these figures, the independent variable is the azimuthal angle, ϕ, over a range of one half of the jet impingement region periphery. For the pitch data (figures 34-42) the angles $\phi = 0°$ and $\phi = 180°$ correspond to directions perpendicular to the short sides of the nozzle exit, with $\phi = 0°$ corresponding to the direction of the horizontal component of the free jet mean flow (see insert in figure 34). For the roll data (figures 43-51) the angles $\phi = 0°$ and $\phi = 180°$ correspond to directions perpendicular to the long sides of the nozzle exit, with $\phi = 0°$ corresponding to the direction of the horizontal component of the free jet mean flow (see insert in figure 43). The parametric variable on each figure is the pitch or roll impingement angle in each case except for figures 42 and 51. Figures 42 and 51 present the effects of parametric variations of nozzle aspect ratio on the momentum flux distributions for $\alpha_j = 60°$ (pitch) and $\theta_j = 60°$ (roll) respectively.

The strong influence of oblique impingement in both pitch and roll cases is clearly evident from these figures. In pitch, the largest fraction of momentum flux appears in a ϕ direction approximately coincident with the magnitude of the impingement angle, and all significant flux of momentum occurs within the

range of $\phi = 0°$ to $\phi = 120°$ of the impingement region periphery. The exact location of the momentum flux peak in the pitch investigations, especially at H/D = 2 and 4, is somewhat uncertain, since the wall jet profiles were obtained at fixed intervals of 15° in azimuth. The roll data indicate strong distributions of momentum flux in the sectors of azimuth adjacent to perpendiculars to the long sides of the nozzle exit ($\phi = 0°$ and $\phi = 180°$), with the strongest momentum flux occurring at the $\phi = 0°$ position as would be expected based on the simplest flow deflection model.

Velocity Profile Effects

Exit velocity profile non-uniformities were created by affixing a flow spoiler to the nozzle exit plane of the aspect ratio four nozzle, as shown in figures 3 and 4. Two flow spoilers were considered: a 0.51 cm (0.20 in.) metal bar and a 0.47 cm (3/16 in.) metal rod. The rod was chosen because it created a more symmetrical velocity depression. Wall jet surveys were obtained for this configuration at one nozzle height above ground (H/D = 2.0), two radial stations (R/D = 6.5, 14.0) and for both vertical ($\alpha_j = \theta_j = 90°$) and oblique impingement ($\alpha_j = 60°$, 75°; $\theta_j = 60°$, 75°) at ten azimuthal stations in the vicinity of the velocity depression. Surveys of the magnitude of the velocity profile non-uniformity created in the free jet were also conducted. At an axial station of one nozzle width downstream of the aspect ratio four nozzle exit ($Z_N/D = 1.0$) a velocity depression of 89 m/sec out of a maximum of 149 m/sec was measured. This depression mixed out of the jet very rapidly, and at $Z_N/D = 4.0$, a central flat profile had formed with a velocity magnitude of approximately 126 m/sec. Because of this rapid mixing within the jet, the detrimental effects of the flow spoiler appear largely to reduce nozzle thrust performance, but to have little, if any, effect on the wall jet radial momentum flux distributions. In fact, this was the case, since no significant indication of a local velocity depression could be identified for any of the test conditions investigated even at the minimum radial position of R/D = 6.5.

Nozzle Spacing Effects

Azimuthal distributions of wall jet radial momentum flux were obtained for pairs of aspect ratio eight rectangular exit area nozzles for nozzle (long axis) centerline spacings of S/D = 4, 6, 8 for the case of vertical impingement at H/D = 2 and 8. Wall jet velocity profiles were surveyed at two radial positions, R/D = 14.0 and 29.0 over a range of one quarter (minimum) of the impingement region periphery, since in this case, two planes of flow symmetry exist in the ideal case. In this dual nozzle arrangement, the direction $\phi = 90°$ corresponds to a direction perpendicular to the long sides of the nozzle exits, and the direction $\phi = 0°$ corresponds to a direction coincident with the ideal stagnation line which would be formed on the ground plane by the interaction of the two nozzle flows.

Free jet surveys of the dual nozzle flows were conducted at distances downstream of the dual rectangular nozzle exits of Z/D = 2 and 8 corresponding to H/D = 2 and 8. Only in one case, for the closest nozzle spacing (S/D = 4) at an axial station corresponding to H/D = 8 did the dual jets begin to merge at the inner jet boundaries. Figures 52, 53 and 54 present the azimuthal distributions of wall jet momentum flux for the inner radial station R/D = 14.0, and figures 55, 56 and 57 present the local flow angularity at a distance of approximately 1 cm. above the ground board for the same conditions. The independent variable on figures 52, 53 and 54 is again the azimuthal angle ϕ, and the parametric variable is H/D. The momentum flux peaks at $\phi = 90°$ correspond to the basic single nozzle momentum flux characteristics presented in figures 31 and 32 for the aspect ratio eight nozzle. The second, lower peaks, at $\phi = 0°$ represent the accumulation of wall jet momentum flux in the base of the fountain formed between the two impinging jet flows. The angularity data in figures 55, 56 and 57 indicate that these flows are diverging from the direction $\phi = 0°$ near the ground plane. Figures 58, 59 and 60 present wall jet momentum flux distribution data for the outer radial station R/D = 29.0. The decay of the magnitude of the momentum flux in the fountain base

region (ϕ = 0°) is clearly indicated by these data; the consistent increase of wall jet momentum flux in the ϕ = 90° region especially for the H/D = 2.0 configuration is not well understood and needs further verification and investigation.

MODIFICATION OF GROUND FLOWFIELD PROGRAM

The azimuthal distributions of wall jet radial momentum flux presented in figures 25 through 33 for vertically impinging rectangular jets and those presented in figures 34 through 41 and 43 through 50 for oblique impingement have been curve fit for incorporation into the ground flow field computer program originally developed for axi-symmetric jets for NADC, reference 2. The method of curve fitting and the necessary functional expressions and constants are presented in the appendix. The constants presented in the appendix have been derived by imposing the requirement that the integral of the momentum flux distribution function be equal to 2π around the complete circumference of the jet impingement region. This manipulation is necessary to permit scaling of the momentum flux distribution with the total momentum flux of the individual lift jets in a multi-jet lift system. Wall jet radial momentum flux characteristics for geometry and flow conditions other than those investigated here, but within the range of those investigated, are obtained by appropriate interpolation schemes within the ground flowfield computer program.

CONCLUSIONS

The following conclusions were reached based on inspection of the experimental data obtained in the experimental test program:

1. Reynolds number effects on the impinging turbulent jet flow fields were found to be insignificant over the range from 146,000 to 275,000 based on the rectangular nozzle exit width, D,

2. The azimuthal distribution of ground wall jet radial momentum flux was found to be strongly directional for impinging rectangular jets of nozzle exit area aspect ratio four through eight at heights above ground as high as sixteen nozzle exit widths, H/D = 16,
3. The directionality of the wall jet radial momentum flux distribution is a strong function of H/D for low values of H/D typical of VTOL aircraft hovering in ground effect. The relative magnitudes of the momentum flux peaks and the average distribution level diverge as H/D decreases. Significant differences in azimuthal momentum flux distribution exist at H/D = 16 even for the lowest aspect ratio nozzle tested (L/D = 4.0),
4. Measurements of wall jet radial momentum flux representative of a fixed sector of azimuth at different radial stations indicate a significant decay of wall jet radial momentum flux between R/D = 14 and R/D = 29,
5. No significant effect on the azimuthal distribution of wall jet radial momentum flux was measured as a result of a spoiler placed in the center of the aspect ratio four nozzle exit at an impingement height above ground of H/D = 2.0 for either vertical or oblique impingement, and
6. Measurements of azimuthal distributions of wall jet momentum flux about the impingement region of pairs of aspect ratio eight rectangular jets impinging vertically on a ground plane at heights above ground of H/D = 2 and 8 indicate a significant flux of wall jet momentum along the stagnation line formed by the interaction of the two jet flows.

APPENDIX

The wall jet radial momentum flux distributions, illustrated in figures 25-41 and 43-50 for the cases of vertical impingement, oblique impingement in pitch, and oblique impingement in roll, were curve-fit in a piecewise manner as shown in figures 61-63 and then normalized for inclusion in the ground flowfield computer program. The vertical impingement distributions were fit using polynomial and trigonometric functions of azimuthal angle, ϕ, and nozzle exit aspect ratio, L/D. Similar functions of ϕ alone were determined for the oblique impingement distributions. The distributions were normalized by adjusting the coefficients in a manner such that the integral of the vertical impingement momentum flux distribution curves, over the range of $\phi = 0$ to $\phi = \pi/2$, was equal to $\pi/2$; and such that the integral of the oblique impingement momentum flux distribution curves, over the range of $\phi = 0$ to $\phi = \pi$, was equal to π.

The functional forms of the momentum flux distribution curves, as well as the corresponding normalized constants and coefficients, are shown in tables 3, 4 and 5 for the cases of vertical impingement, oblique impingement in pitch, and oblique impingement in roll, respectively.

TABLE 1
BASIC TEST PROGRAM

Free Jet Characteristics
- L/D = 4, 8
- Z/L = 0, 1/2, 1, 2, 4
- P_T/P_{amb} = 1.15

Reynolds Number Effect
- L/D = 4, 6, 8
- H/D = 8
- α_j = 90°
- P_T/P_{amb} = 1.07, 1.15, 1.28
- R/D = 14.0, 29.0
- ϕ = 0°, 90°

Vertical Impingement
- L/D = 4, 6, 8
- H/D = 2, 8, 16
- α_j = 90°
- P_T/P_{amb} = 1.15
- R/D = 14.0, 29.0
- ϕ = 0°, 15°, 30°, 45°, 60°, 75°, 90°

Oblique Impingement
- L/D = 4, 6, 8
- H/D = 2, 4, 8
- α_j = 75°, 60°
- θ_j = 75°, 60°
- P_T/P_{amb} = 1.15
- R/D = 21.5
- ϕ = 0°, 15°, 30°, 45°, 60°, 75°, 90°, 105°, 120°, 135°, 150°, 165°, 180°

(H/D = 2 condition not tested for all combinations of L/D and impingement angle)

Exit Velocity Profile Effect
- L/D = 4
- H/D = 2
- α_j = 90°, 75°, 60°
- θ_j = 75°, 60°
- P_T/P_{amb} = 1.15
- R/D = 6.5, 14.0
- ϕ = 10 angles in vicinity of P_T depression

Nozzle Spacing Effect (Two Nozzles)
- L/D = 8
- H/D = 2, 8
- α_j = 90° (both jets)
- P_T/P_{amb} = 1.15
- R/D = 14.0, 29.0
- ϕ = 0°, 15°, 30°, 45°, 60°, 75°, 90°
- S/D = 4, 6, 8

TABLE 2
FLOWFIELD SURVEYS

	Surveys
1. Free Jet Characteristics	51
2. Reynolds Number Effect	47
3. Vertical Impingement	126
4. Oblique Impingement	436
5. Exit Velocity Profile Effect	153
6. Nozzle Spacing Effect	115
Total	928

GP78-0700-1

(See Figure 60)

- $F\,(1) = f_o + C_1\,\phi + C_2\,\phi^2 + C_3\,\phi^3$ $\qquad (0 \leq \phi < \phi_2)$
- $F\,(2) = f_2 + (C_4 + C_5\,L/D)\,\sin 6\,(\phi - \phi_2)$ $\qquad (\phi_2 \leq \phi \leq \frac{\pi}{2})$
- $f = F\,(1)\,;\,F\,(2)$
- $\int_0^{\pi/2} f\,d\phi = \frac{\pi}{2}$

L/D	H/D	ϕ_2	f_o	f_2	C_1	C_2	C_3	C_4	C_5
4	2	5π/12	0.310	1.920	1.113	−3.977	3.107	1.177	0.310
6	2	5π/12	0.291	1.803	1.044	−3.733	2.917	1.105	0.291
8	2	5π/12	0.274	1.697	0.983	−3.515	2.746	1.040	0.274
4	8	5π/12	0.325	2.065	0.927	−2.340	2.022	−1.376	0.459
6	8	5π/12	0.296	1.881	0.844	−2.132	1.842	−1.254	0.418
8	8	5π/12	0.272	1.728	0.776	−1.958	1.692	−1.152	0.384
4	16	π/3	0.563	1.310	−0.219	1.279	−0.370	−0.218	0.109
6	16	π/3	0.551	1.282	−0.215	1.251	−0.362	−0.214	0.107
8	16	π/3	0.539	1.253	−0.210	1.223	−0.354	−0.209	0.104

GP78-0770-71

TABLE 3
NORMALIZED WALL JET MOMENTUM FLUX DISTRIBUTION COEFFICIENTS
Vertical Impingement

TABLE 4
NORMALIZED WALL JET MOMENTUM FLUX DISTRIBUTION COEFFICIENTS
Oblique Impingement - Pitch

(See Figure 61)

- $F\,(1) = f_o + C_1\,\phi + C_2\,\phi^2 + C_3\,\phi^3$ $\qquad (0 \leq \phi < \phi_1)$
- $F\,(2) = f_1 + (f_2 - f_1)\sin 6\,(\phi - \phi_1)$ $\qquad (\phi_1 \leq \phi < \phi_3)$
- $F\,(3) = C_4 + C_5\,\phi + C_6\,\phi^2$ $\qquad (\phi_3 \leq \phi < \phi_4)$
- $F\,(4) = f_4$ $\qquad (\phi_4 \leq \phi \leq \pi)$
- $f = F\,(1)\,;F\,(2)\,;F\,(3)\,;F\,(4)$
- $\int_0^{\pi} f\,d\phi = \pi$

L/D	H/D	α	ϕ_1	ϕ_3	ϕ_4	f_o	f_1	f_2	f_4	C_1	C_2	C_3	C_4	C_5	C_6
4	2	75	$\pi/3$	$\pi/2$	$2\pi/3$	0.508	1.726	4.872	0.102	1.422	−5.183	4.714	26.085	−24.812	5.923
6	2	↓	↓	↓	↓	0.406	1.651	5.613	0.064	1.657	−6.439	5.721	26.225	−25.103	6.022
4	4	↓	↓	↓	↓	0.579	1.930	3.860	0.097	2.150	−5.984	4.930	23.642	−21.563	4.928
6	4	↓	↓	↓	↓	0.335	1.860	4.811	0.062	2.333	−6.717	5.615	24.812	−22.995	5.337
8	4	↓	↓	↓	$2\pi/3$	0.298	1.573	5.610	0.043	2.451	−7.131	5.685	21.666	−20.194	4.712
4	8	↓	↓	↓	$3\pi/4$	0.733	1.980	2.713	0.099	0.801	−1.986	2.253	12.870	−9.958	1.926
6	8	↓	↓	↓	↓	0.585	2.080	3.380	0.065	1.221	−3.438	3.472	19.565	−16.842	3.635
8	8	75	$\pi/3$	$\pi/2$	$3\pi/4$	0.499	1.939	4.051	0.048	1.045	−2.346	2.541	19.286	−16.800	3.659
4	2	60	$\pi/4$	$5\pi/12$	$7\pi/12$	0.990	1.980	3.960	0.099	0.126	−1.445	3.678	22.275	−24.013	6.500
4	4	↓	↓	↓	↓	1.089	1.980	3.465	0.099	0.567	−1.445	2.759	18.810	−19.476	5.056
6	4	↓	↓	↓	↓	0.769	1.984	4.439	0.062	0.126	−1.628	4.377	20.894	−22.143	5.880
8	4	↓	↓	↓	$7\pi/12$	0.757	1.958	4.717	0.045	0.969	−4.545	6.696	24.030	−26.296	7.207
4	8	↓	↓	↓	$2\pi/3$	1.316	1.974	2.632	0.094	−0.347	4.115	−3.318	15.134	−14.841	3.657
6	8	↓	↓	↓	↓	1.170	2.145	2.925	0.065	0.248	1.897	1.3E-5	16.445	−16.097	3.952
8	8	60	$\pi/4$	$5\pi/12$	$2\pi/3$	1.067	1.959	3.250	0.049	0.136	1.132	0.180	13.551	−12.869	3.066

GP78-0770-72

TABLE 5
NORMALIZED WALL JET MOMENTUM FLUX DISTRIBUTION COEFFICIENTS
Oblique Impingement - Roll

(See Figure 62)

- $F\,(1) = f_1 + (f_o - f_1)\cos 6\phi$ $\quad (0 \leq \phi < \pi/12)$
- $F\,(2) = C_o + C_1\,\phi + C_2\,\phi^2 + C_3\,\phi^3$ $\quad (\pi/12 \leq \phi < \pi/3)$
- $F\,(3) = C_4 + C_5\,\phi$ $\quad (\pi/3 \leq \phi < 3\pi/4)$
- $F\,(4) = C_6 + C_7\,\phi + C_8\,\phi^2$ $\quad (3\pi/4 \leq \phi < 11\pi/12)$
- $F\,(5) = f_4 + (f_5 - f_4)\sin 6\,(\phi - 11/12\,\pi)$ $\quad (11/12\,\pi \leq \phi \leq \pi)$
- $f = F\,(1)\,; F\,(2)\,; F\,(3)\,; F\,(4)\,; F\,(5)$
- $\int_0^{\pi} f\,d\phi = \pi$

L/D	H/D	θ	f_o	f_1	f_4	f_5	C_o	C_1	C_2	C_3	C_4	C_5	C_6	C_7	C_8
4	2	75	6.426	2.268	1.418	3.119	6.048	−20.093	24.128	−9.655	0.605	−0.217	31.562	−26.349	5.515
6	2	↓	7.728	1.978	1.265	4.186	5.624	−19.357	23.154	−9.186	0.288	−0.088	32.889	−27.168	5.621
4	4	↓	5.790	2.444	1.260	2.726	5.132	−13.117	11.795	−3.492	0.380	−0.058	18.010	−15.295	3.292
6	4	↓	6.845	2.223	1.170	3.428	5.405	−16.446	18.180	−6.846	0.351	−0.089	22.147	−18.591	3.926
8	4	↓	7.659	2.575	0.888	4.085	8.066	−29.523	36.547	−14.846	0.219	−0.040	19.040	−15.786	3.293
4	8	↓	4.019	2.652	1.224	1.734	4.794	−10.325	8.929	−2.842	0.755	−0.234	−4.386	1.948	1.42E-5
6	8	↓	4.712	2.402	1.254	2.204	4.171	−8.176	5.778	−1.349	0.502	−0.101	8.223	−7.689	1.830
8	8	75	5.961	2.093	1.019	3.385	4.004	−9.078	7.302	−1.944	0.288	−0.014	8.526	−7.577	1.726
4	2	60	8.366	2.314	0.712	1.958	6.052	−20.170	25.321	−10.747	0.570	−0.204	19.312	−15.807	3.246
4	4	↓	8.335	2.778	0.567	1.739	6.823	−21.032	23.715	−9.129	0.488	−0.159	14.912	−12.128	2.482
6	4	↓	8.803	2.596	0.519	2.667	6.643	−21.131	24.103	−9.316	0.399	−0.144	16.095	−13.093	2.668
8	4	↓	9.165	2.605	0.374	3.760	8.096	−29.520	36.531	−14.852	0.306	−0.113	11.271	−9.191	1.878
4	8	↓	4.693	2.888	0.570	0.798	4.598	−7.523	3.881	−0.353	0.768	−0.189	5.795	−4.608	0.970
6	8	↓	5.888	3.034	0.640	1.152	5.747	−13.144	11.579	−3.686	0.653	−0.196	7.680	−6.478	1.401
8	8	60	7.397	2.898	0.598	1.408	5.373	−11.462	8.121	−1.709	0.438	−0.120	6.366	−5.482	1.208

GP78-0770-70

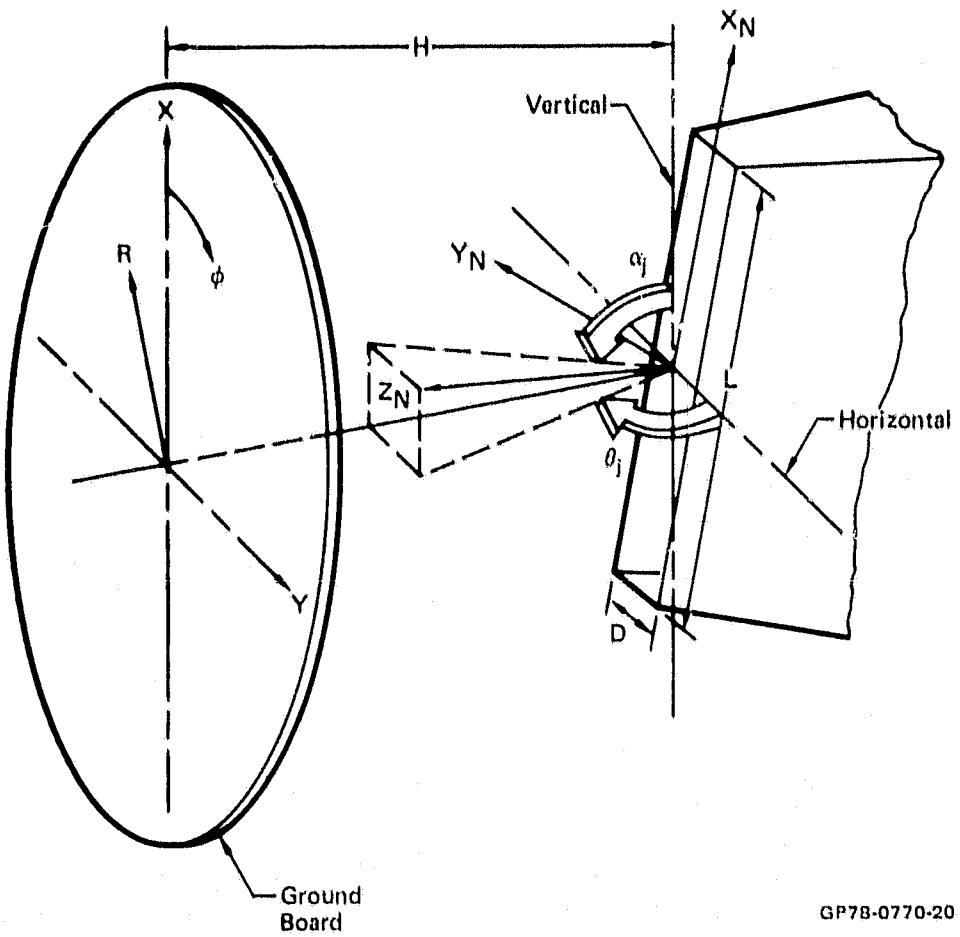

FIGURE 1
TEST NOMENCLATURE

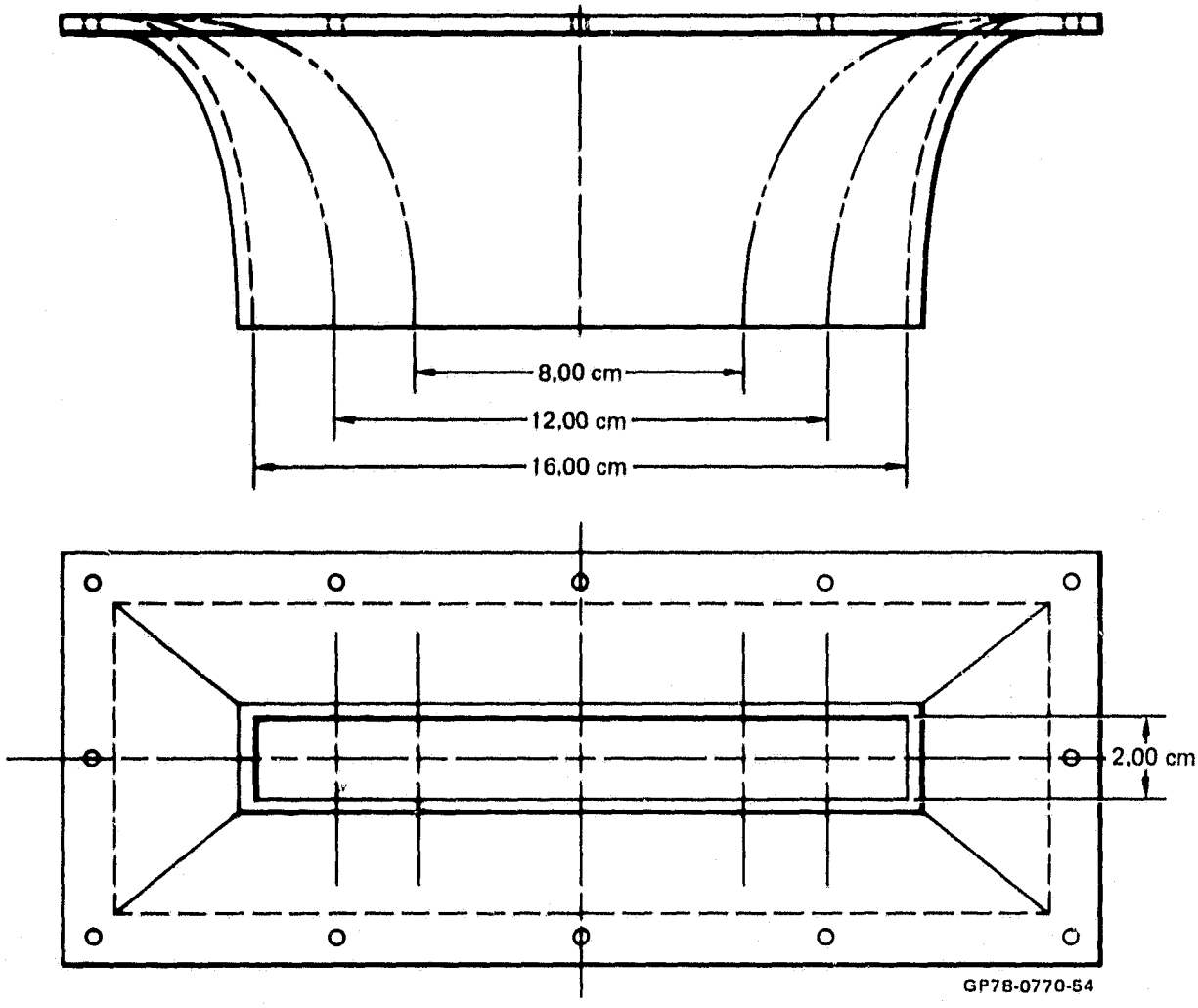

FIGURE 2
SINGLE NOZZLE CONFIGURATIONS

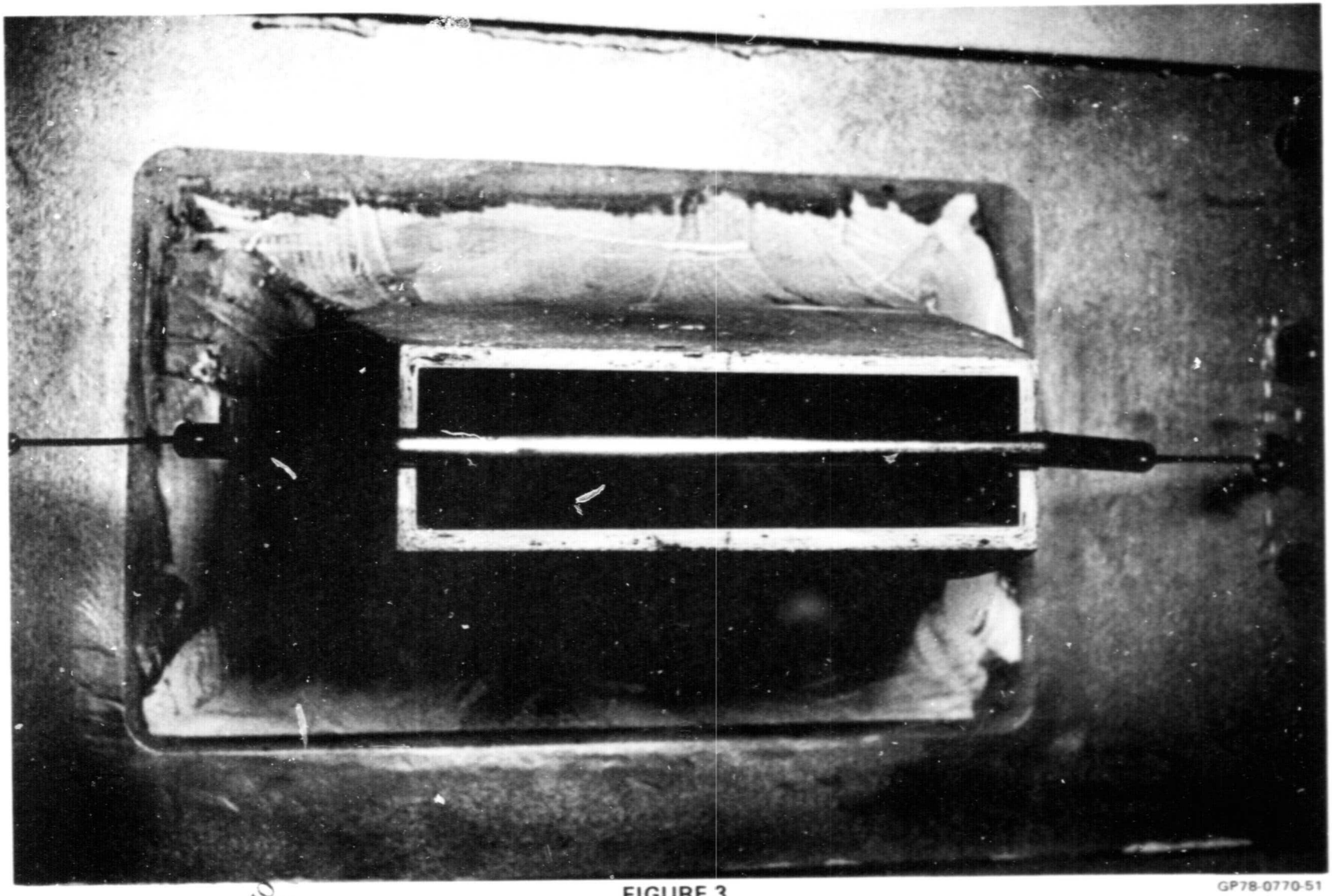

GP78-0770-51

FIGURE 3
ASPECT RATIO FOUR RECTANGULAR EXIT CONVERGING NOZZLE
With Flow Spoiler

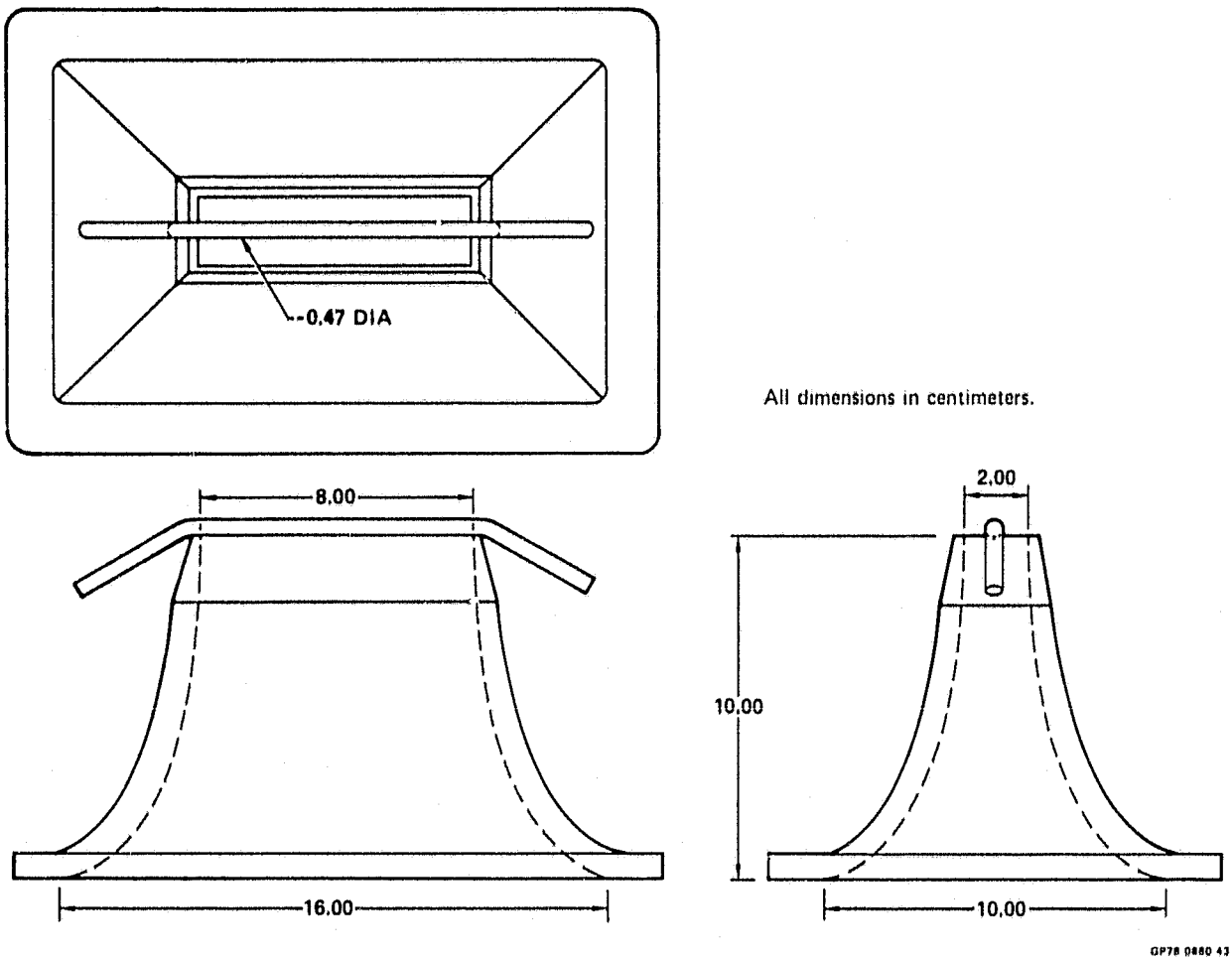

FIGURE 4
FLOW SPOILER INSTALLATION

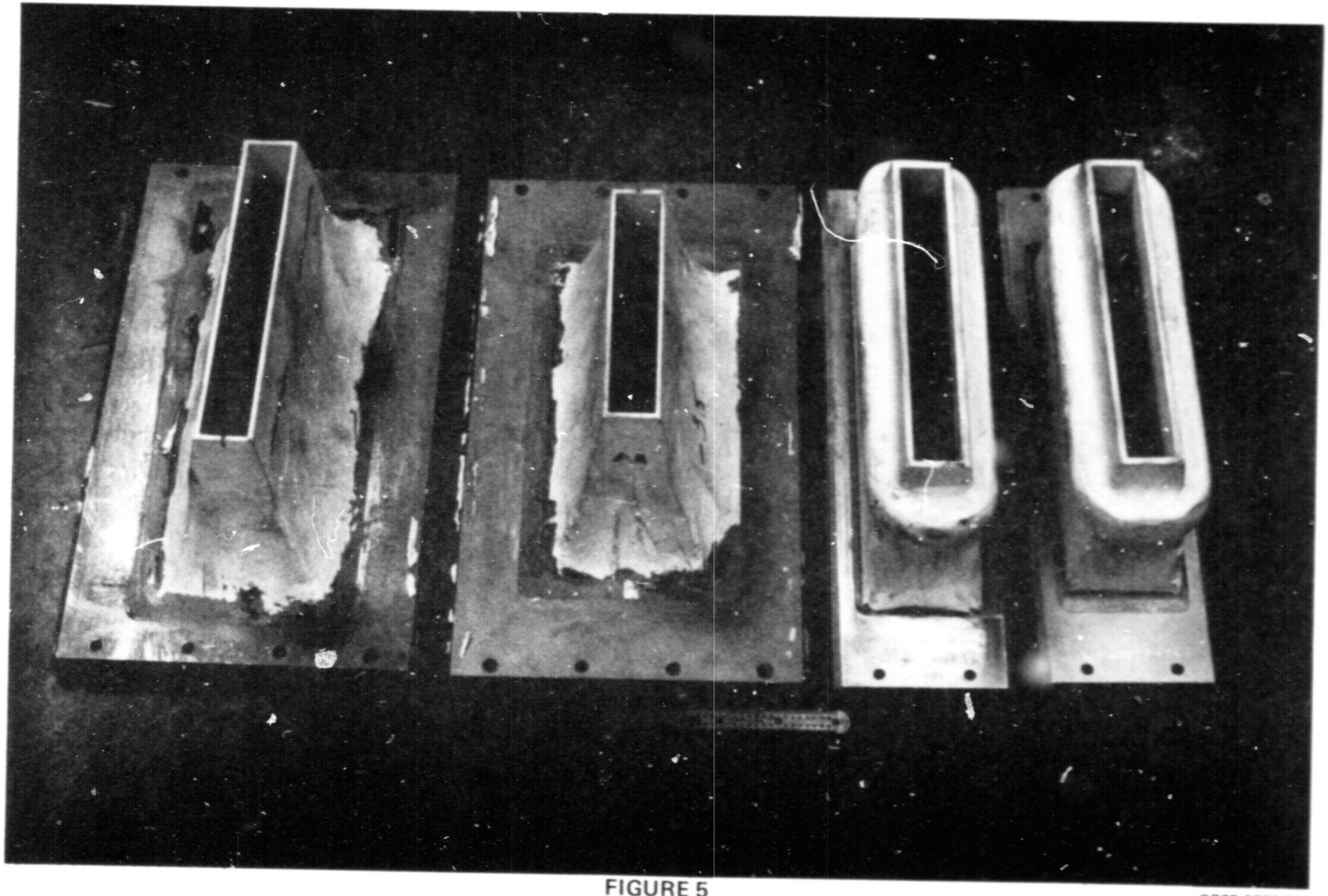

FIGURE 5
ASPECT RATIO SIX AND EIGHT RECTANGULAR EXIT CONVERGING NOZZLES

GP78-0770-50

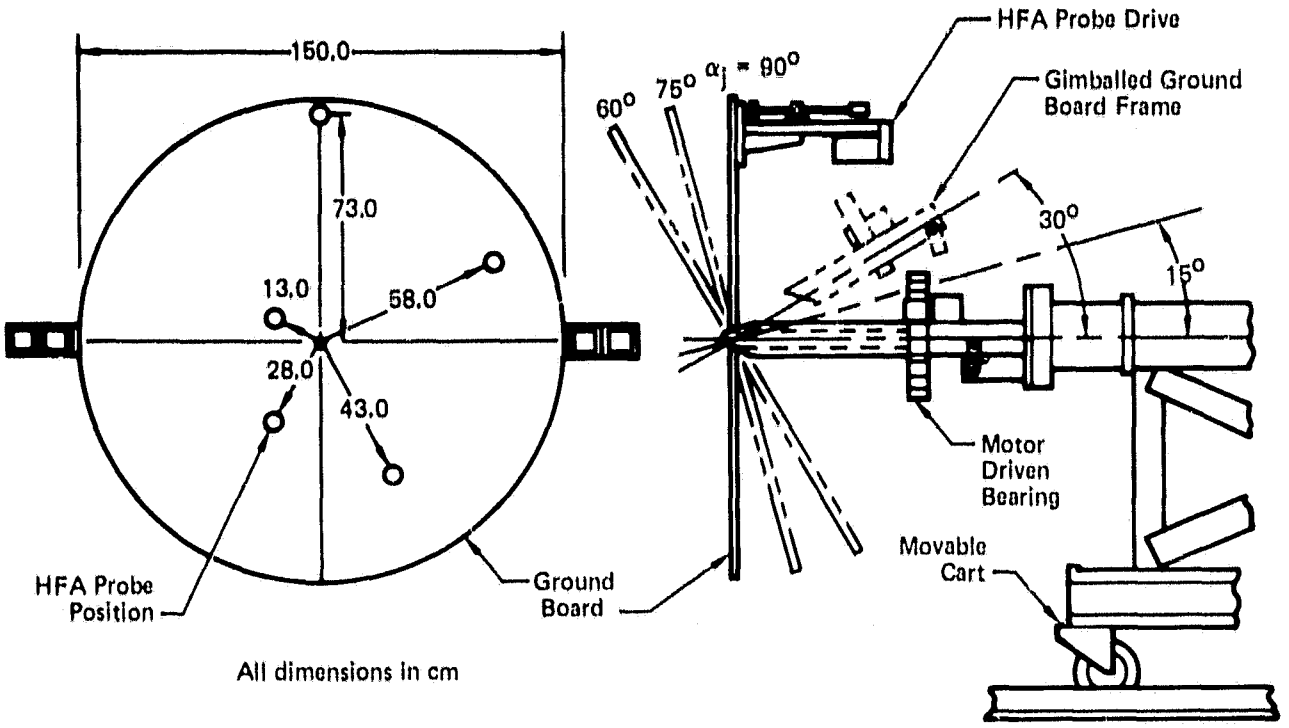

FIGURE 6
GROUND BOARD AND SUPPORT HARDWARE
Pitch Configuration

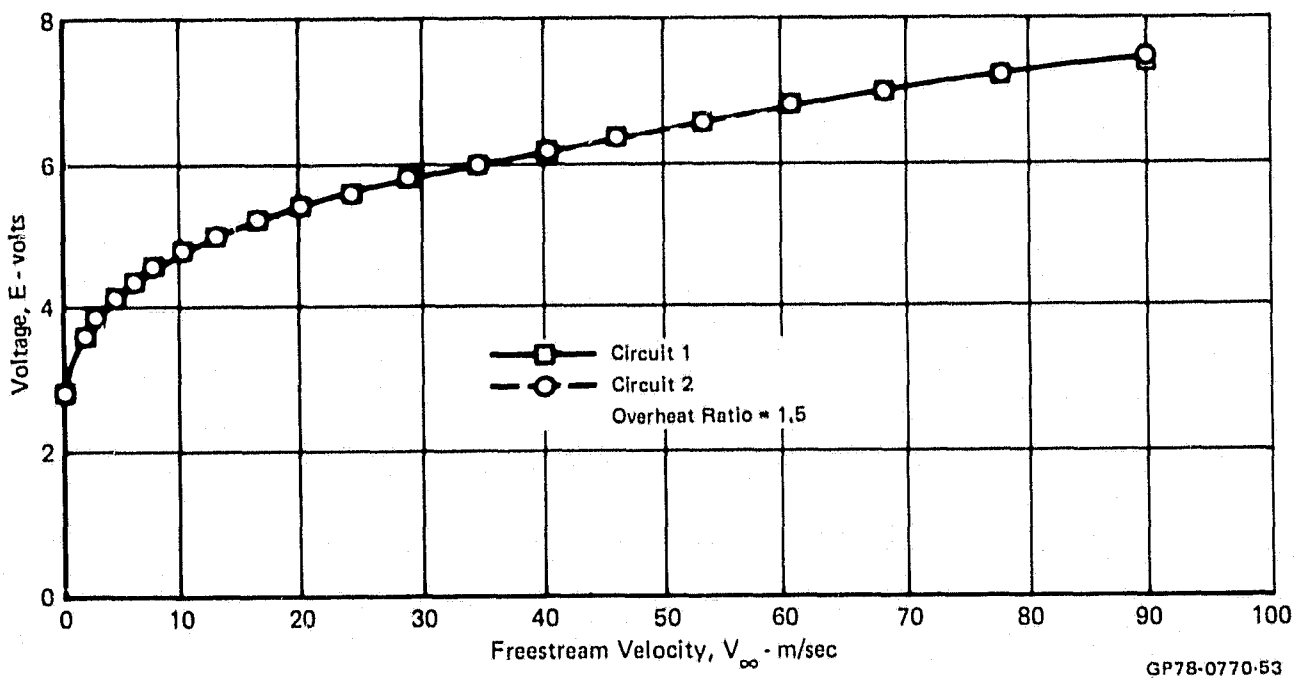

FIGURE 7
HOT FILM ANEMOMETER MEAN FLOW CALIBRATION
Voltage vs Freestream Velocity Probe No. B576

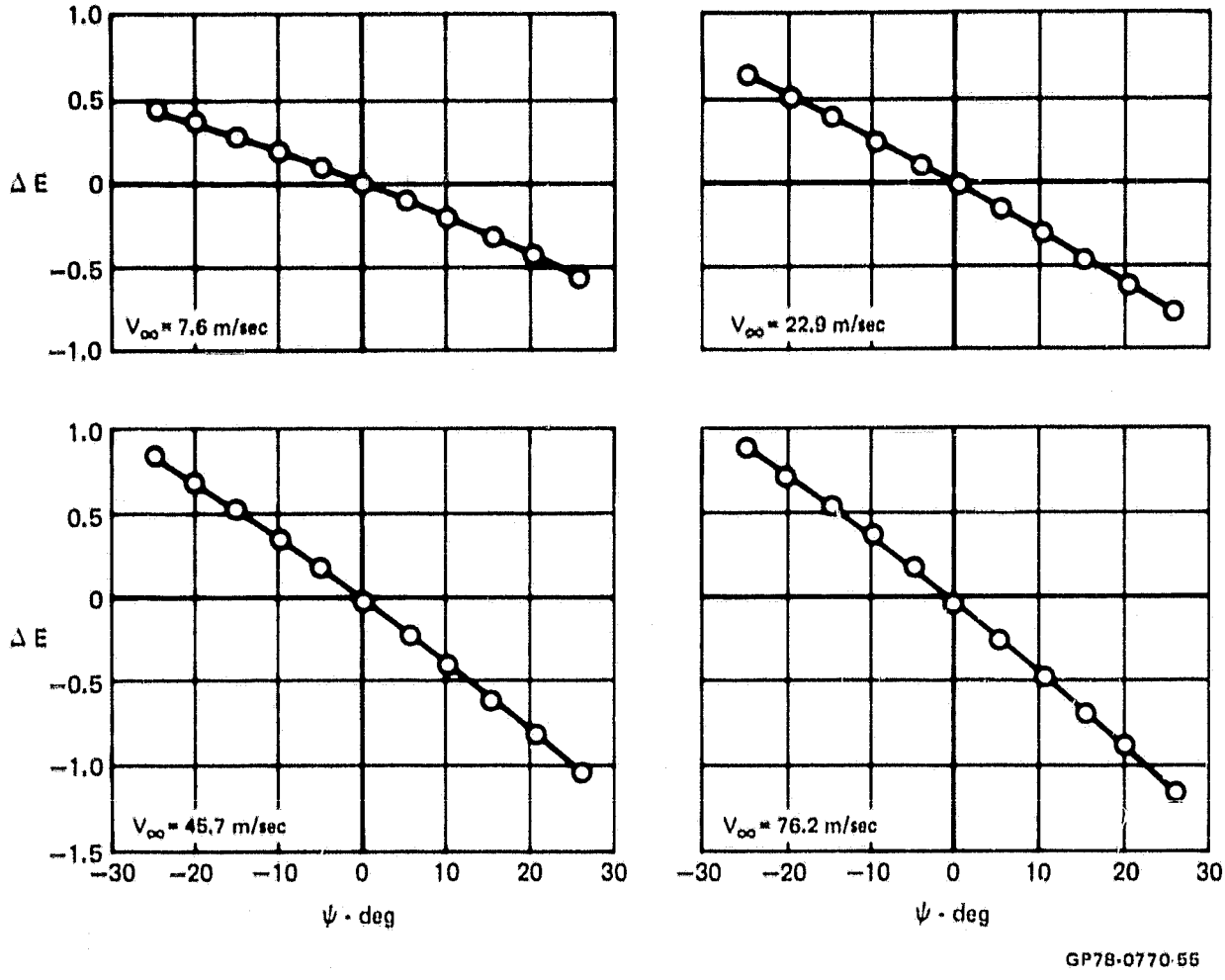

FIGURE 8
HOT FILM ANEMOMETER YAW CALIBRATION
Voltage Difference vs Probe Yaw Angle
Probe No. B576
$\Delta E = E_2 - E_1$

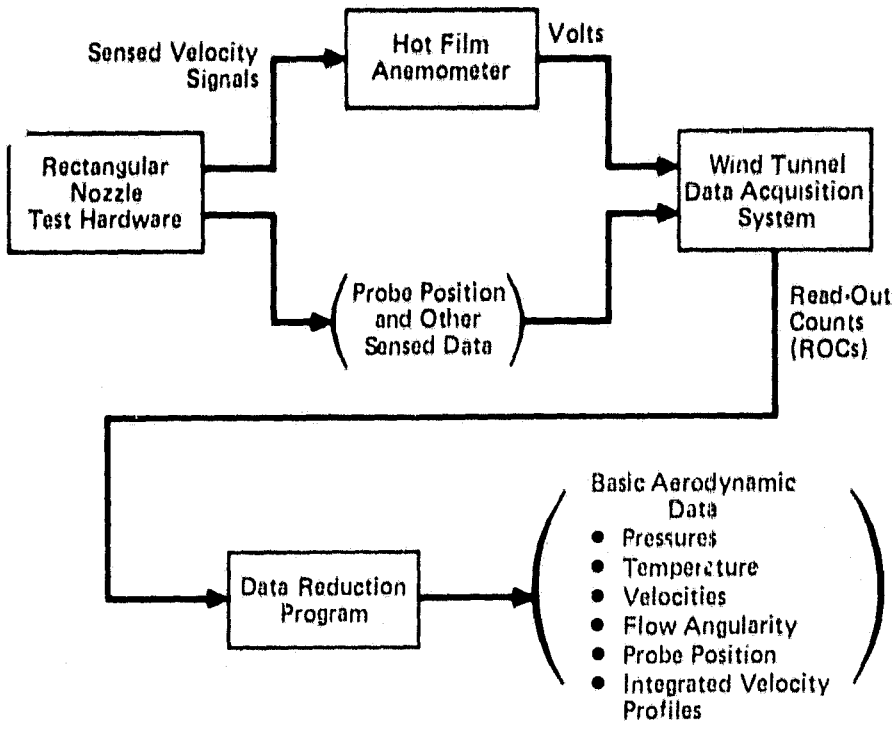

FIGURE 9
WIND TUNNEL TEST
Data Acquisition Elements

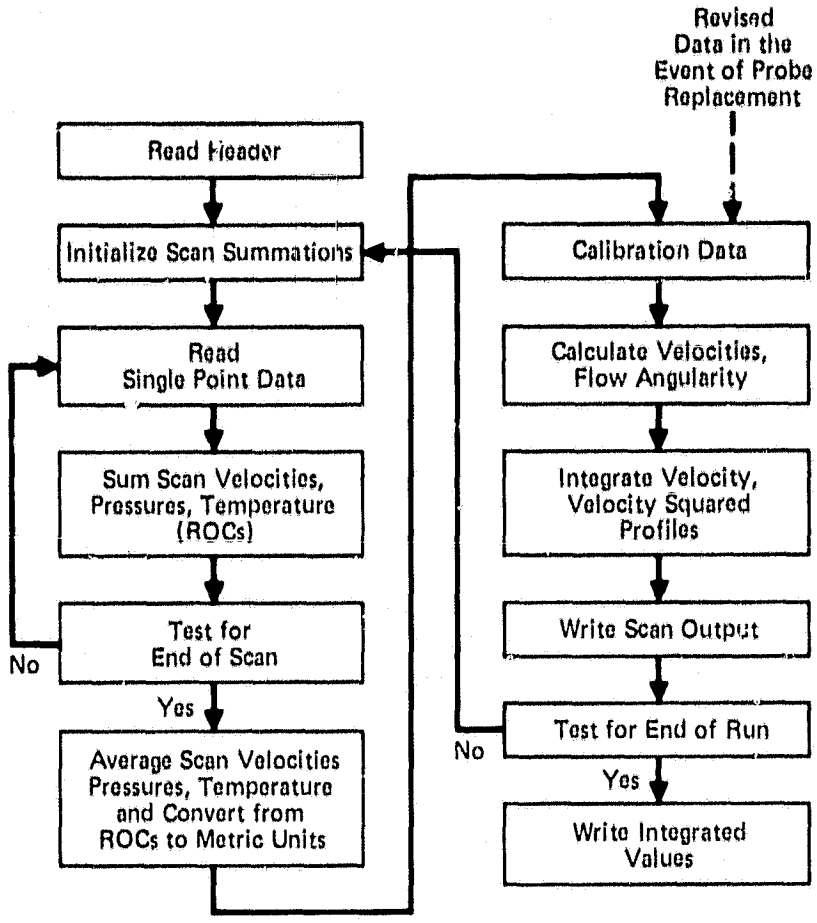

GP78-0770-52

FIGURE 10
WIND TUNNEL TEST
Data Reduction Program

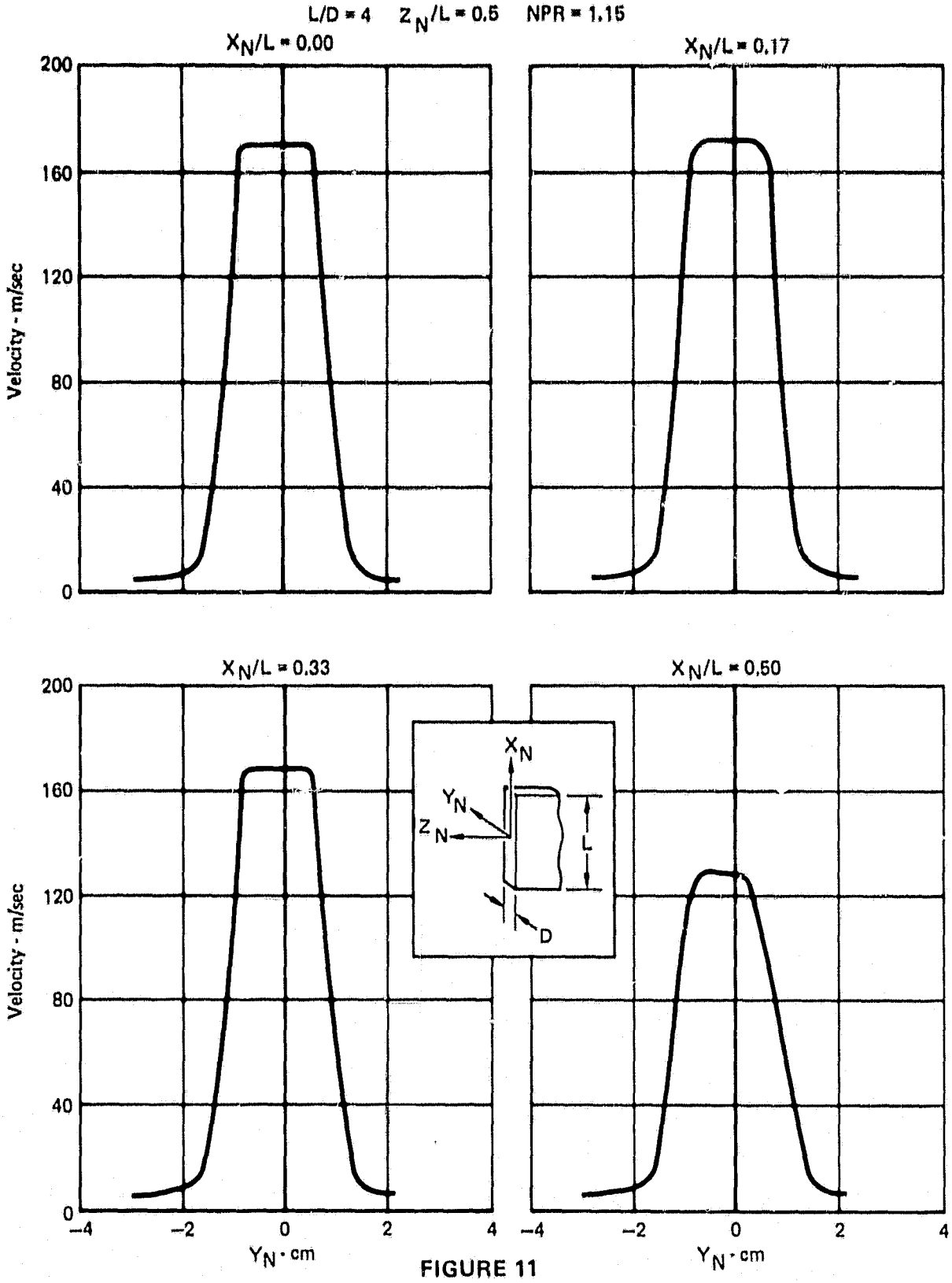

FIGURE 11
FREE-JET VELOCITY PROFILE

GP78-0770-22

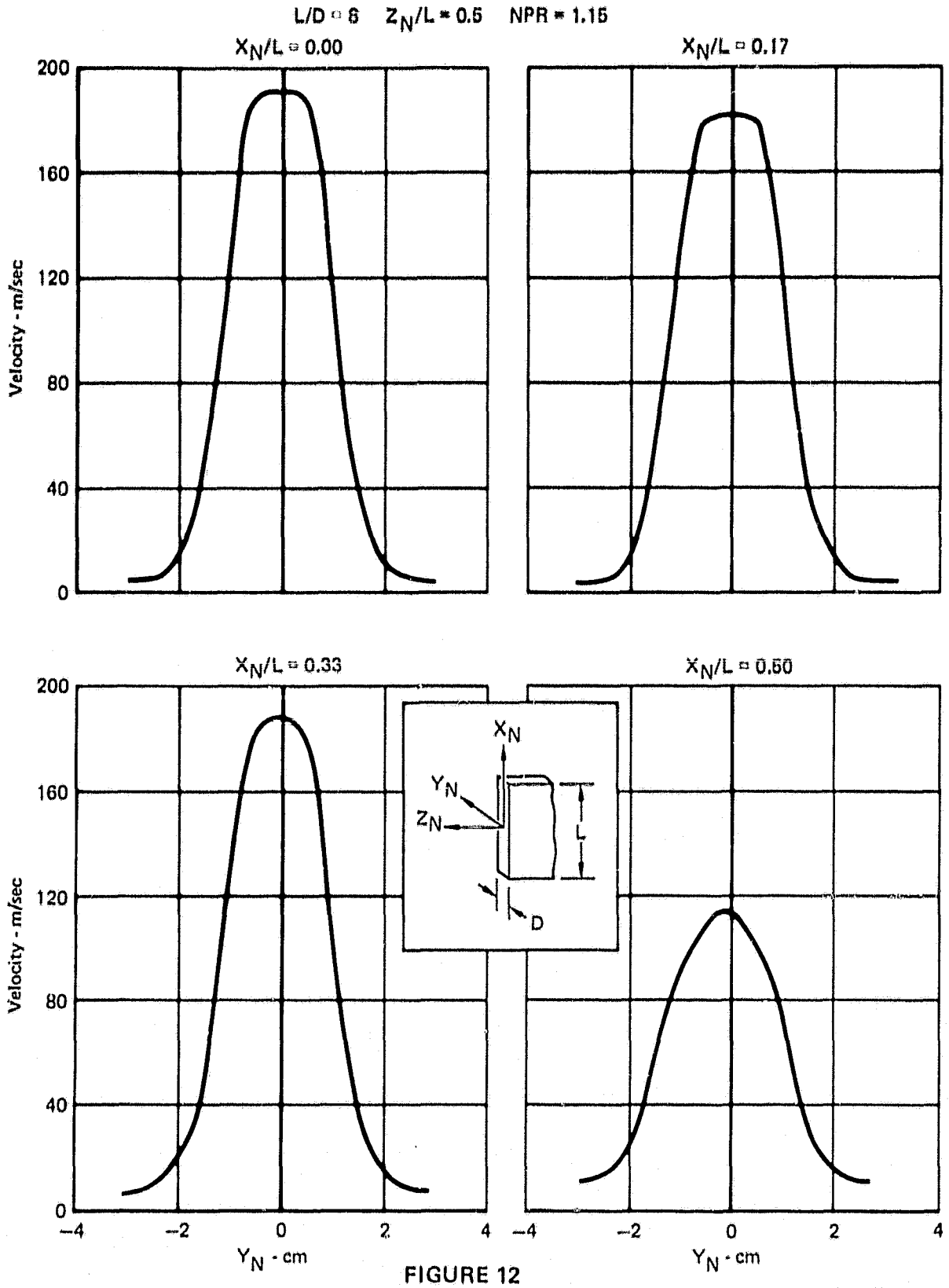

FIGURE 12
FREE-JET VELOCITY PROFILE

GP78-0770-21

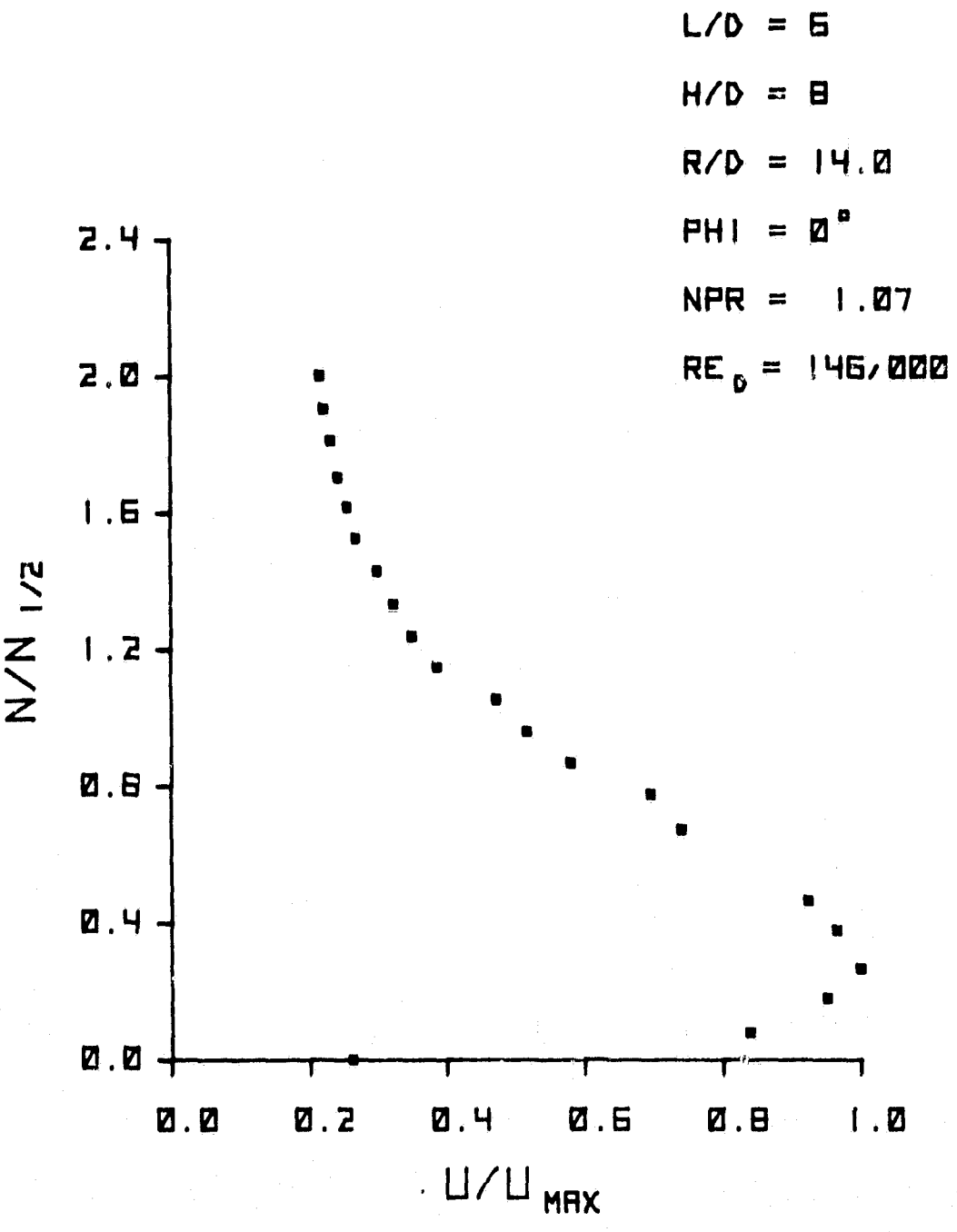

FIGURE 13
WALL JET VELOCITY PROFILE

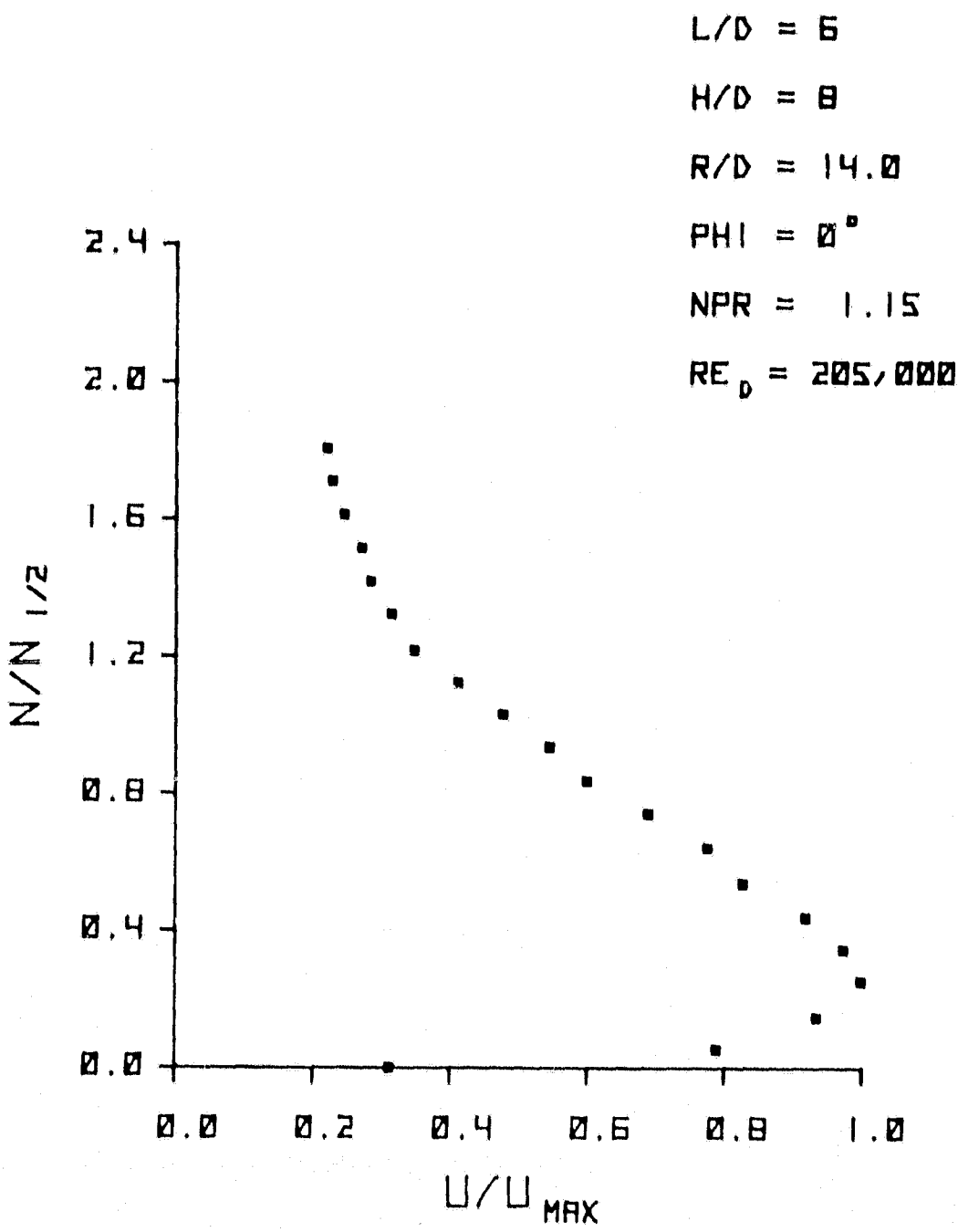

GP78 0770-67

FIGURE 14
WALL JET VELOCITY PROFILE

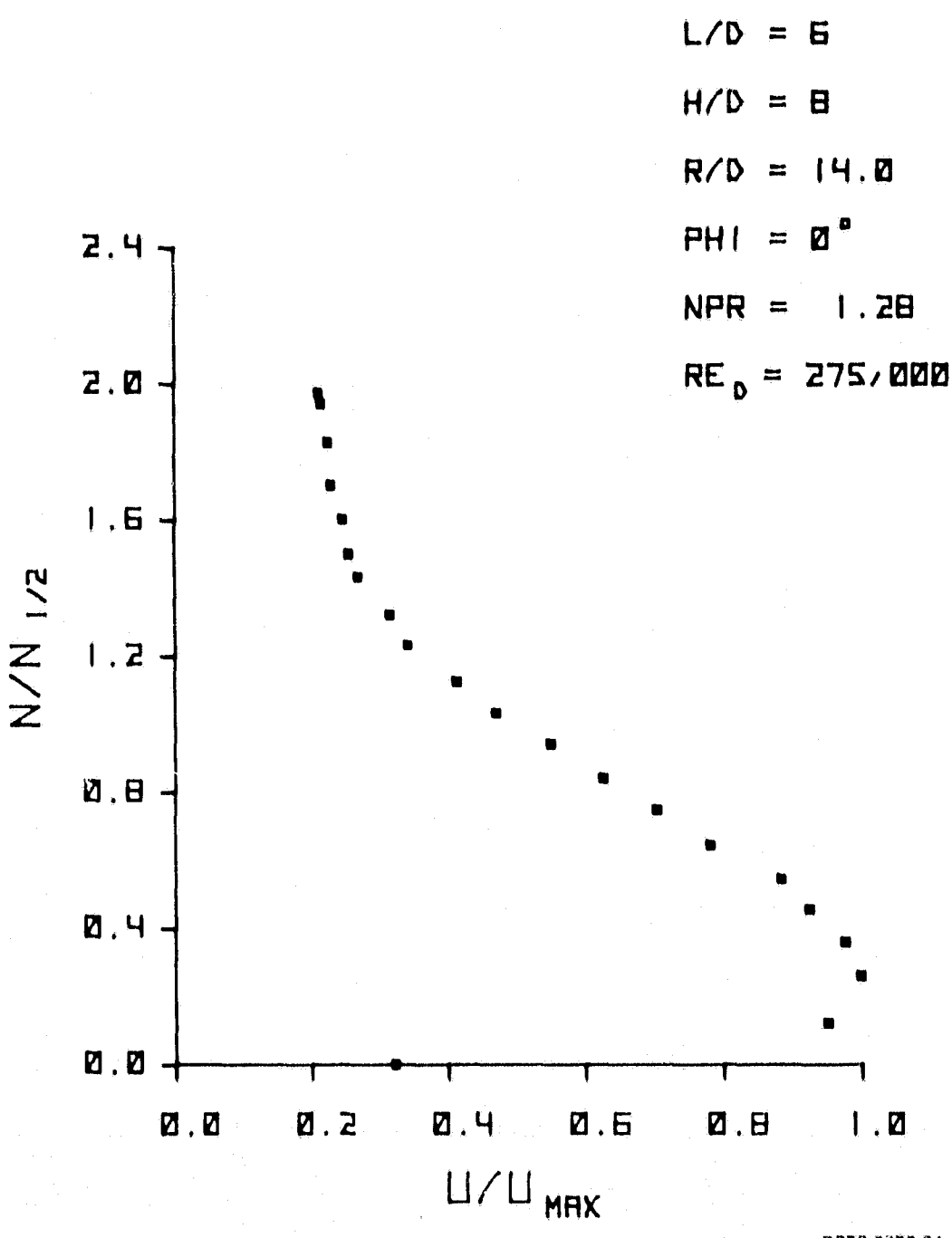

GP78-0770-64

FIGURE 15
WALL JET VELOCITY PROFILE

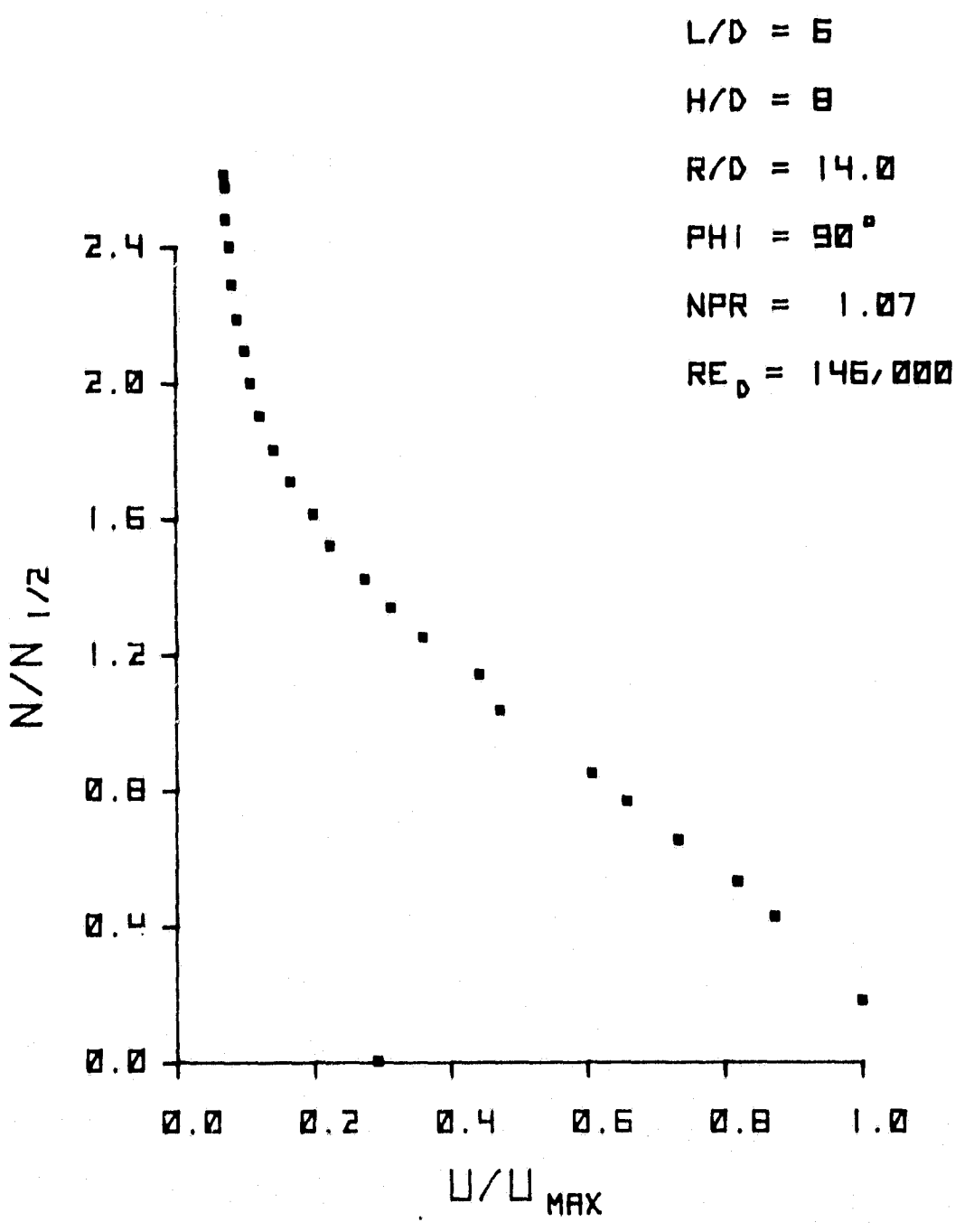

GP78-0770-69

FIGURE 16
WALL JET VELOCITY PROFILE

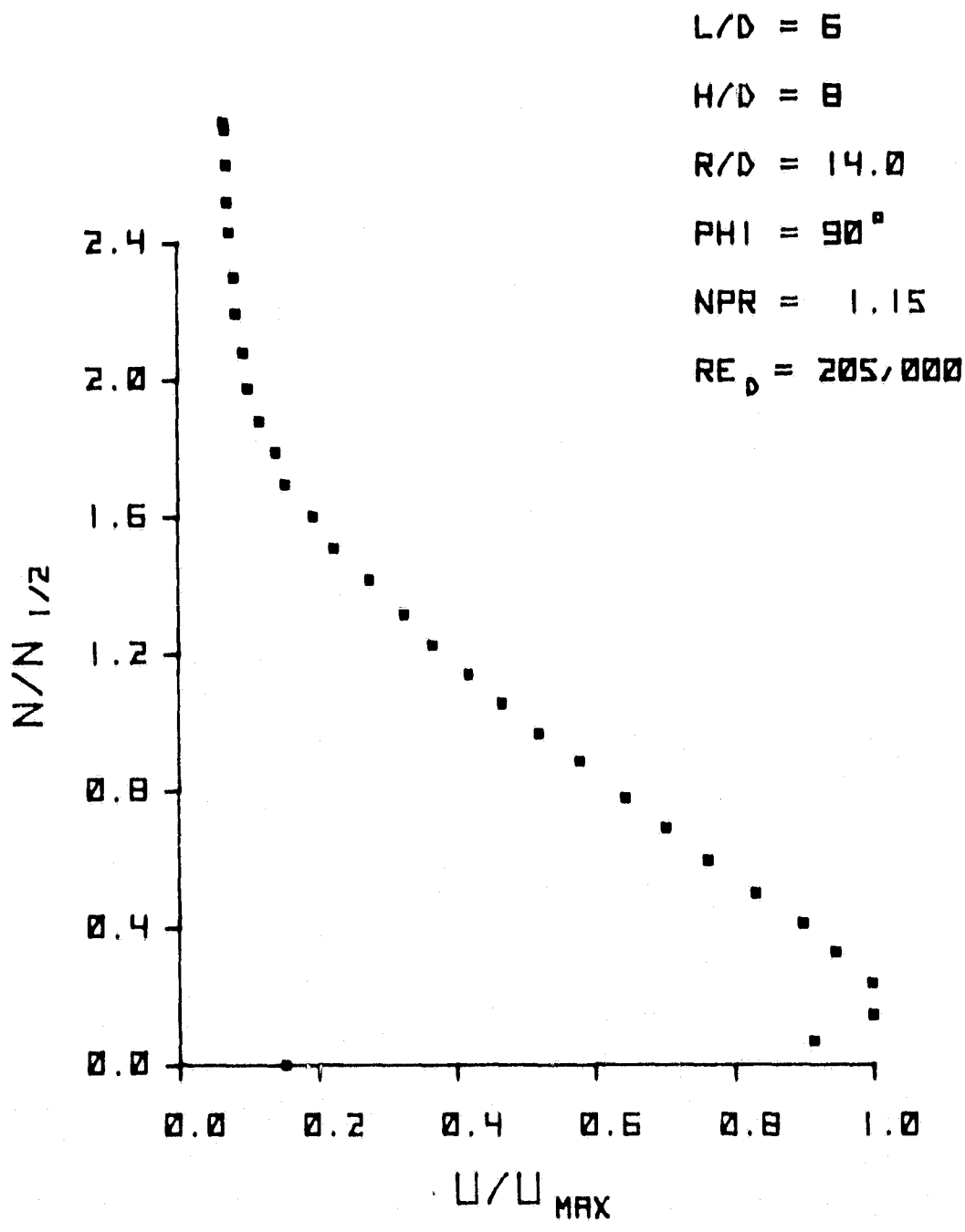

GP78-0770-68

FIGURE 17
WALL JET VELOCITY PROFILE

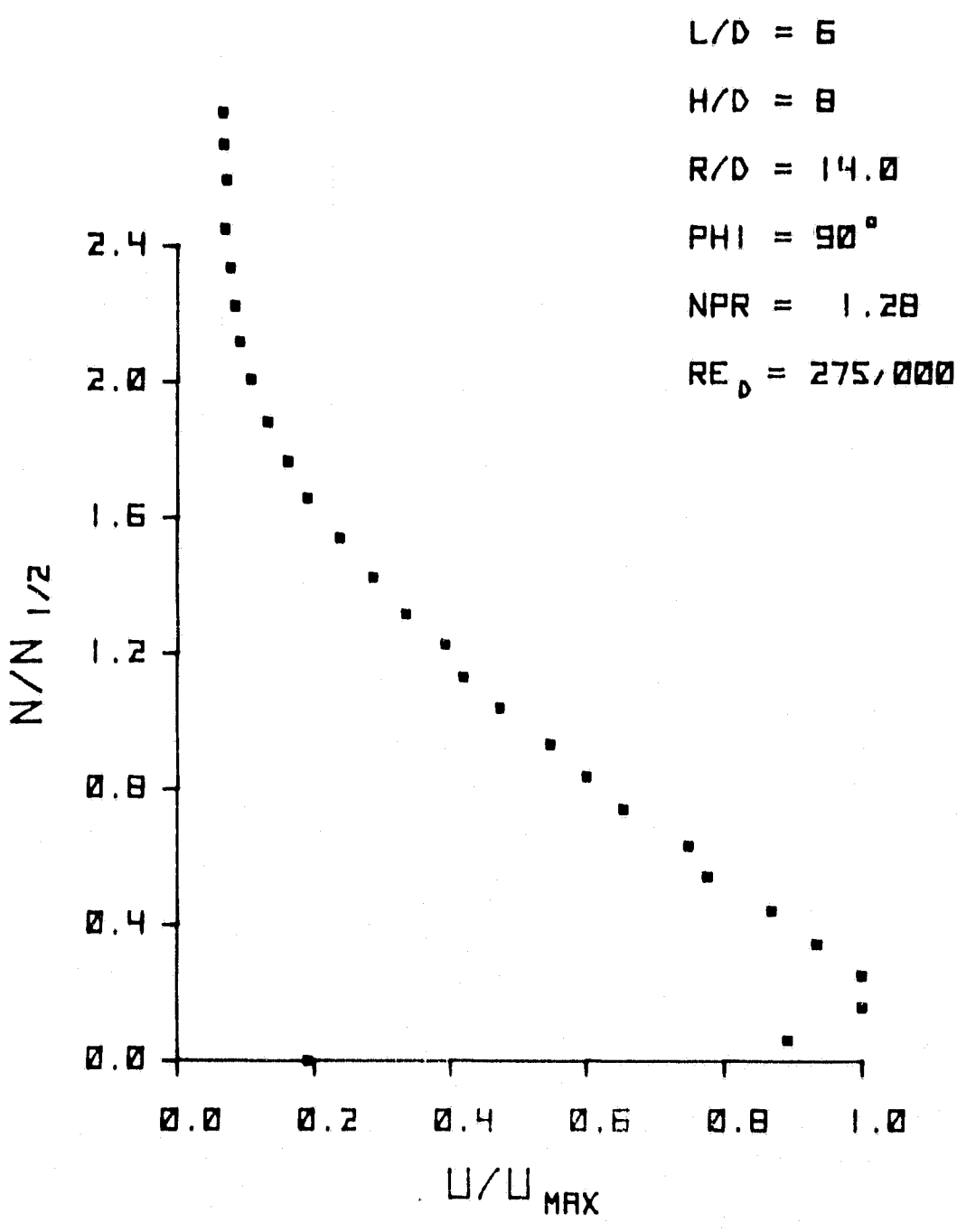

GP78-0770-63

FIGURE 18
WALL JET VELOCITY PROFILE

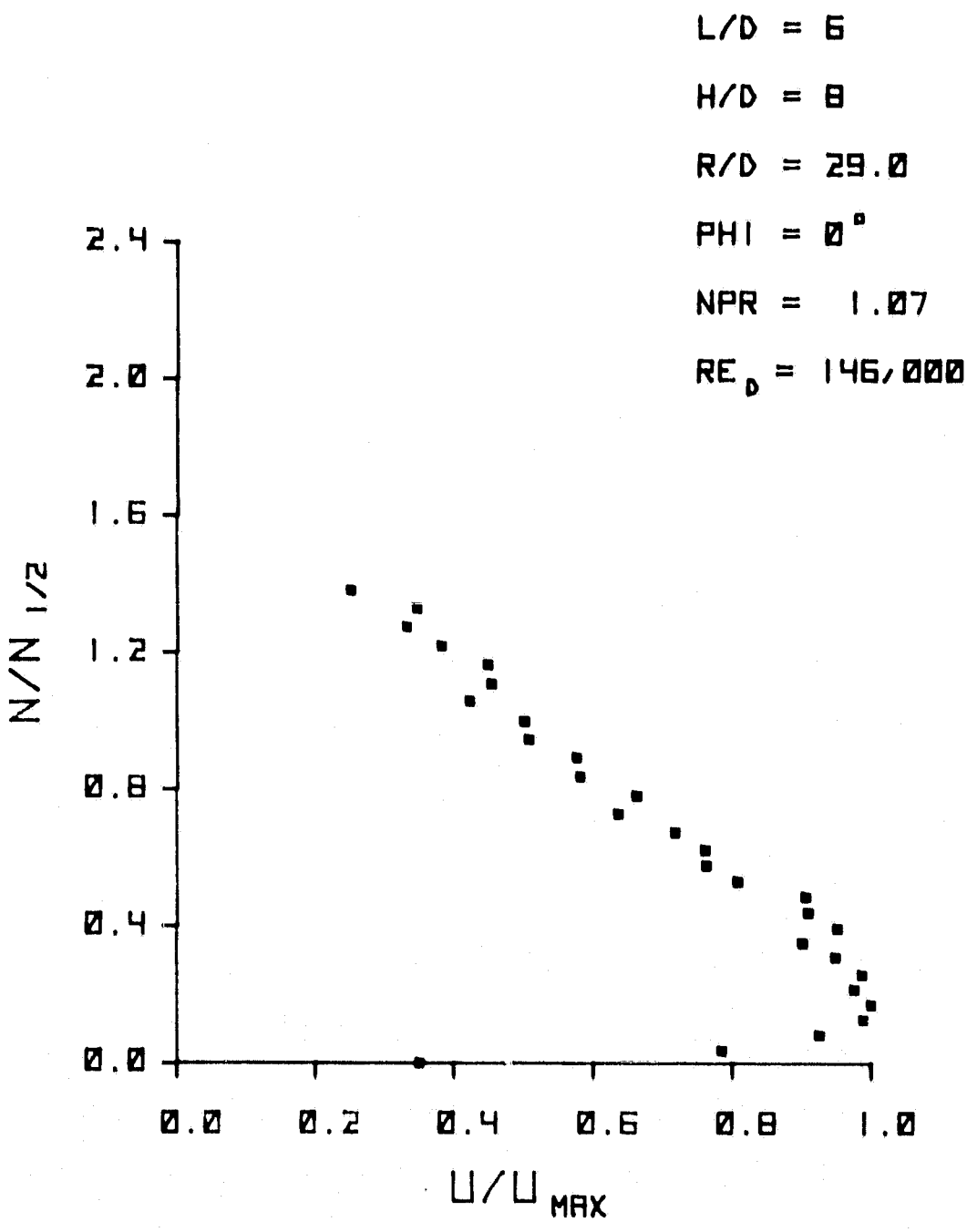

GP78-0770-65

FIGURE 19
WALL JET VELOCITY PROFILE

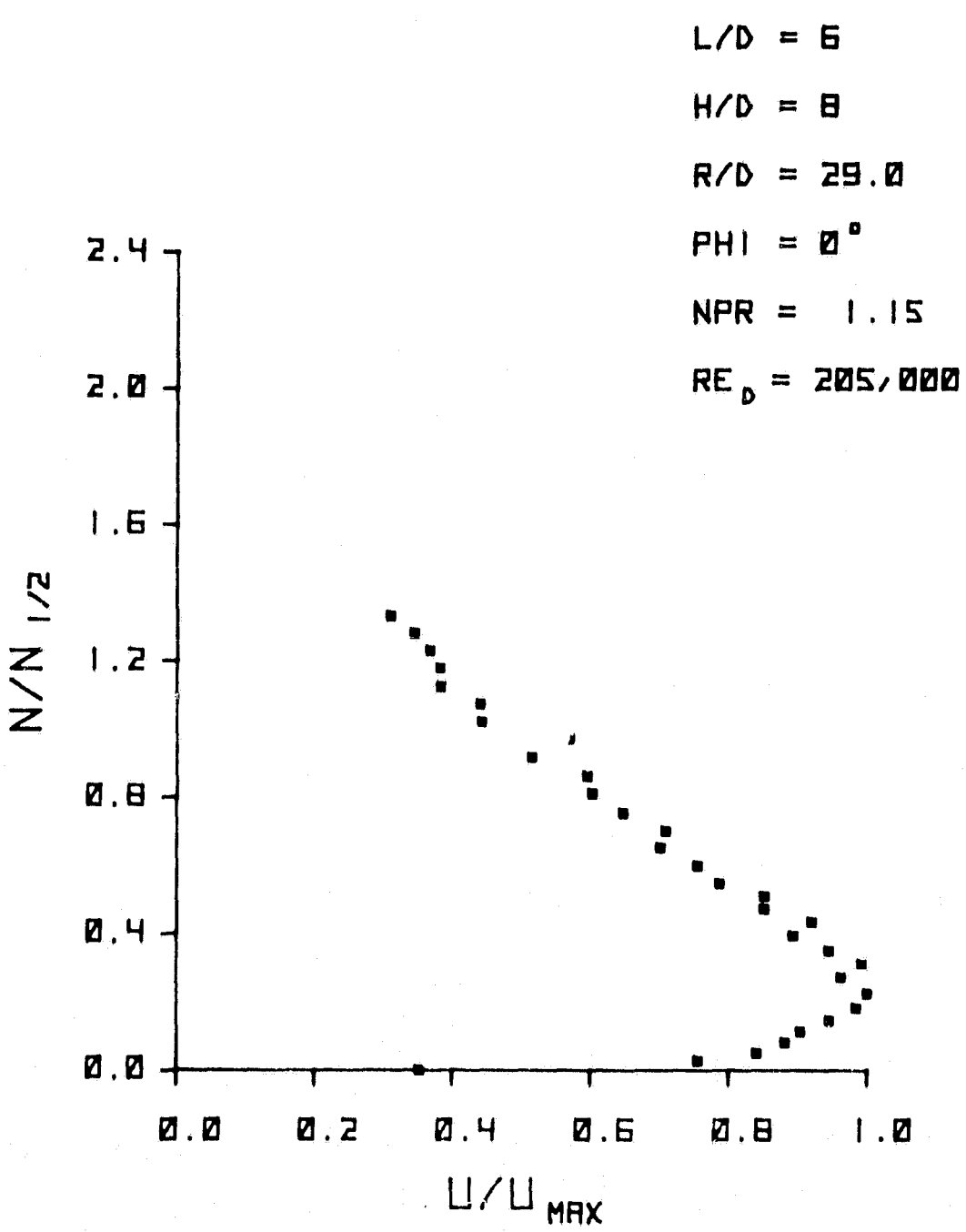

GP78-0770-61

FIGURE 20
WALL JET VELOCITY PROFILE

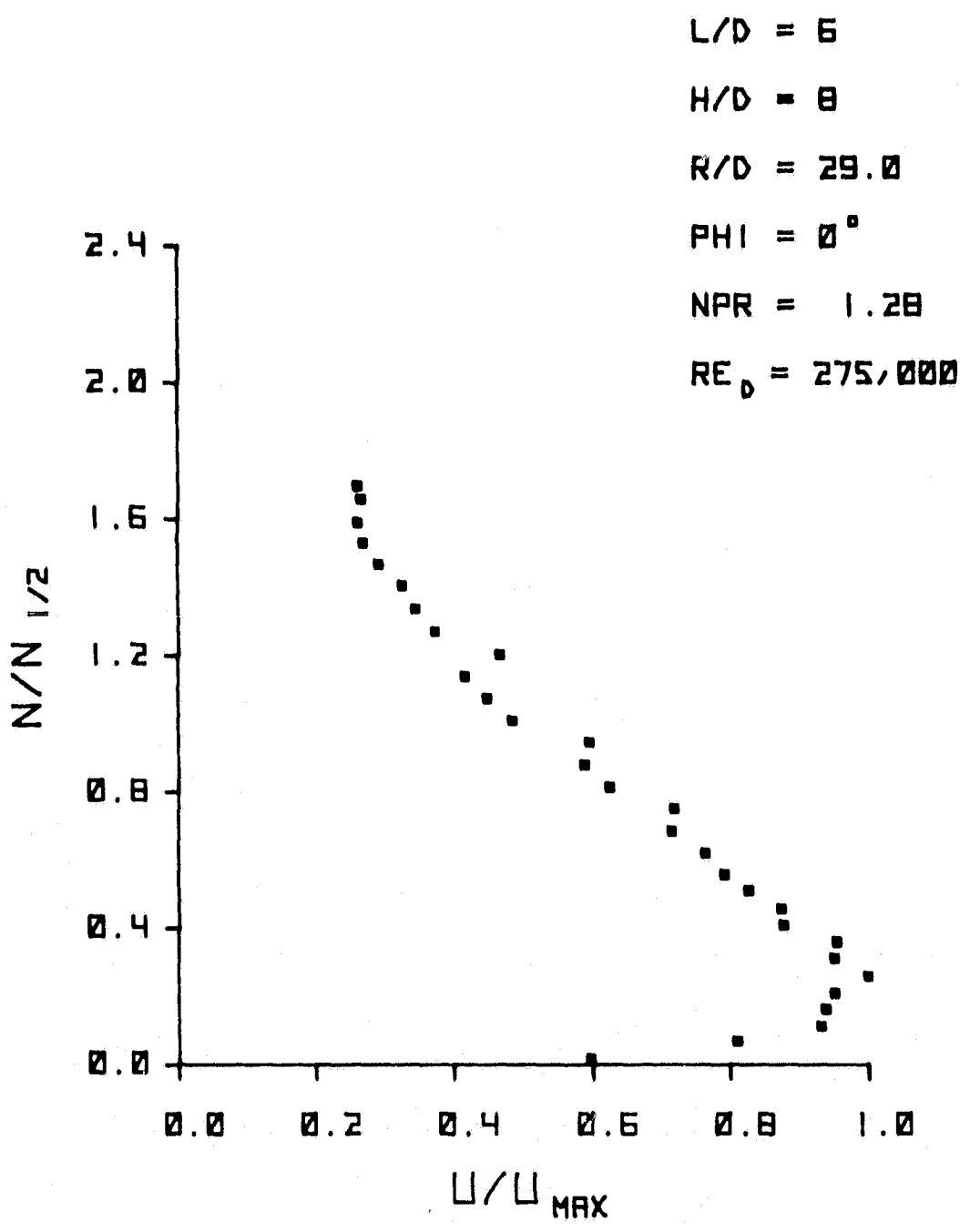

GP78-0770-62

FIGURE 21
WALL JET VELOCITY PROFILE

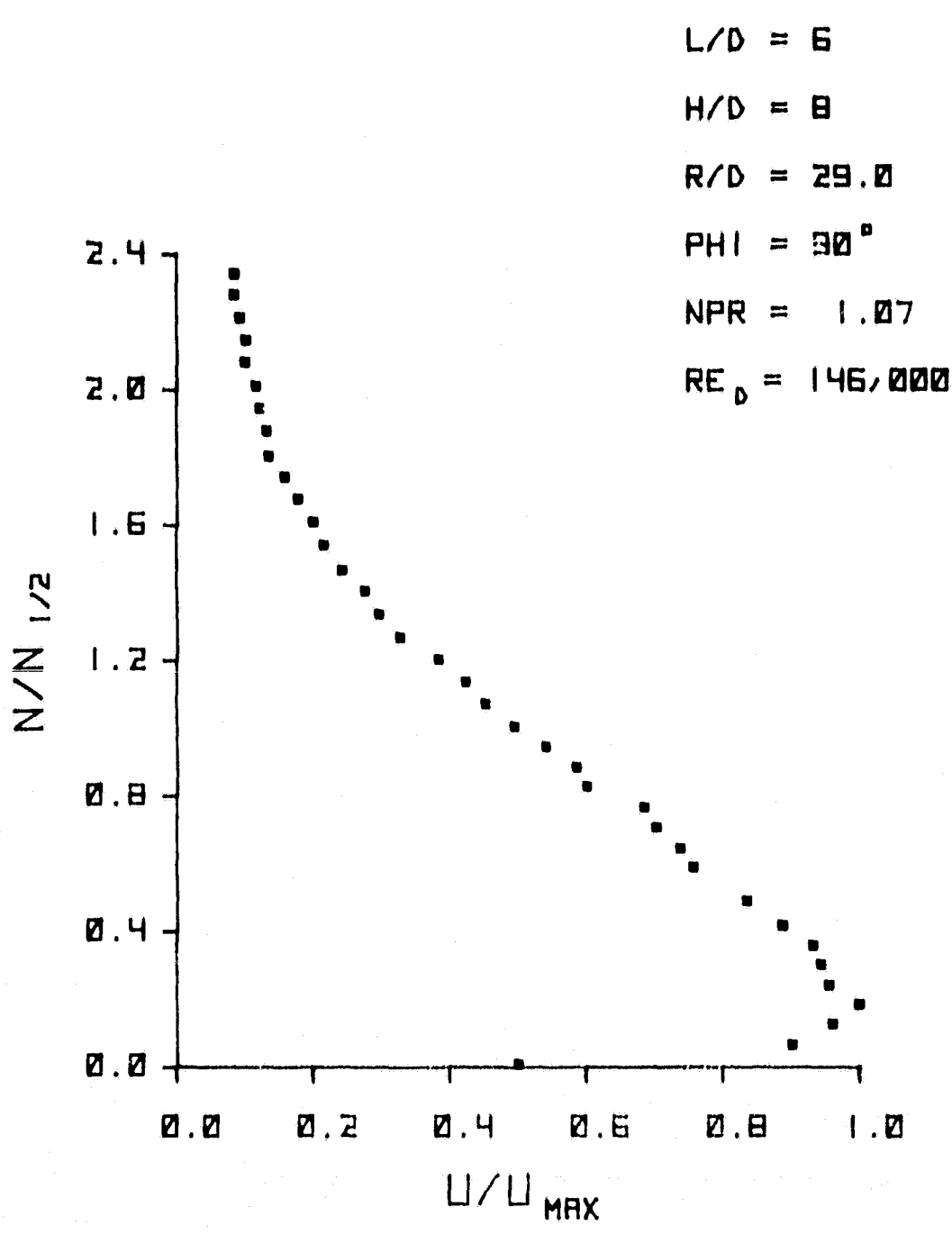

FIGURE 22
WALL JET VELOCITY PROFILE

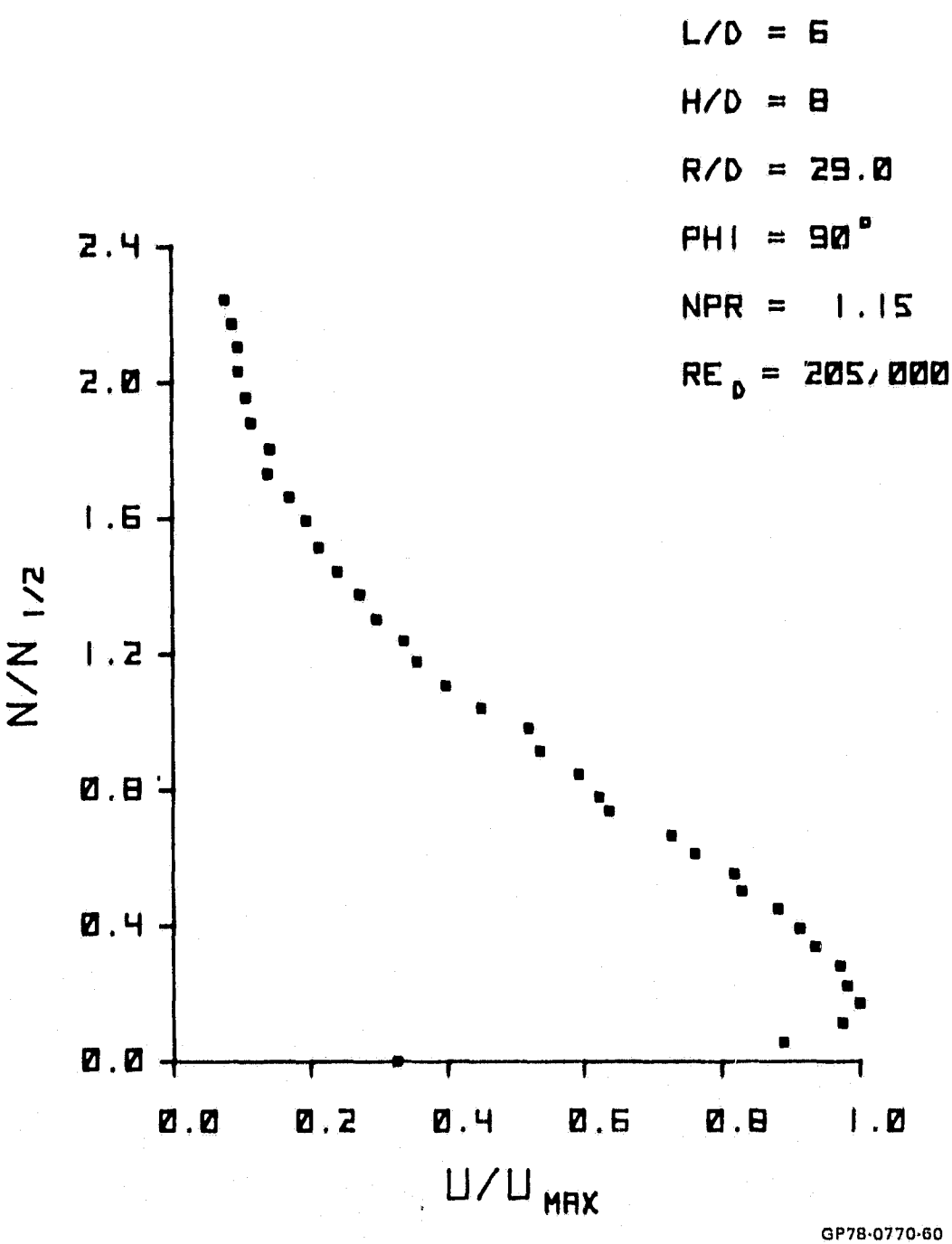

GP78-0770-60

FIGURE 23
WALL JET VELOCITY PROFILE

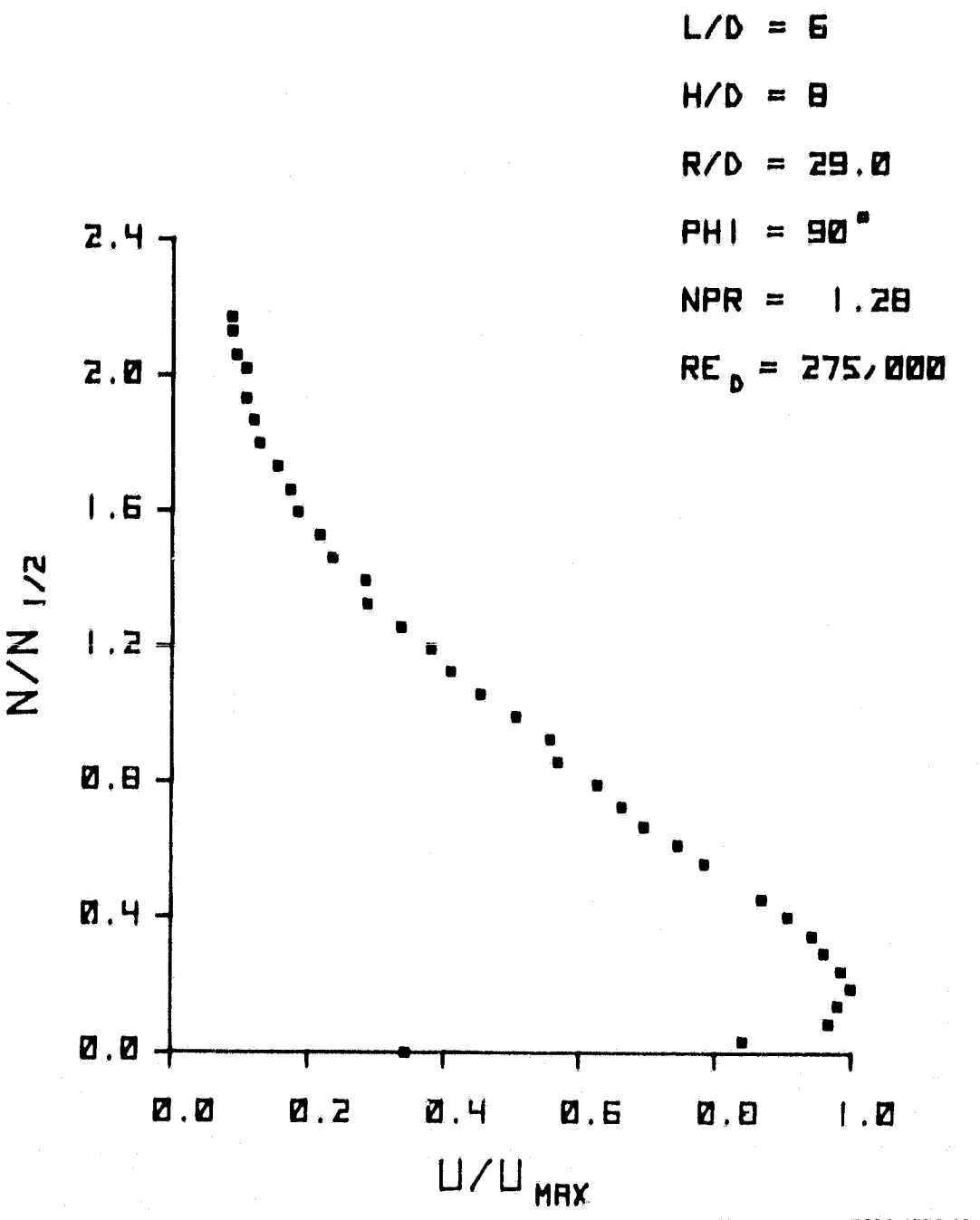

GP78-0770-66

FIGURE 24
WALL JET VELOCITY PROFILE

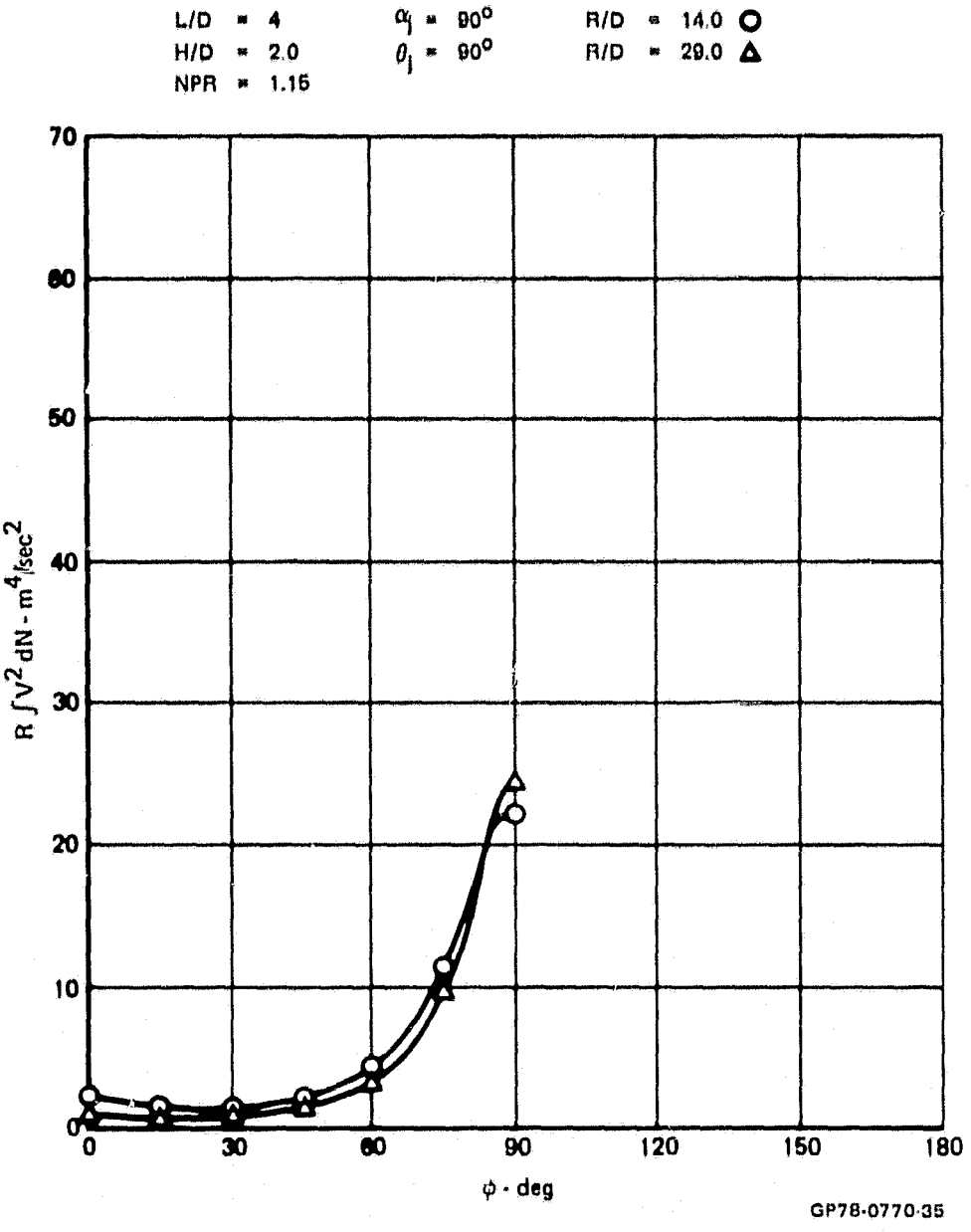

FIGURE 25
AZIMUTHAL DISTRIBUTION OF WALL JET RADIAL MOMENTUM FLUX
Vertical Impingement

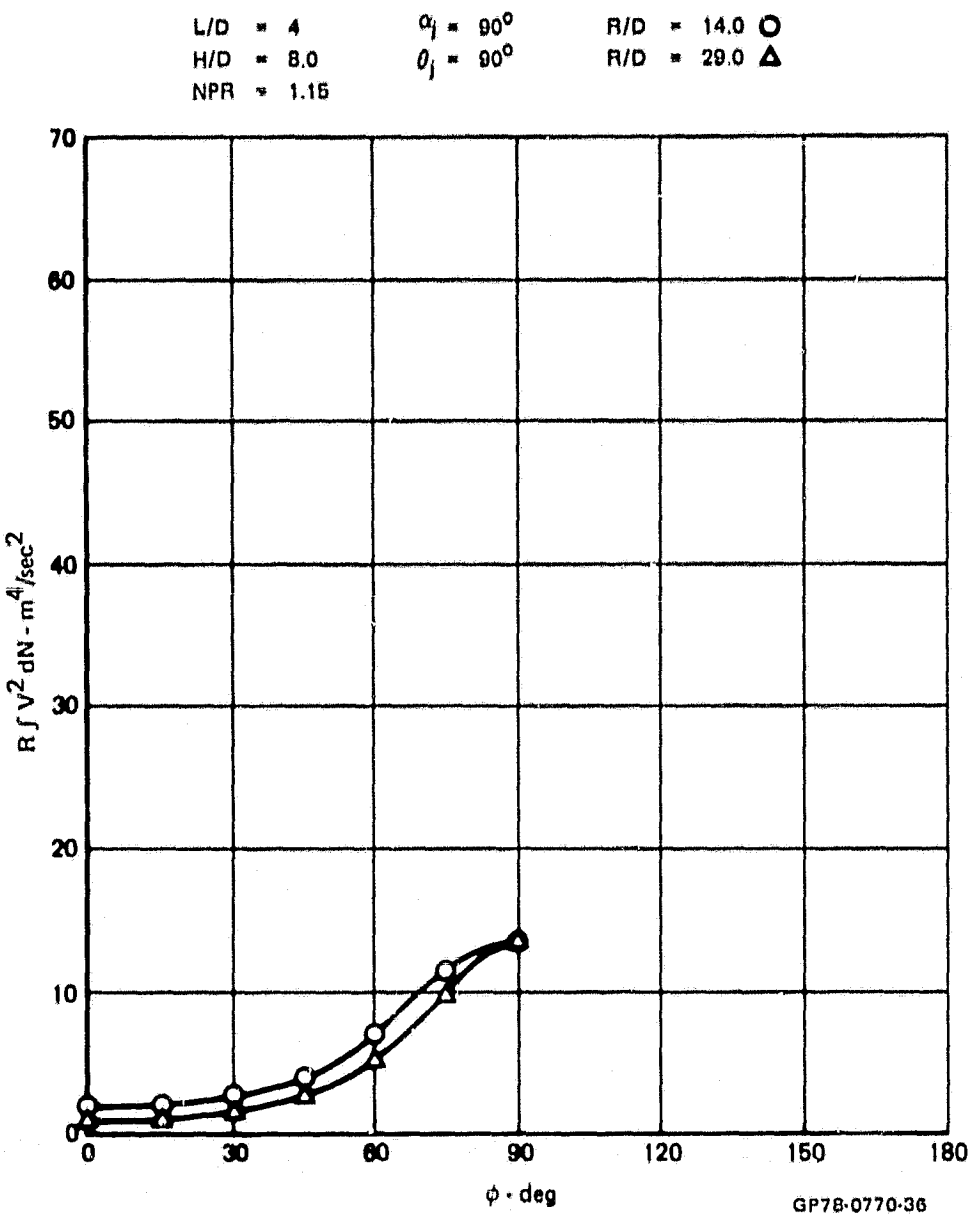

FIGURE 26
AZIMUTHAL DISTRIBUTION OF WALL JET RADIAL MOMENTUM FLUX
Vertical Impingement

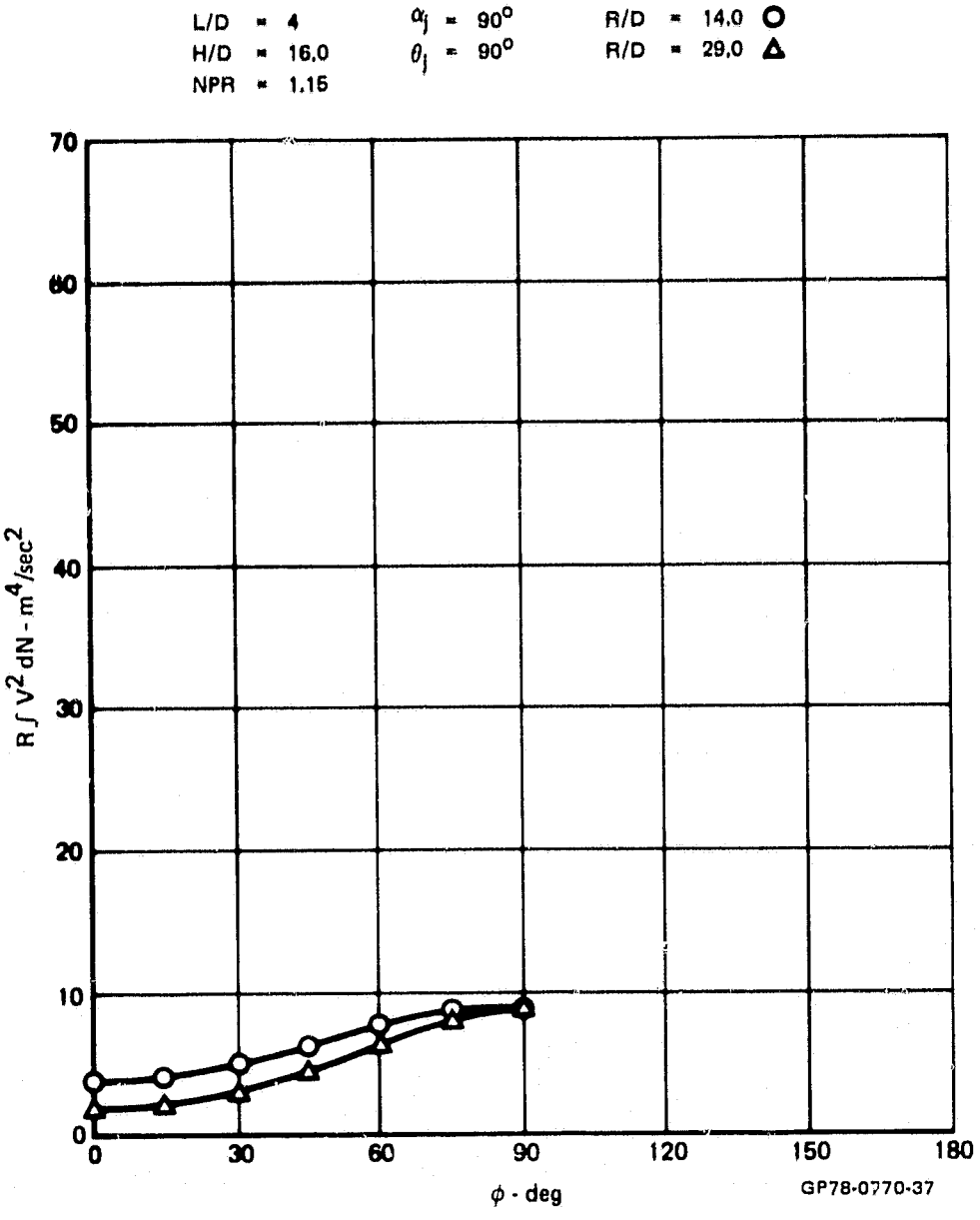

FIGURE 27
AZIMUTHAL DISTRIBUTION OF WALL JET RADIAL MOMENTUM FLUX
Vertical Impingement

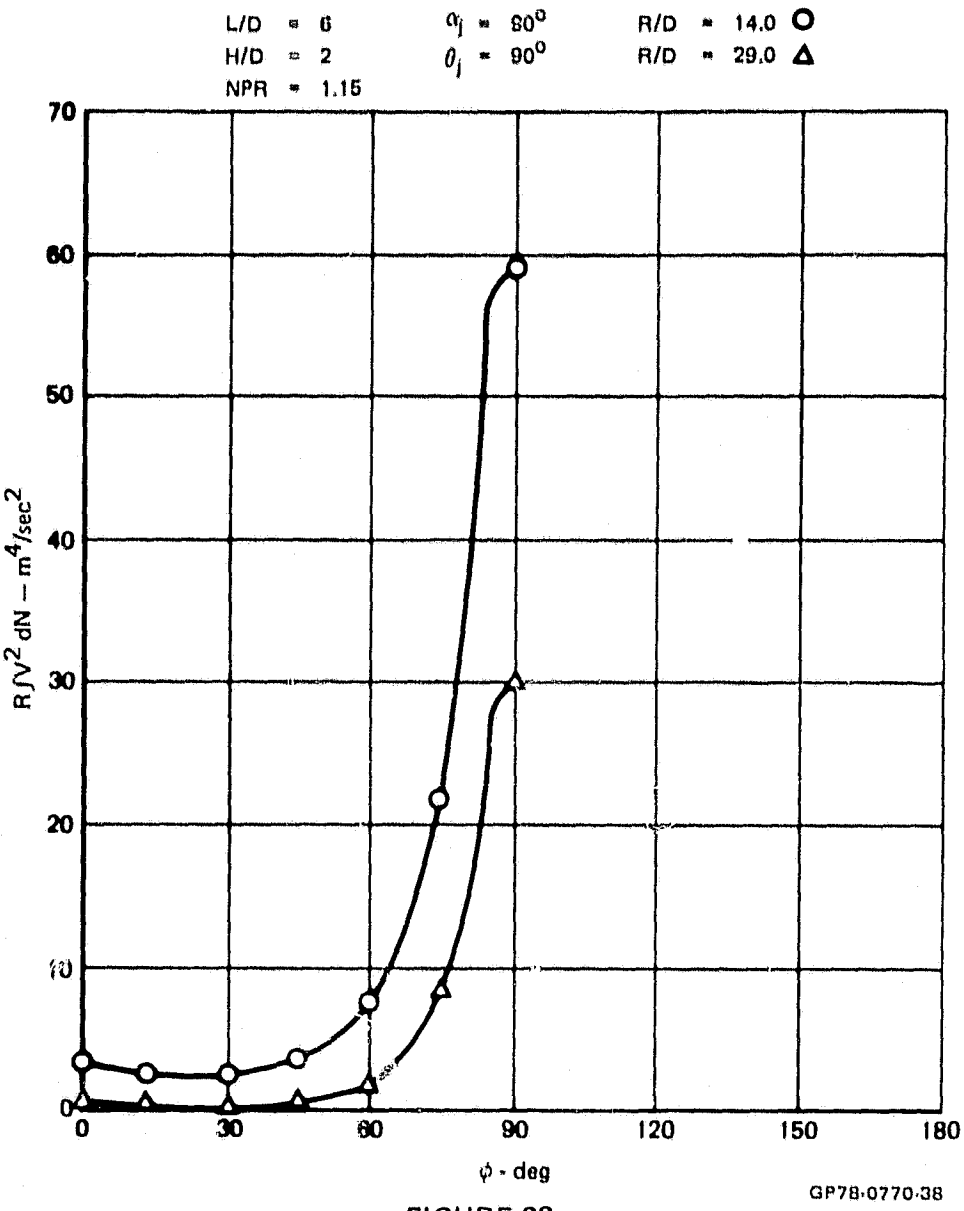

FIGURE 28

AZIMUTHAL DISTRIBUTION OF WALL JET RADIAL MOMENTUM FLUX

Vertical Impingement

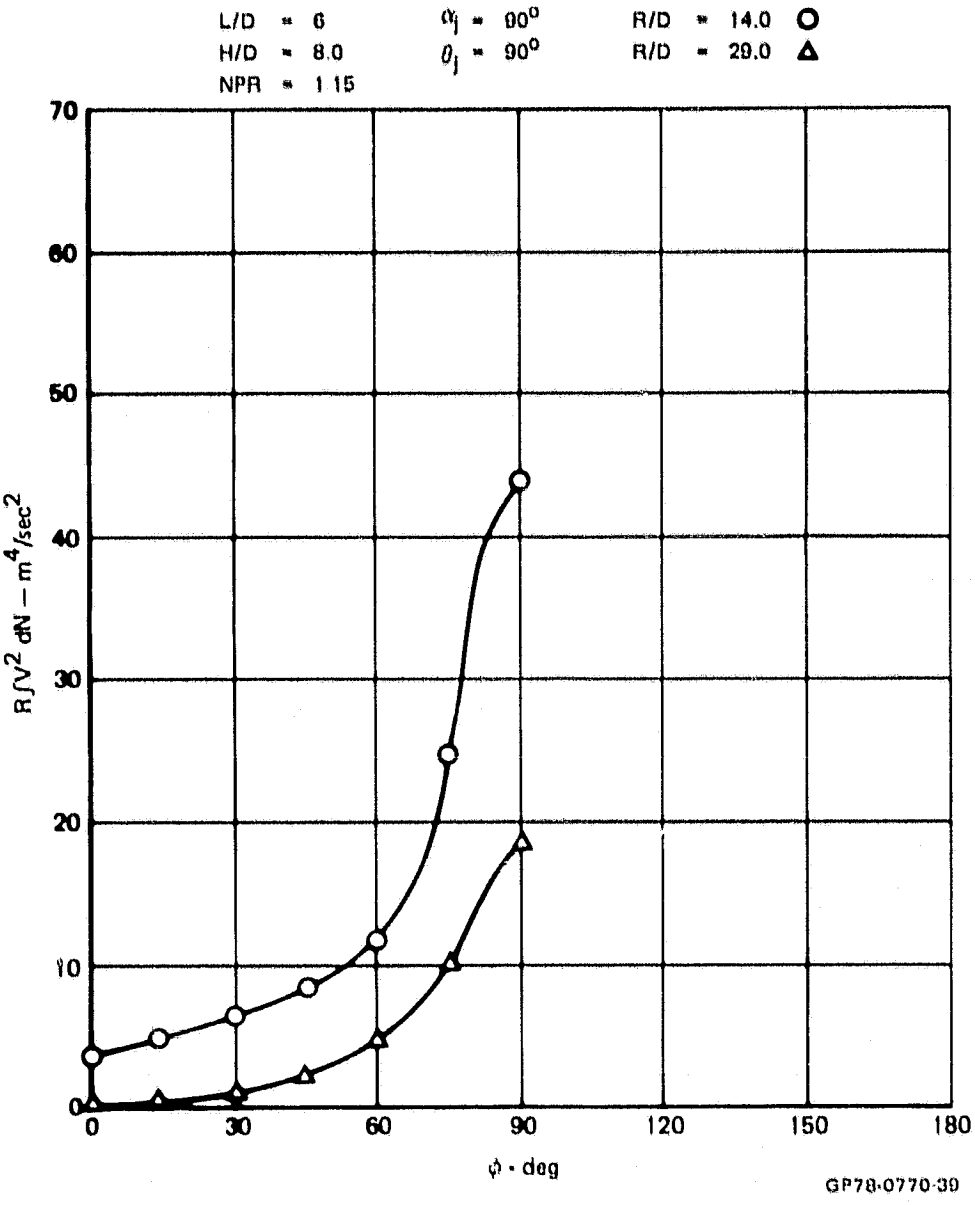

FIGURE 29
AZIMUTHAL DISTRIBUTION OF WALL JET RADIAL MOMENTUM FLUX
Vertical Impingement

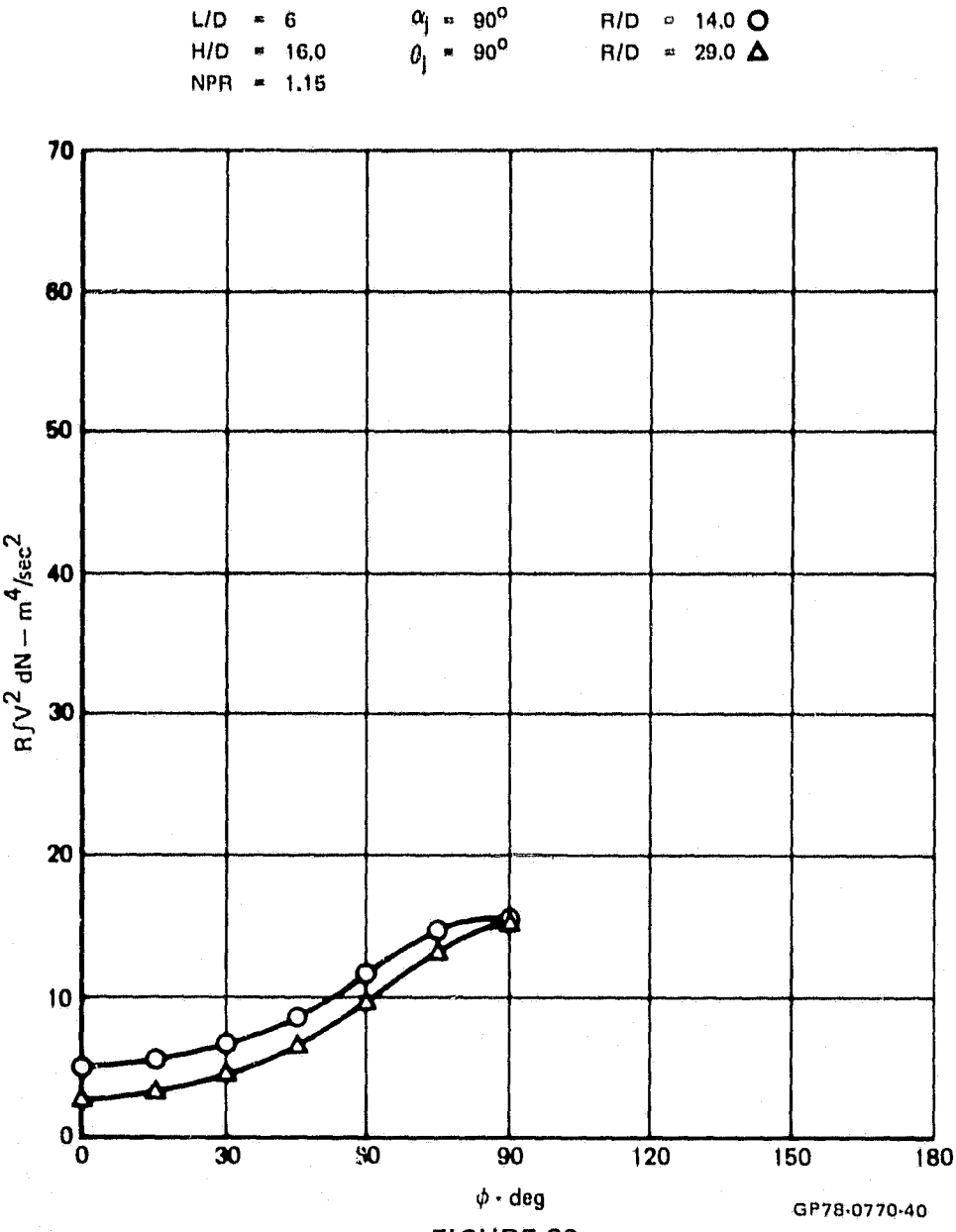

FIGURE 30

AZIMUTHAL DISTRIBUTION OF WALL JET RADIAL MOMENTUM FLUX

Vertical Impingement

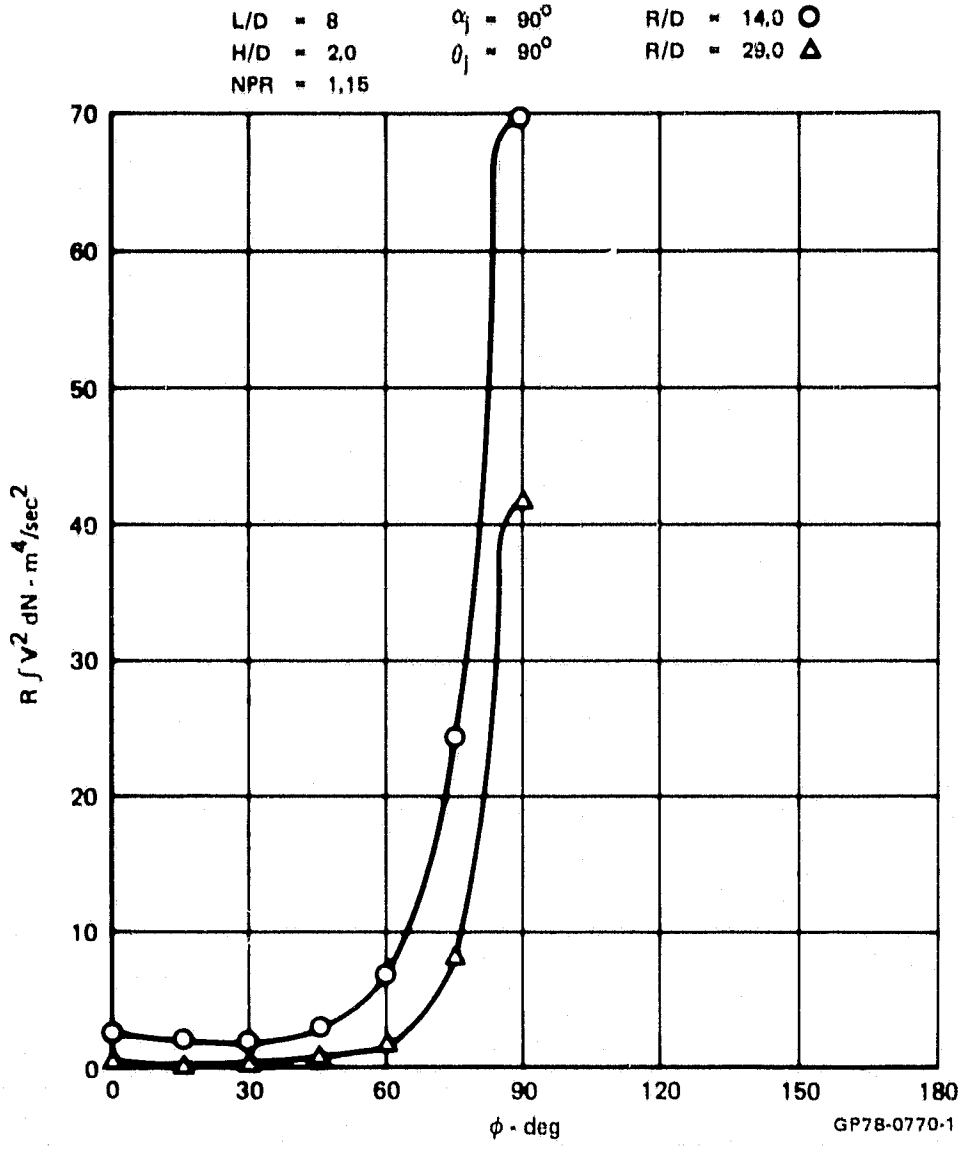

FIGURE 31
AZIMUTHAL DISTRIBUTION OF WALL JET RADIAL MOMENTUM FLUX
Vertical Impingement

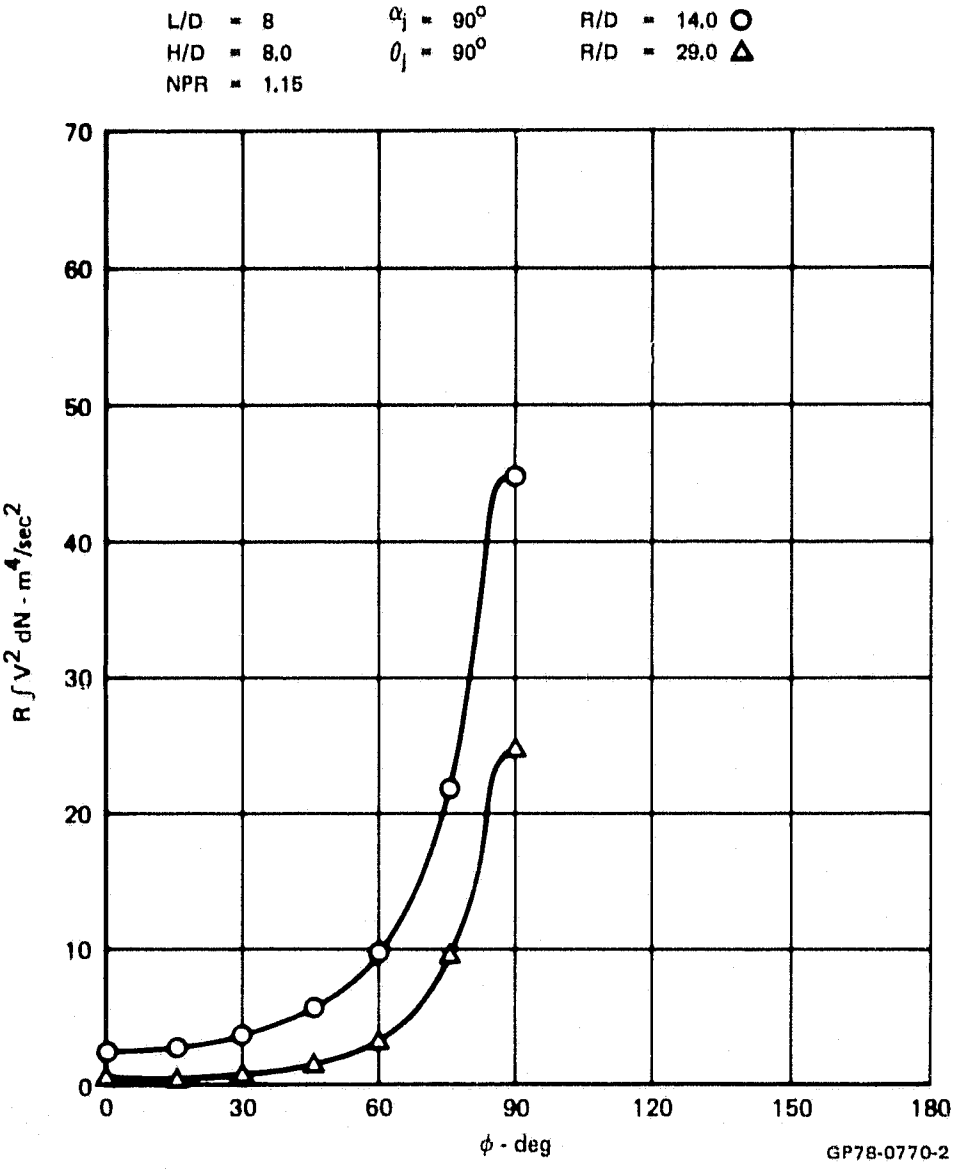

FIGURE 32
AZIMUTHAL DISTRIBUTION OF WALL JET RADIAL MOMENTUM FLUX
Vertical Impingement

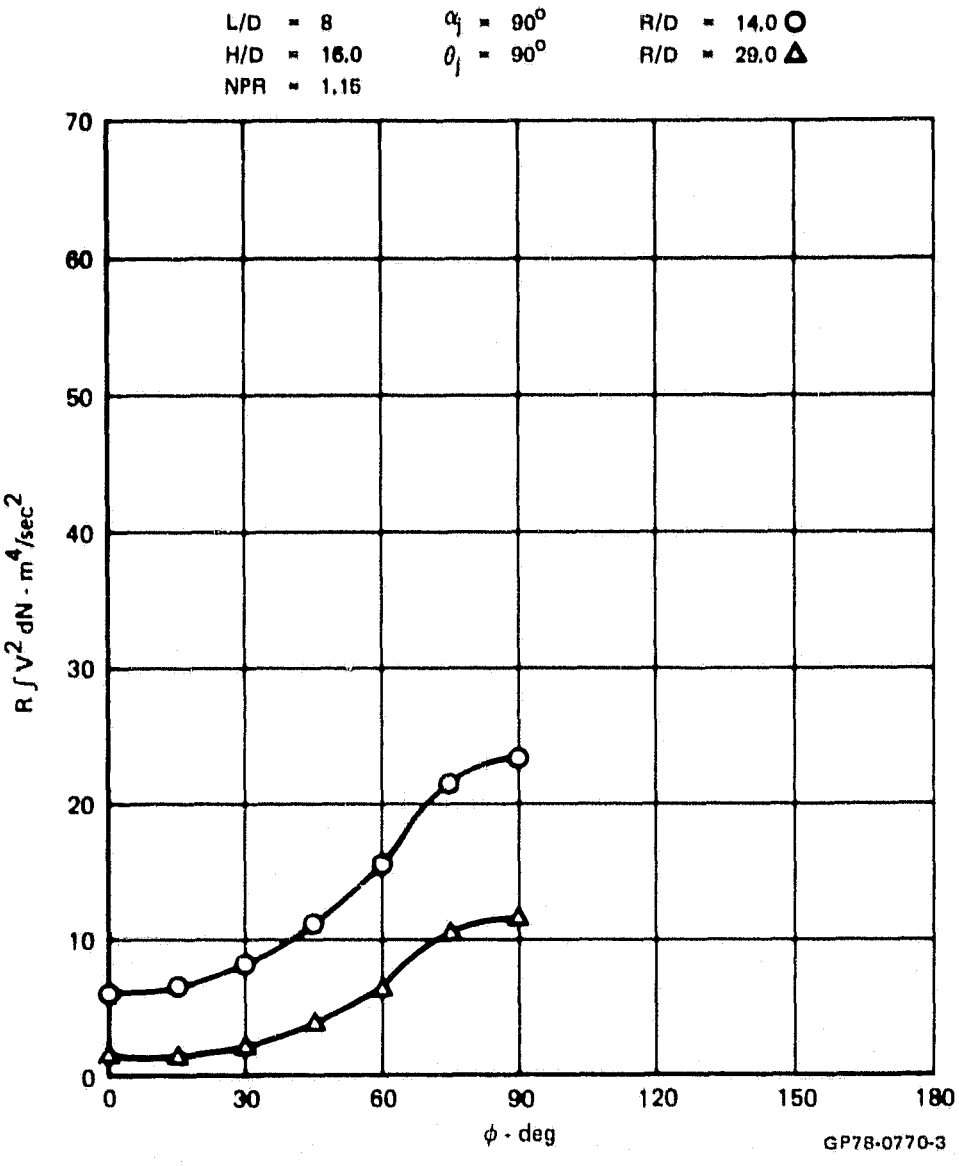

FIGURE 33
AZIMUTHAL DISTRIBUTION OF WALL JET RADIAL MOMENTUM FLUX
Vertical Impingement

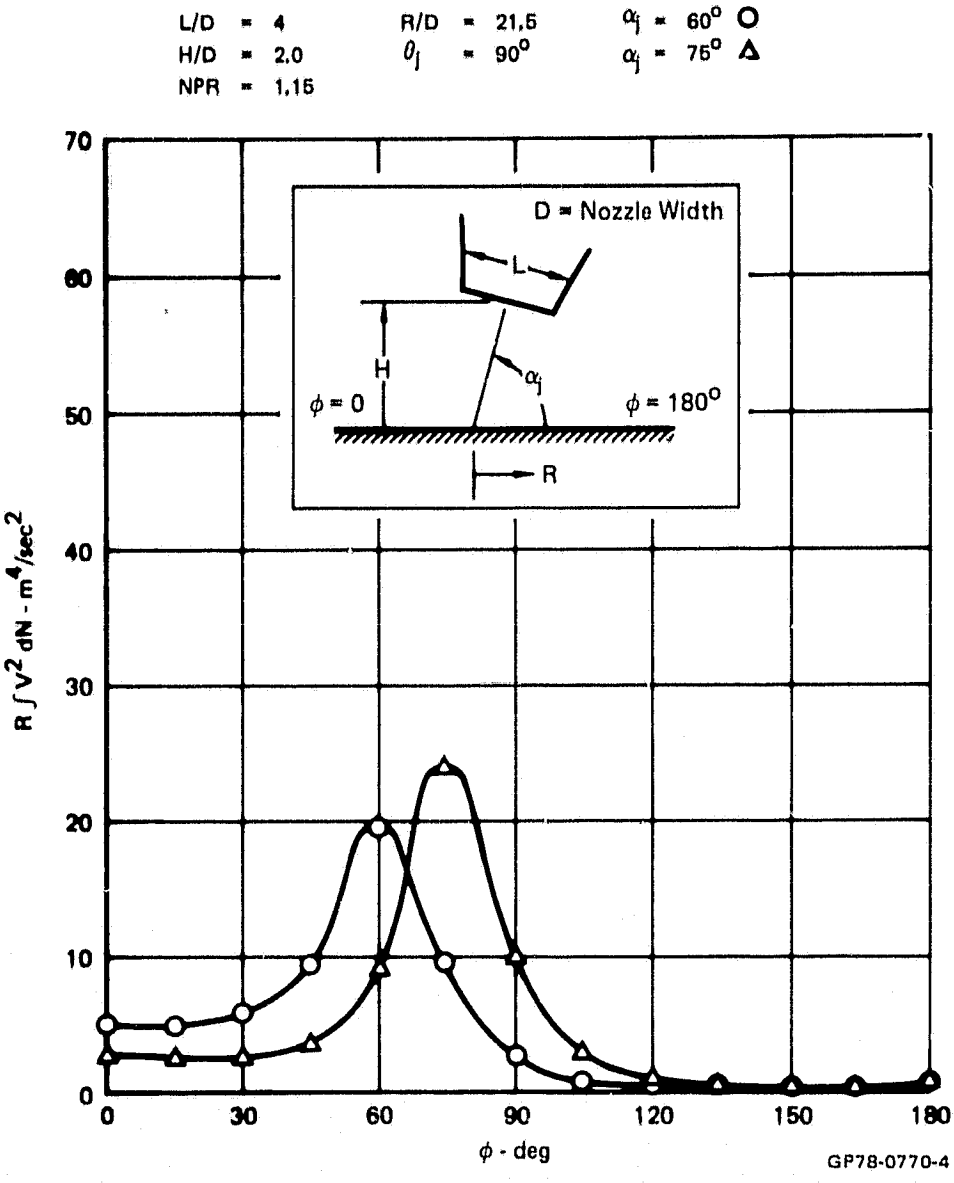

FIGURE 34

AZIMUTHAL DISTRIBUTION OF WALL JET RADIAL MOMENTUM FLUX

Oblique Impingement - Pitch

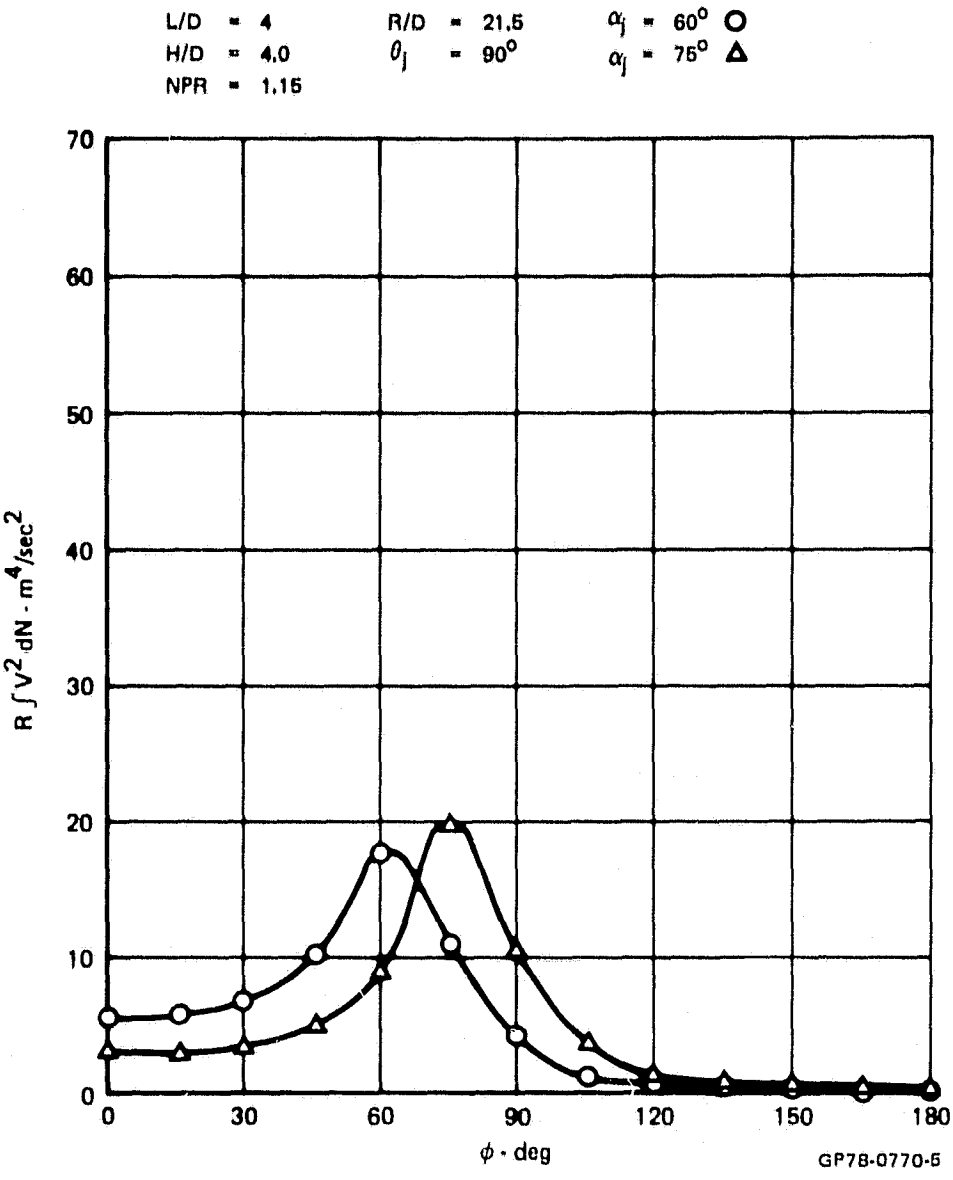

FIGURE 35
AZIMUTHAL DISTRIBUTION OF WALL JET RADIAL MOMENTUM FLUX
Oblique Impingement - Pitch

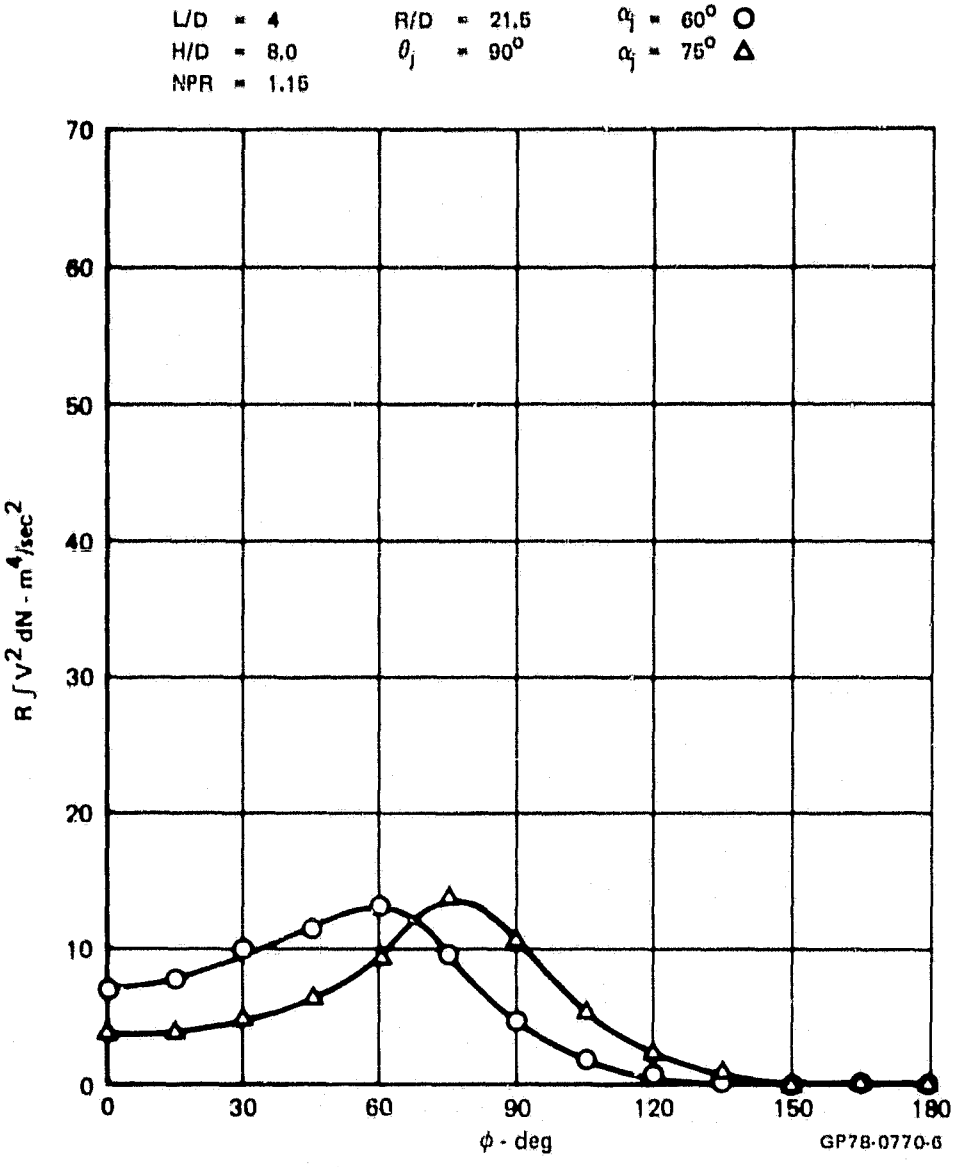

FIGURE 36
AZIMUTHAL DISTRIBUTION OF WALL JET RADIAL MOMENTUM FLUX
Oblique Impingement - Pitch

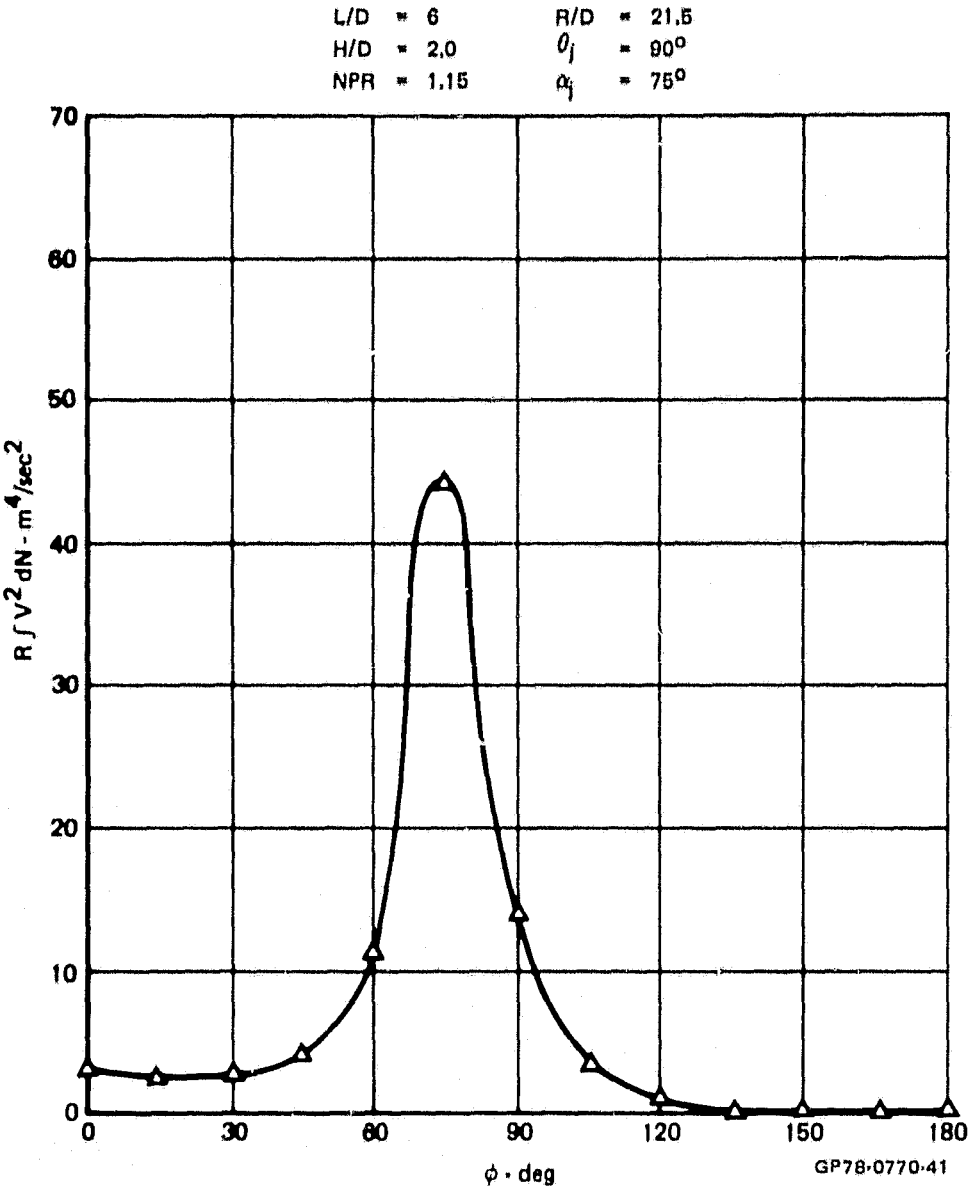

FIGURE 37
AZIMUTHAL DISTRIBUTION OF WALL JET RADIAL MOMENTUM FLUX
Oblique Impingement - Pitch

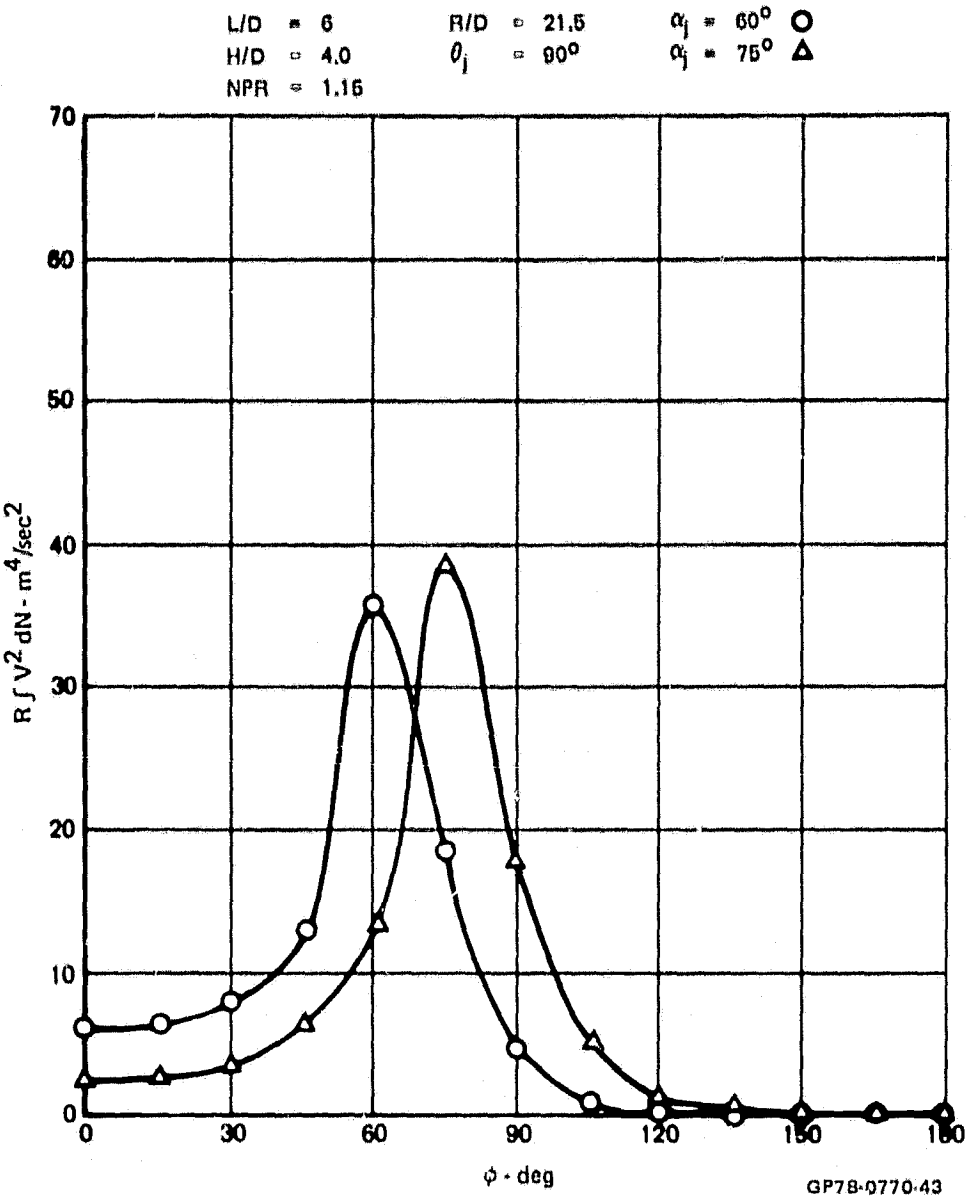

FIGURE 38

AZIMUTHAL DISTRIBUTION OF WALL JET RADIAL MOMENTUM FLUX

Oblique Impingement - Pitch

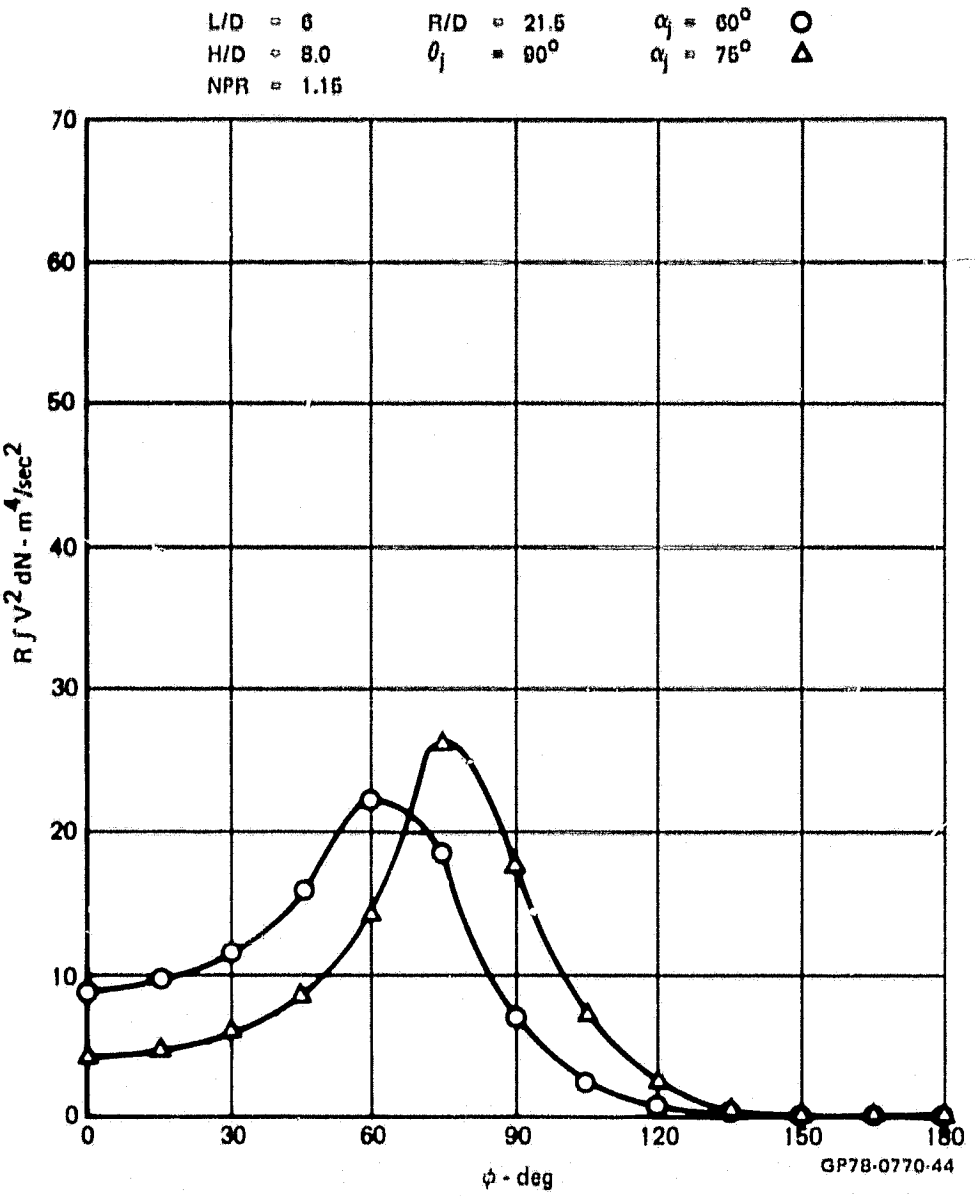

FIGURE 39

AZIMUTHAL DISTRIBUTION OF WALL JET RADIAL MOMENTUM FLUX

Oblique Impingement - Pitch

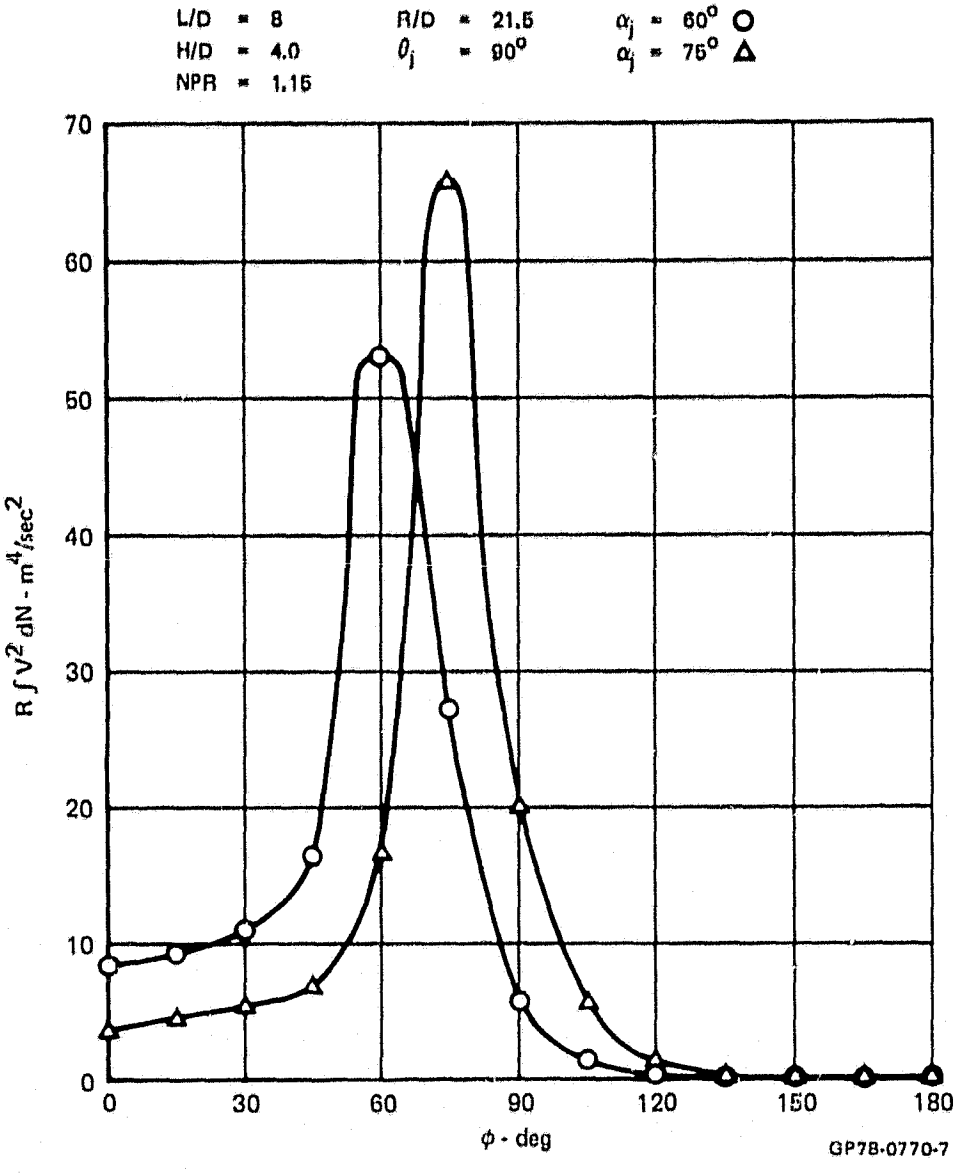

FIGURE 40
AZIMUTHAL DISTRIBUTION OF WALL JET RADIAL MOMENTUM FLUX
Oblique Impingement - Pitch

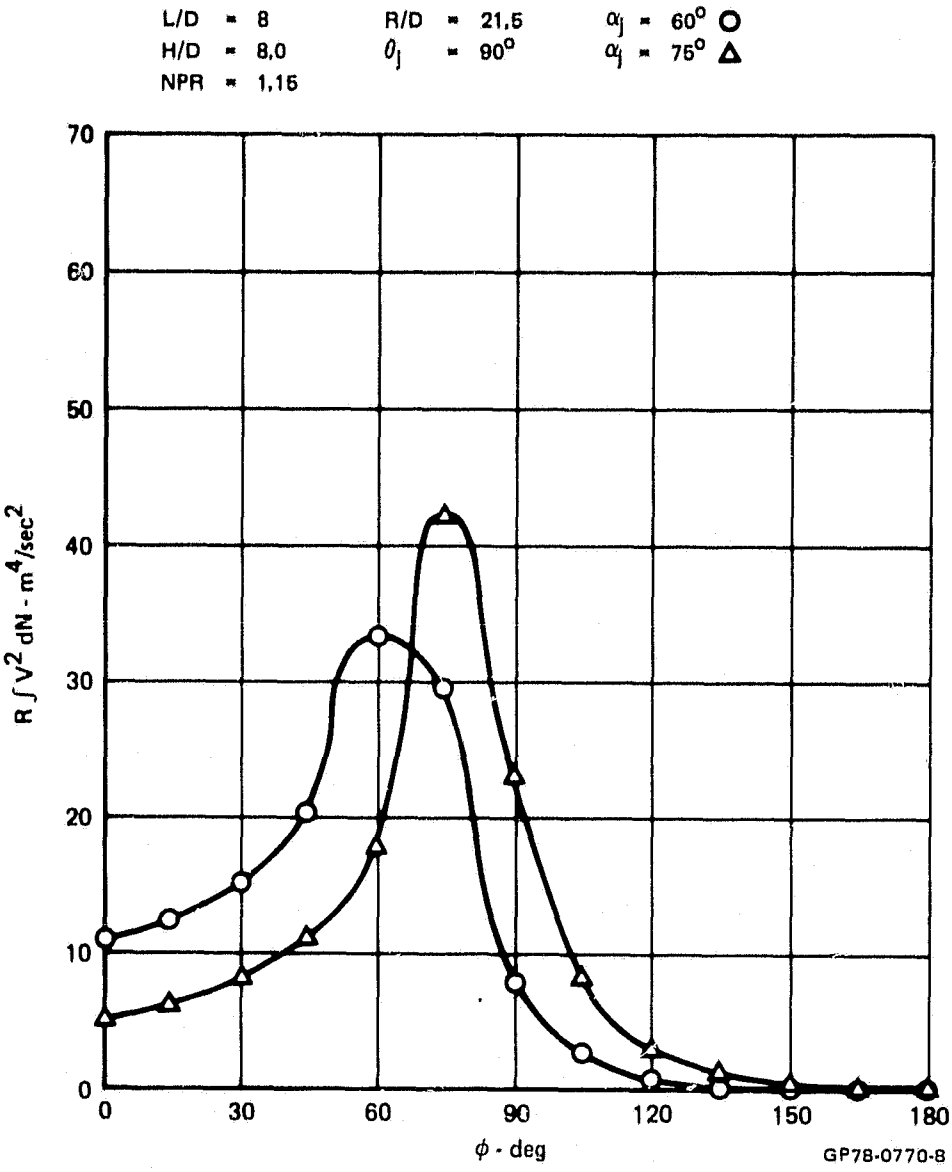

FIGURE 41
AZIMUTHAL DISTRIBUTION OF WALL JET RADIAL MOMENTUM FLUX
Oblique Impingement - Pitch

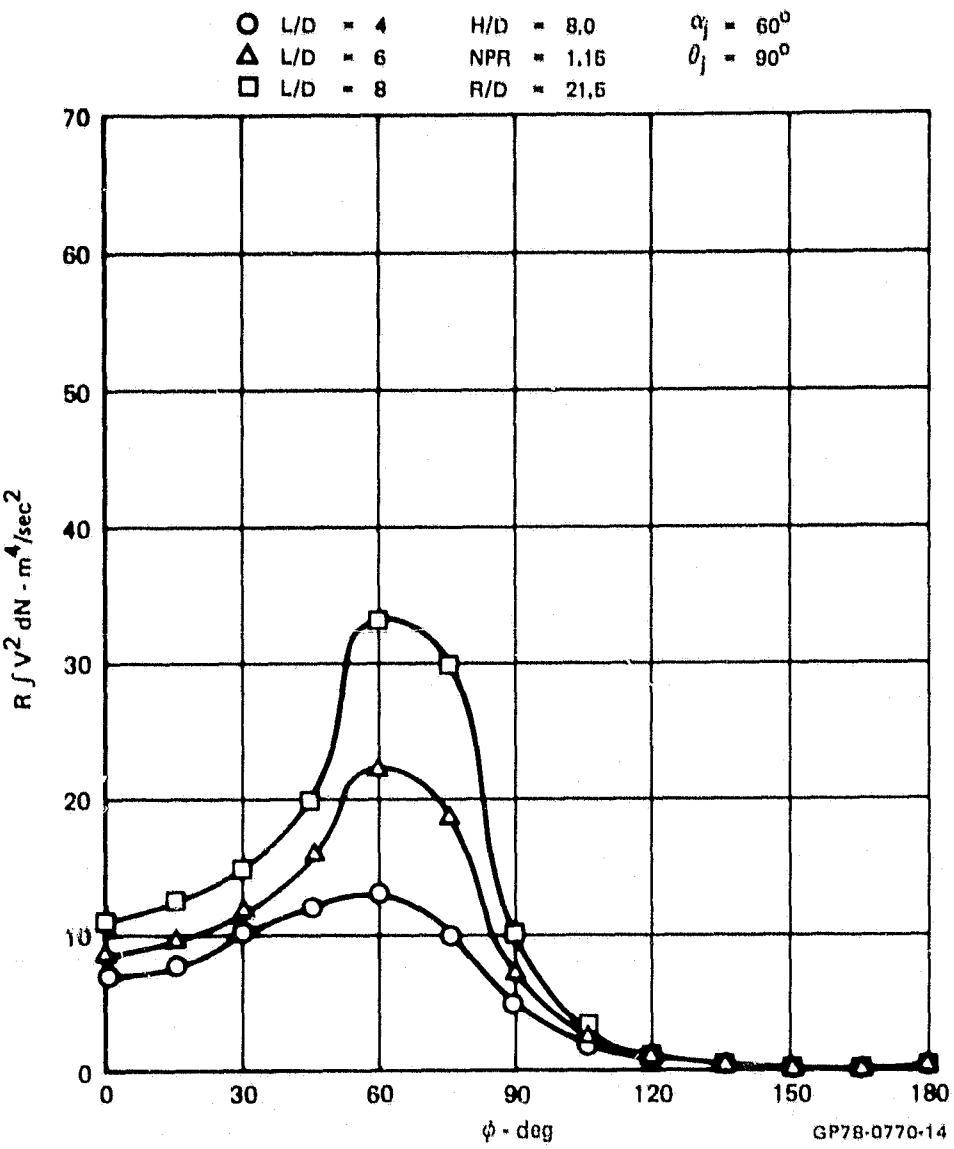

FIGURE 42

AZIMUTHAL DISTRIBUTION OF WALL JET RADIAL MOMENTUM FLUX

Oblique Impingement - Pitch

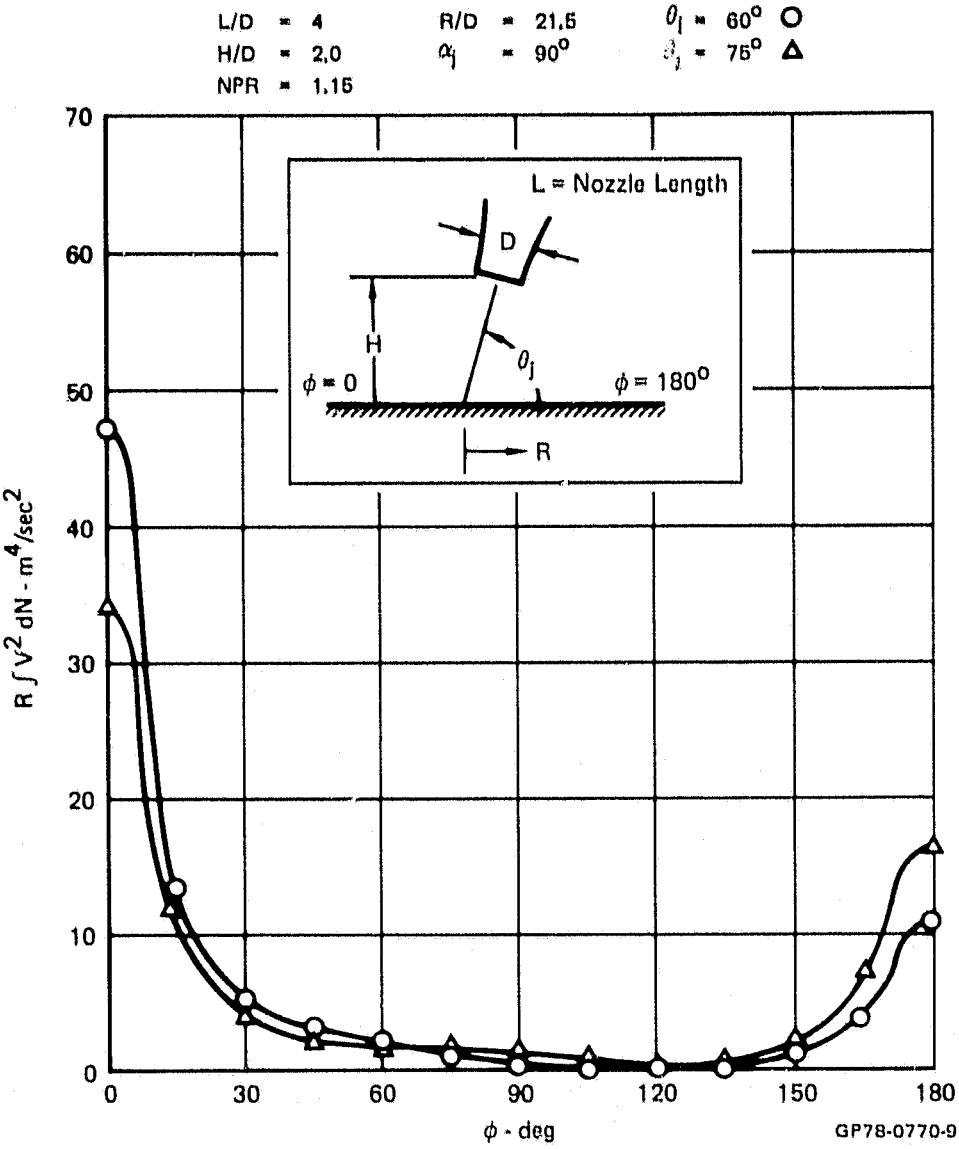

FIGURE 43

AZIMUTHAL DISTRIBUTION OF WALL JET RADIAL MOMENTUM FLUX

Oblique Impingement - Roll

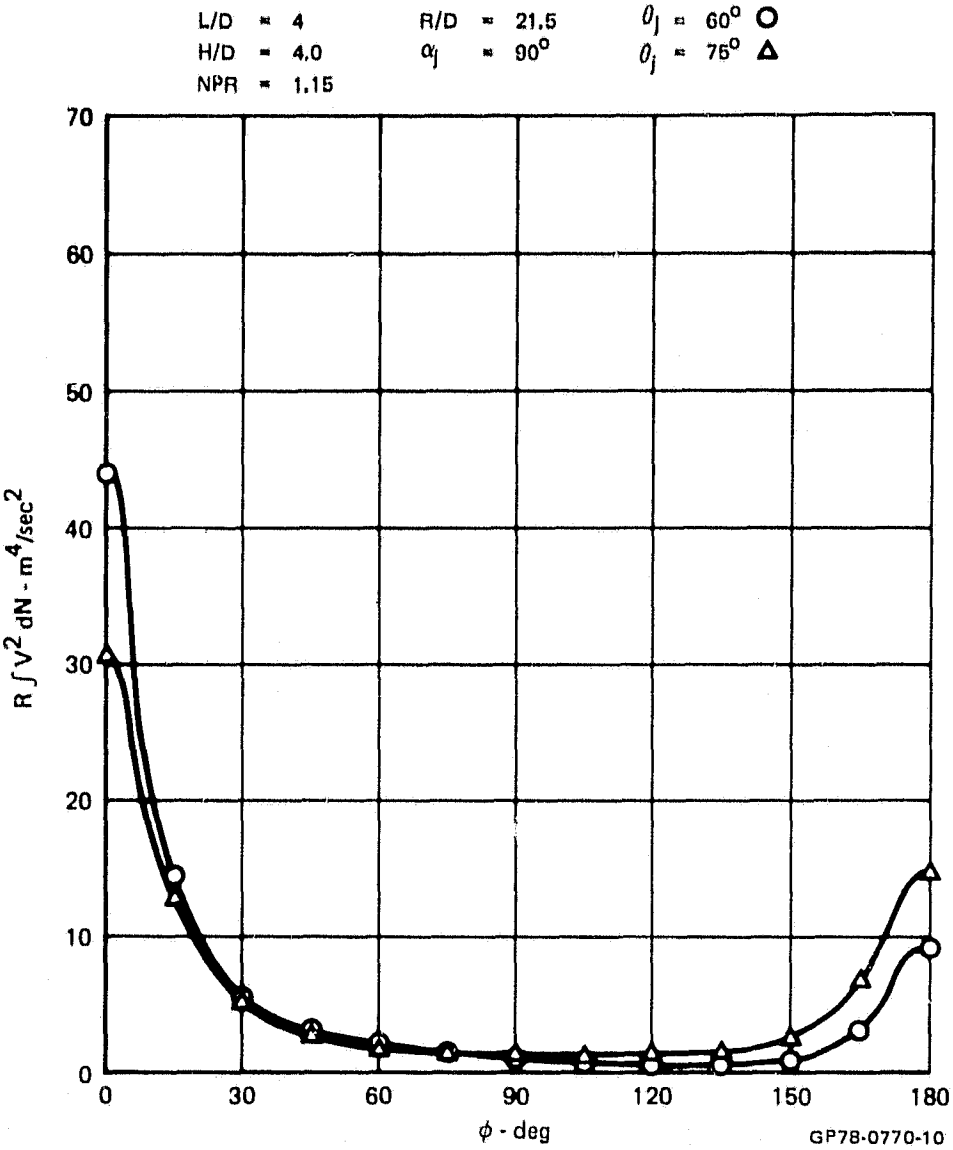

FIGURE 44
AZIMUTHAL DISTRIBUTION OF WALL JET RADIAL MOMENTUM FLUX
Oblique Impingement - Roll

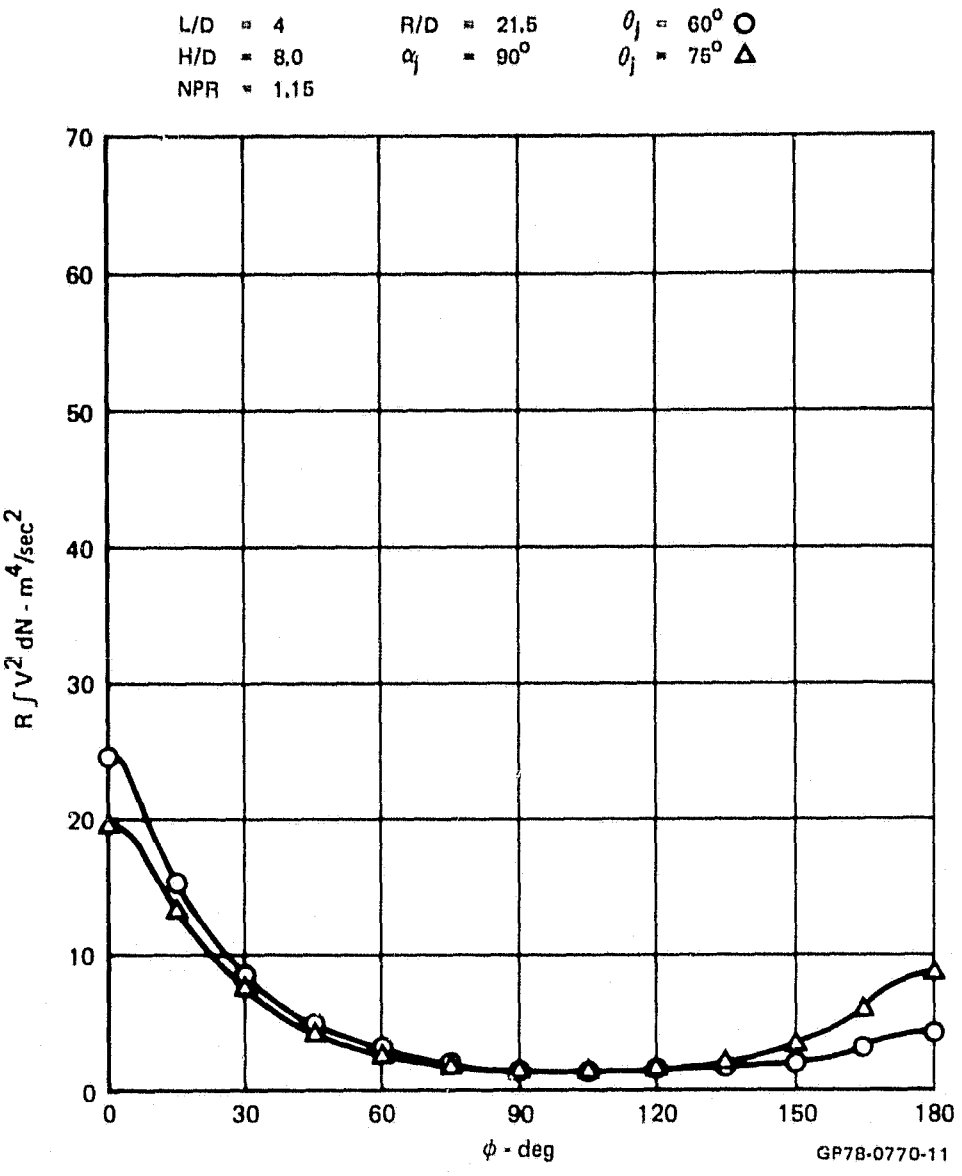

FIGURE 45

AZIMUTHAL DISTRIBUTION OF WALL JET RADIAL MOMENTUM FLUX

Oblique Impingement - Roll

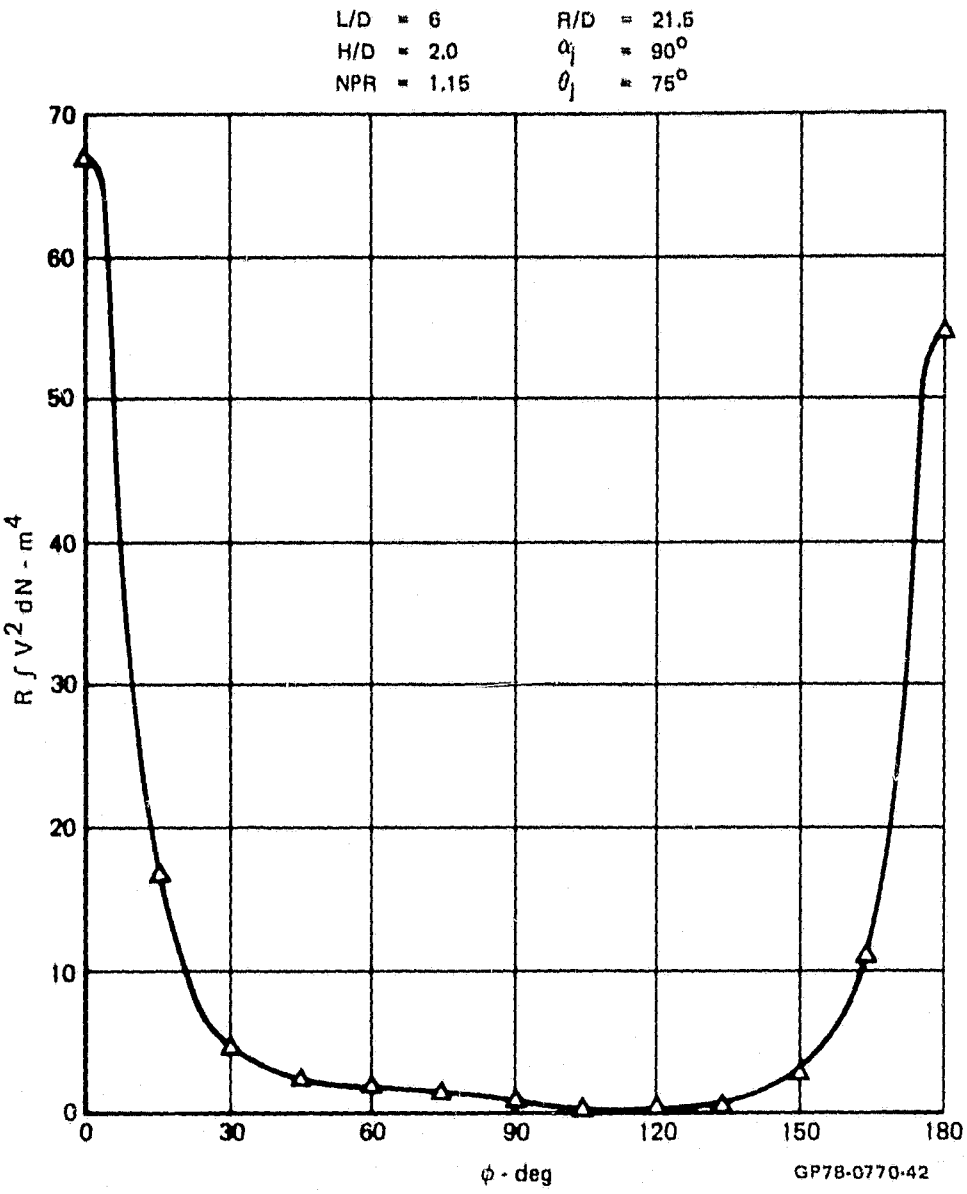

FIGURE 46
AZIMUTHAL DISTRIBUTION OF WALL JET RADIAL MOMENTUM FLUX
Oblique Impingement - Roll

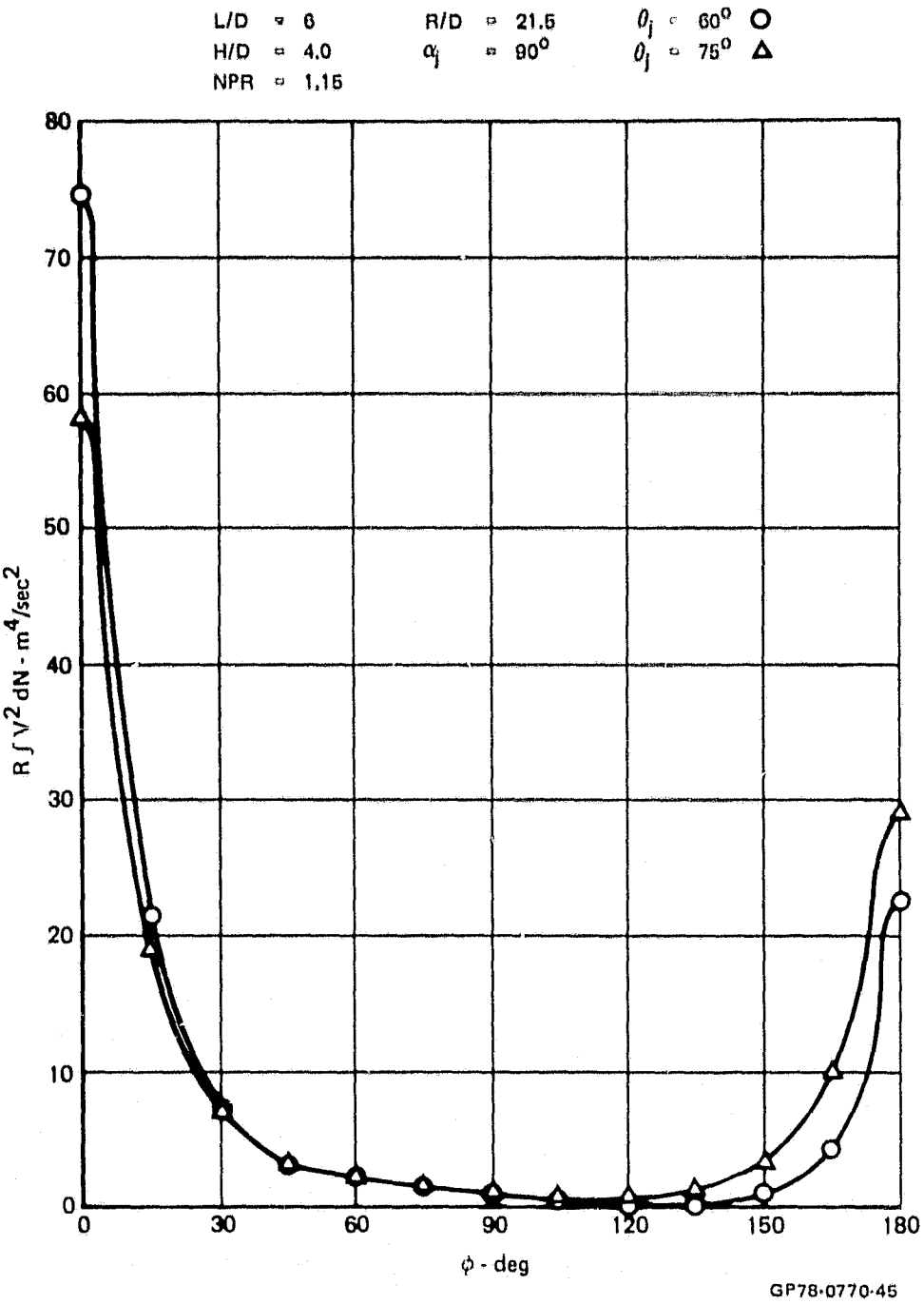

FIGURE 47
AZIMUTHAL DISTRIBUTION OF WALL JET RADIAL MOMENTUM FLUX
Oblique Impingement - Roll

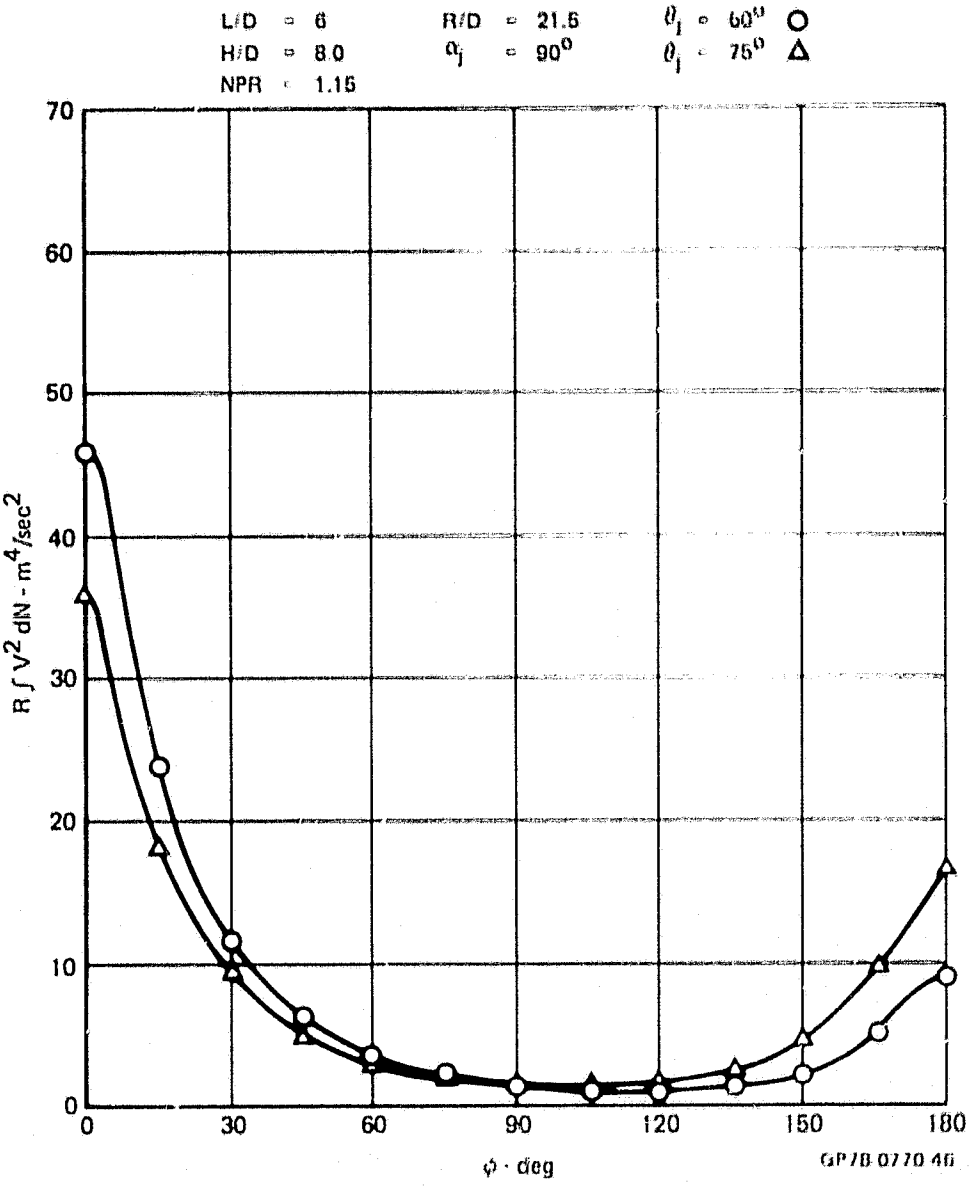

FIGURE 48

AZIMUTHAL DISTRIBUTION OF WALL JET RADIAL MOMENTUM FLUX

Oblique Impingement - Roll

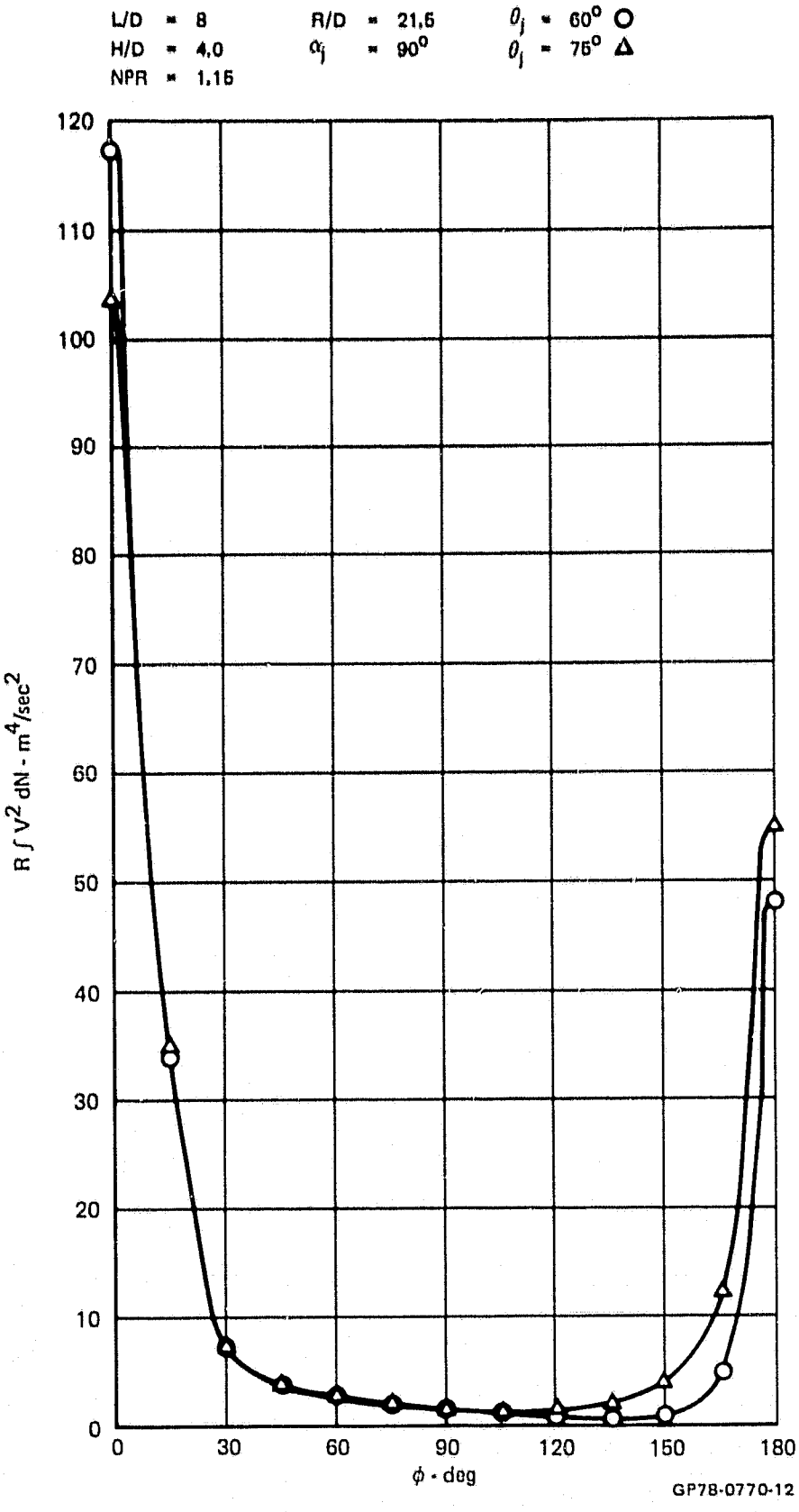

FIGURE 49
AZIMUTHAL DISTRIBUTION OF WALL JET RADIAL MOMENTUM FLUX
Oblique Impingement - Roll

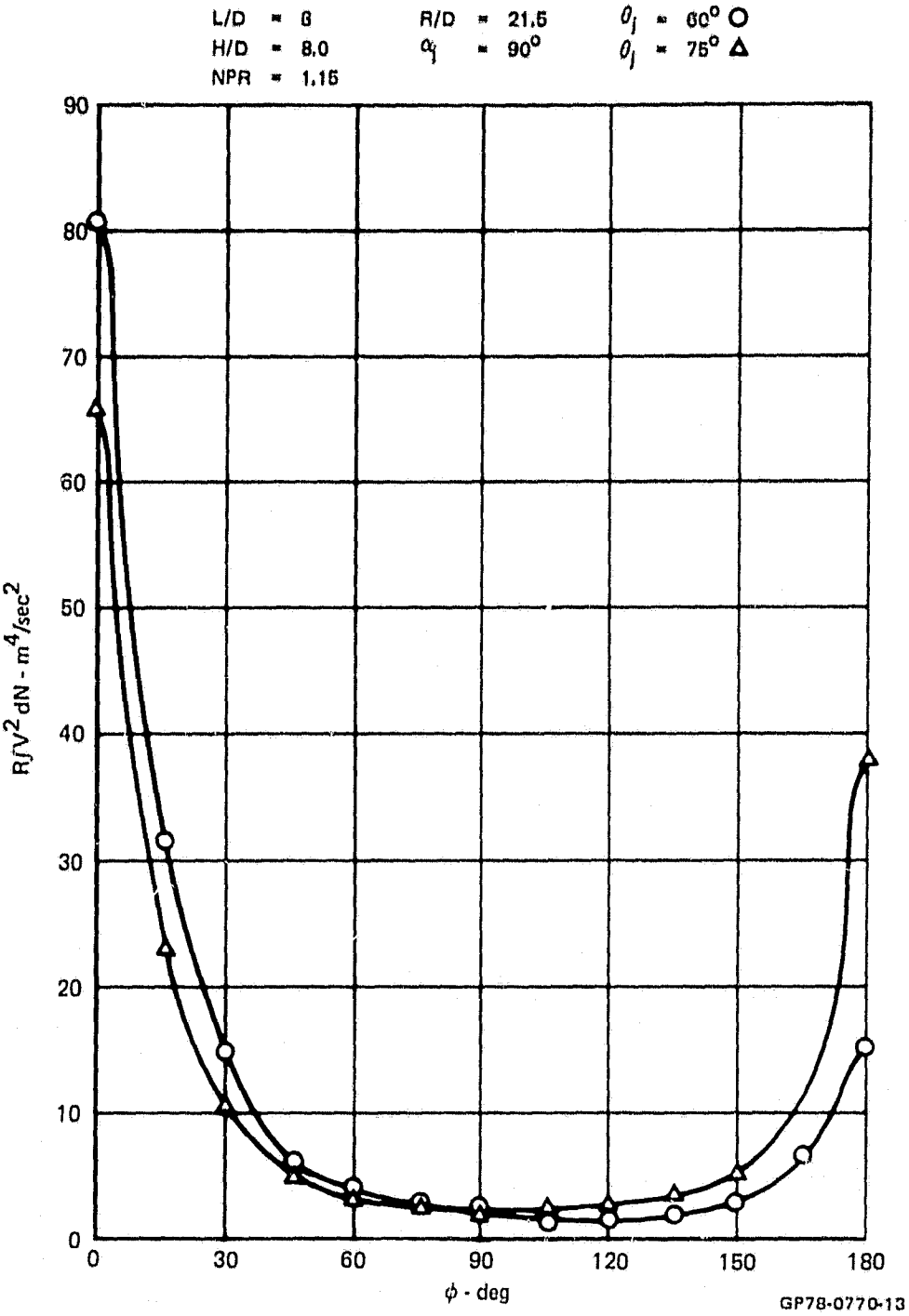

FIGURE 50
AZIMUTHAL DISTRIBUTION OF WALL JET RADIAL MOMENTUM FLUX
Oblique Impingement - Roll

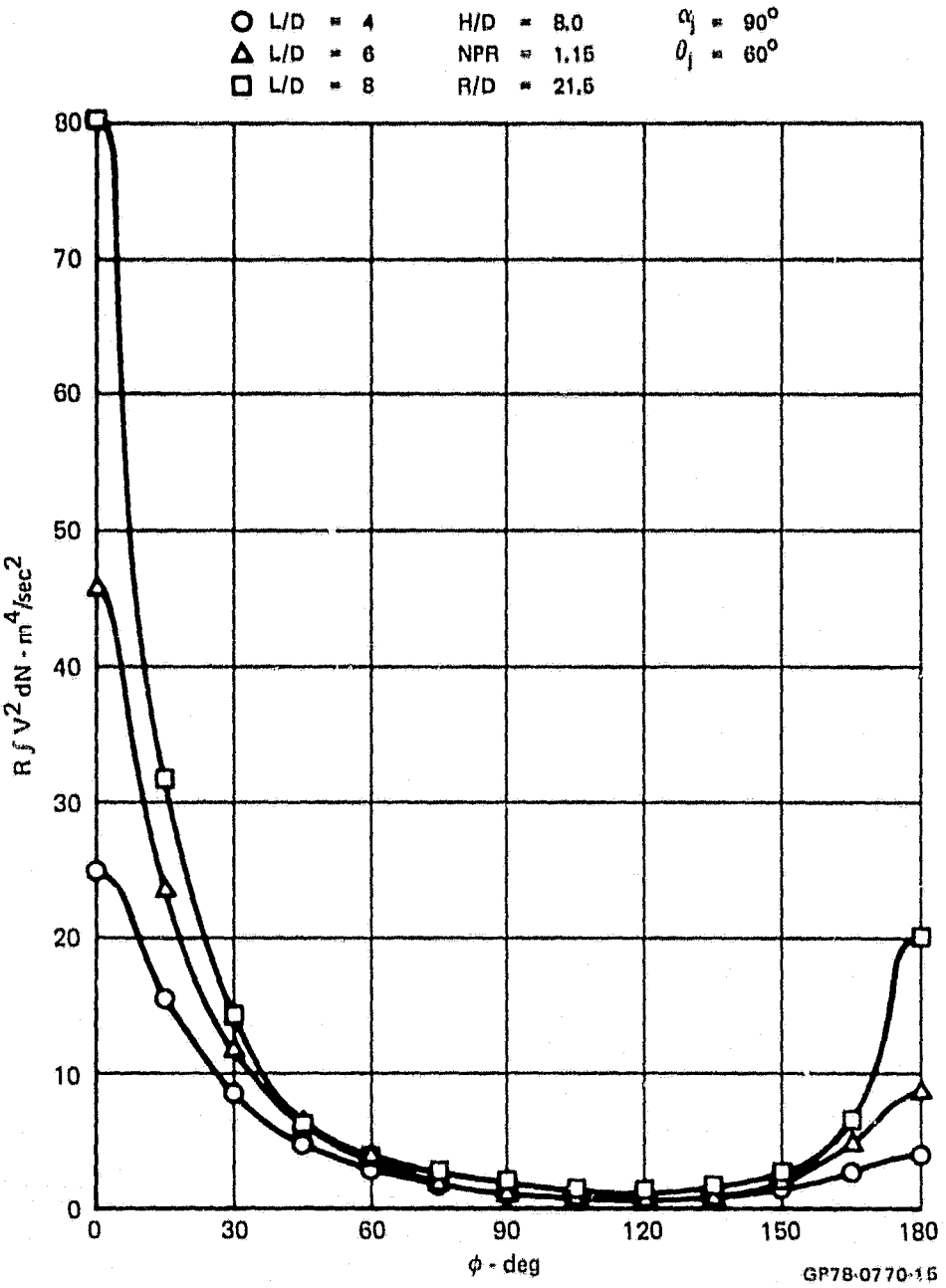

FIGURE 51
AZIMUTHAL DISTRIBUTION OF WALL JET RADIAL MOMENTUM FLUX
Oblique Impingement - Roll

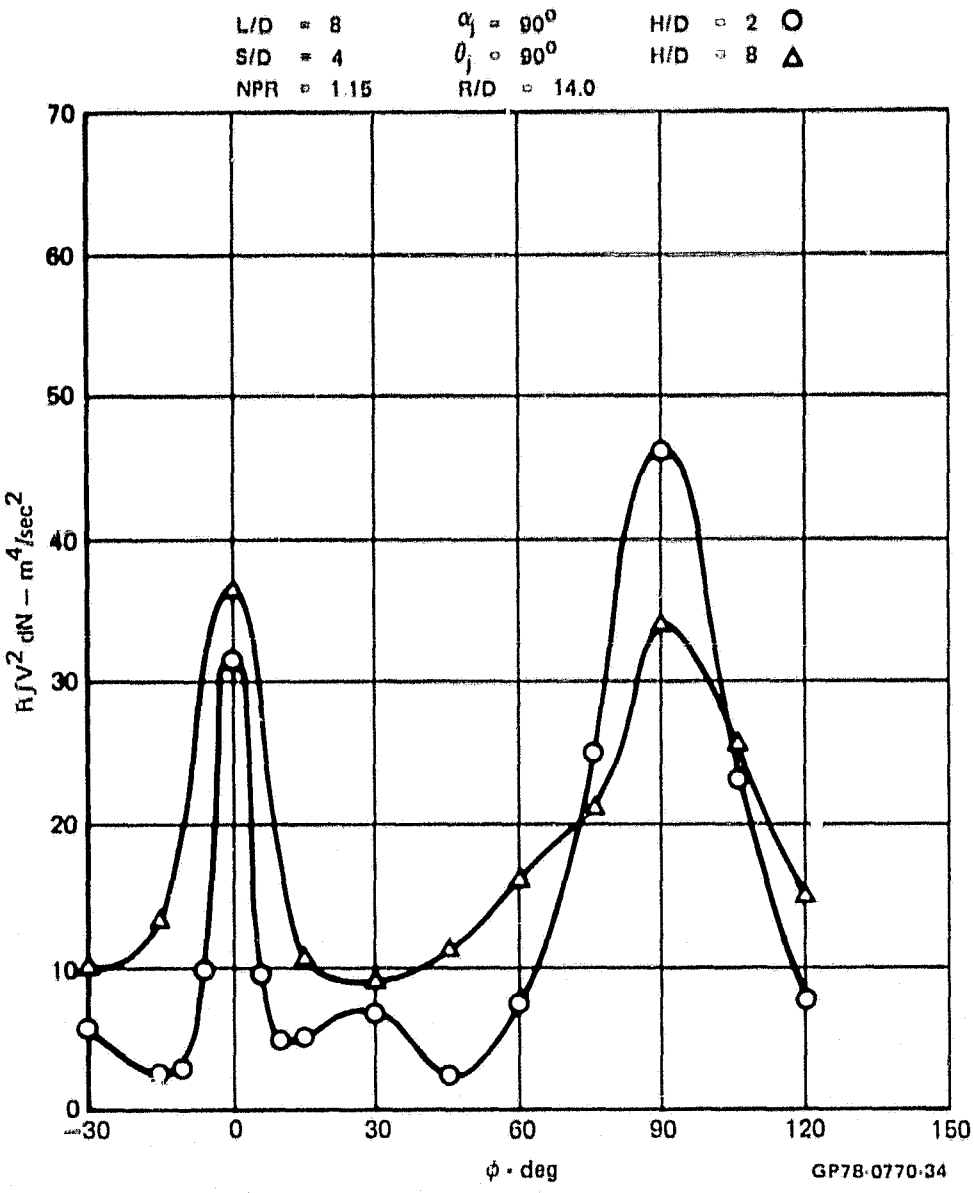

FIGURE 52

AZIMUTHAL DISTRIBUTION OF WALL JET RADIAL MOMENTUM FLUX

Vertical Impingement - Dual Jet

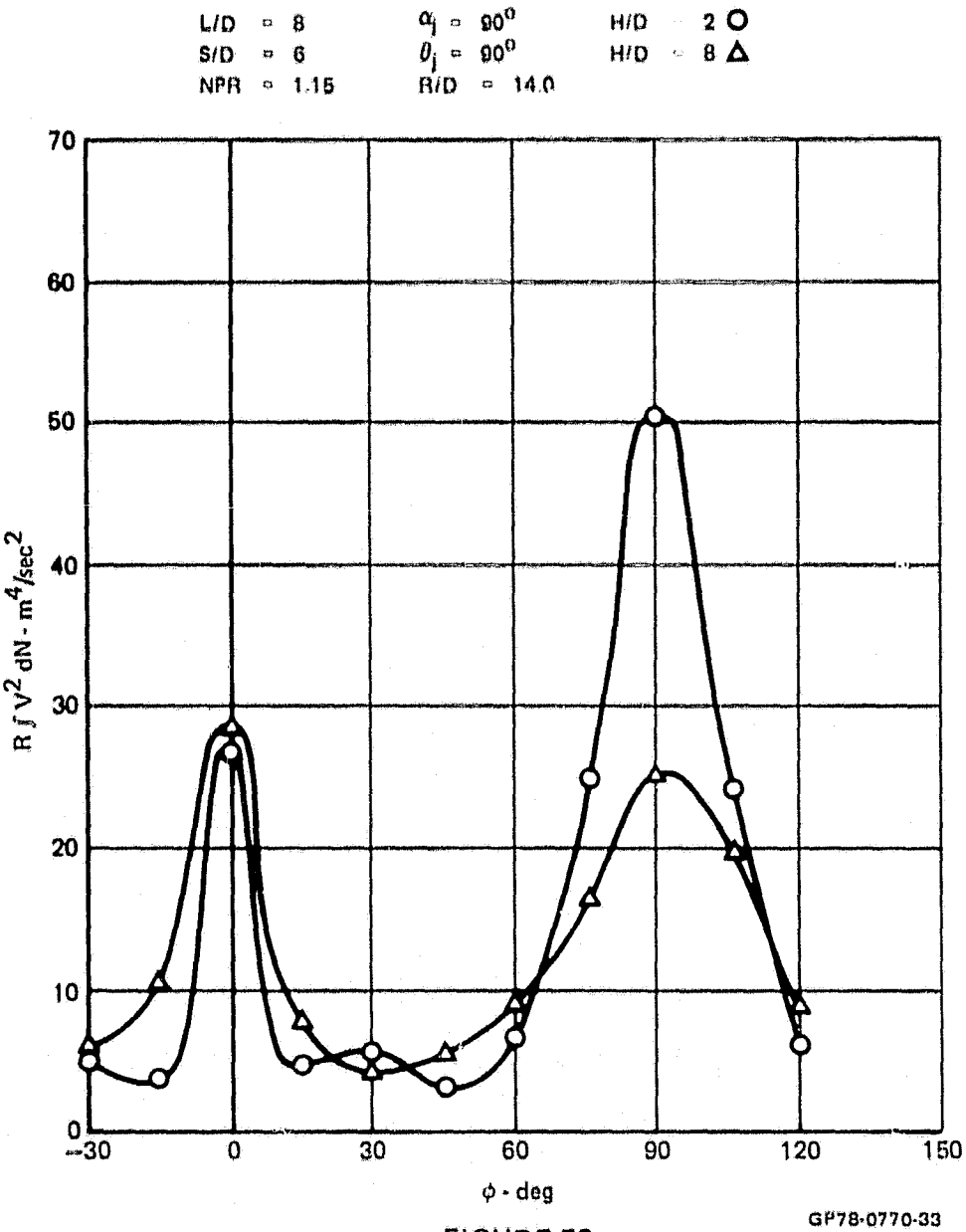

FIGURE 53

AZIMUTHAL DISTRIBUTION OF WALL JET RADIAL MOMENTUM FLUX

Vertical Impingement - Dual Jet

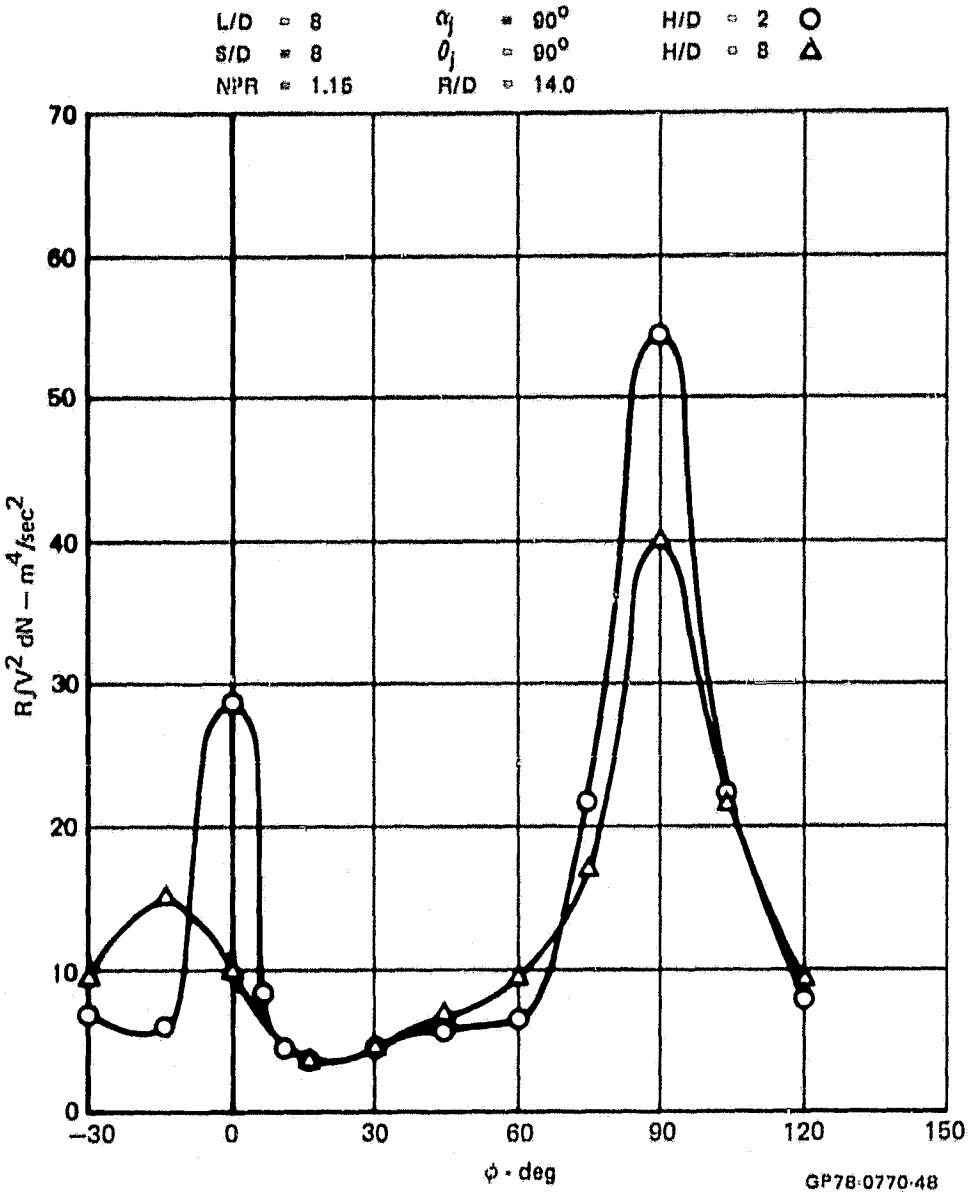

FIGURE 54
AZIMUTHAL DISTRIBUTION OF WALL JET RADIAL MOMENTUM FLUX
Vertical Impingement - Dual Jet

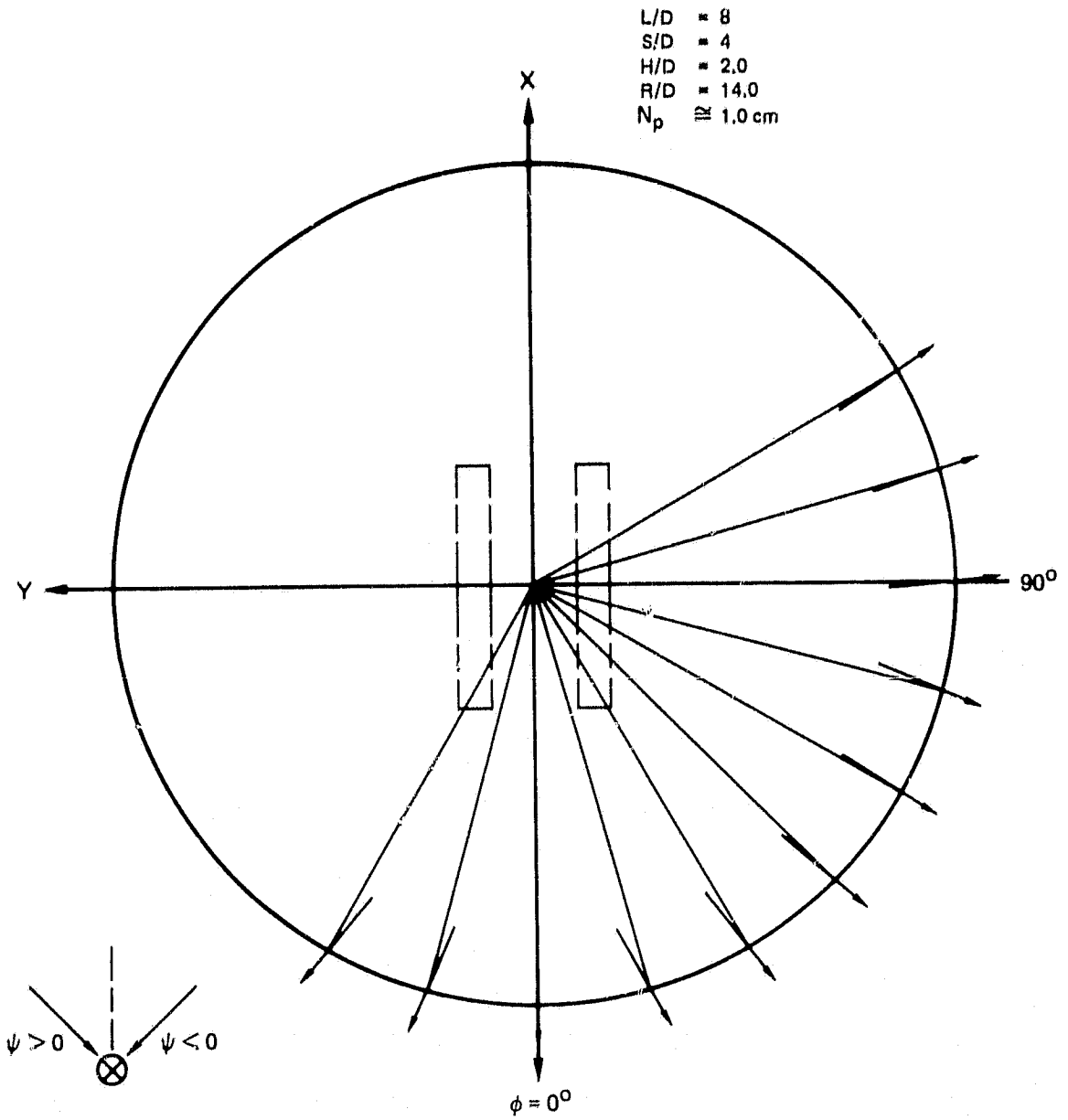

GP78-0770-23

FIGURE 55
DUAL JET YAW ANGULARITY

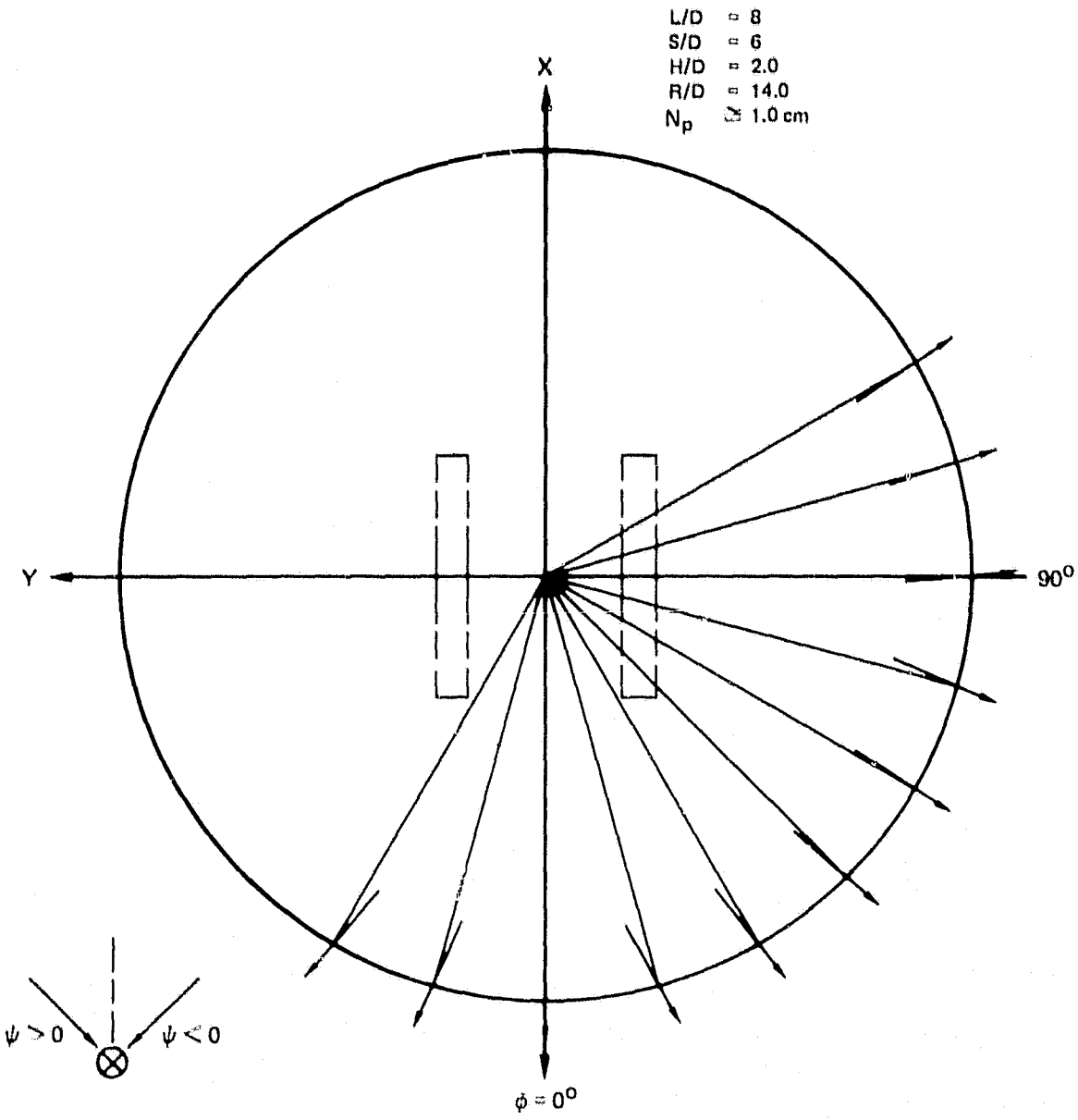

FIGURE 56
DUAL JET YAW ANGULARITY

GP78 0770-26

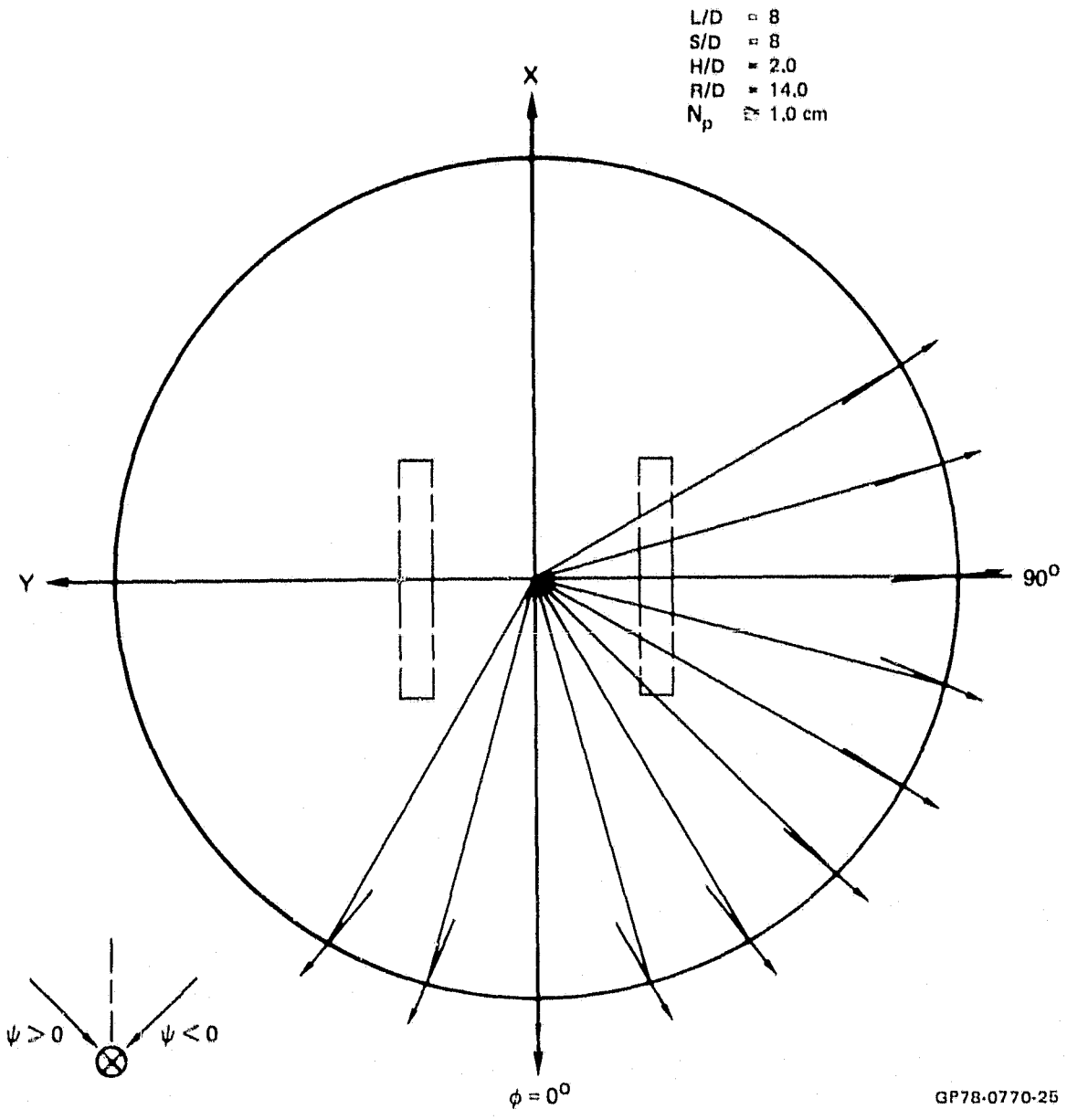

FIGURE 57
DUAL JET YAW ANGULARITY

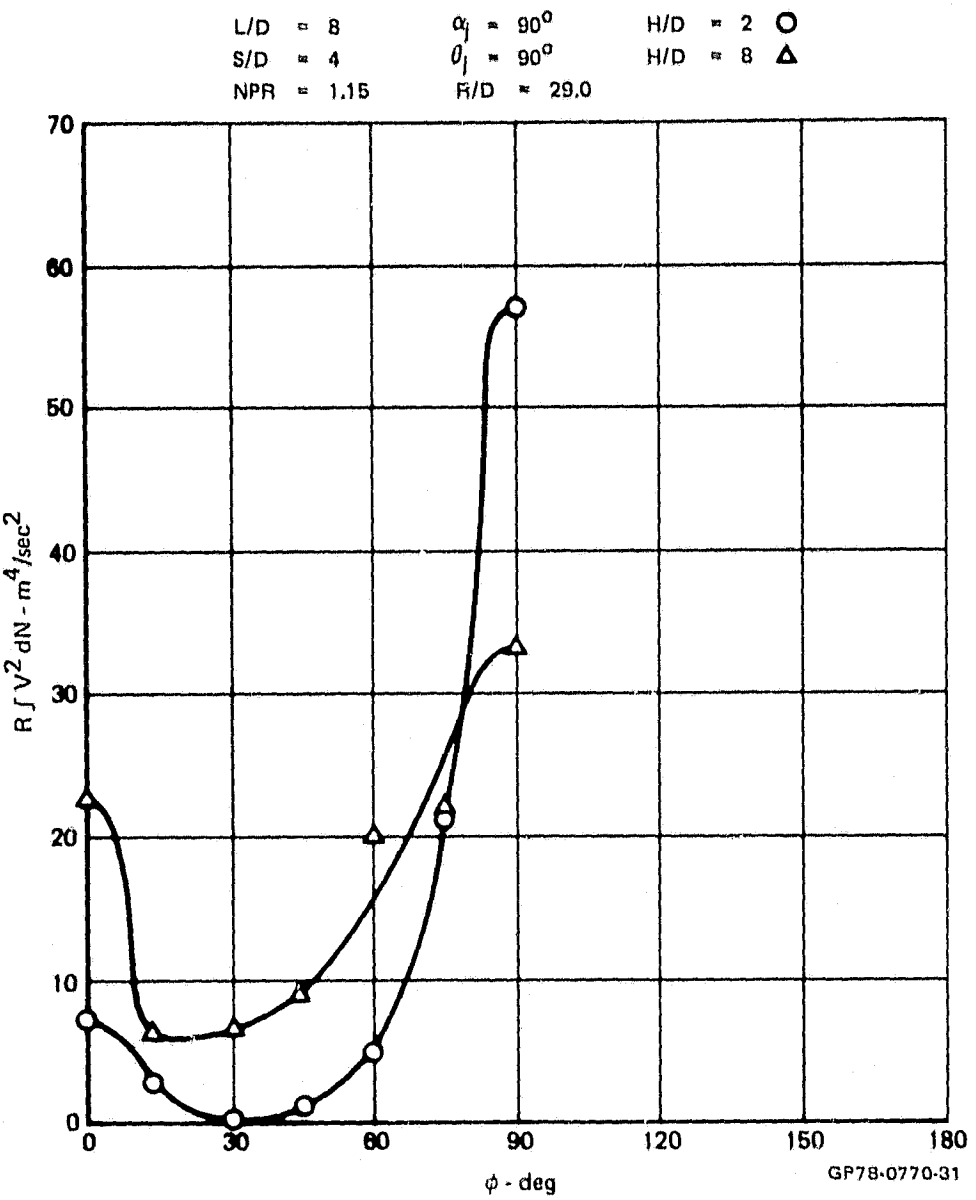

FIGURE 58

AZIMUTHAL DISTRIBUTION OF WALL JET RADIAL MOMENTUM FLUX

Vertical Impingement - Dual Jet

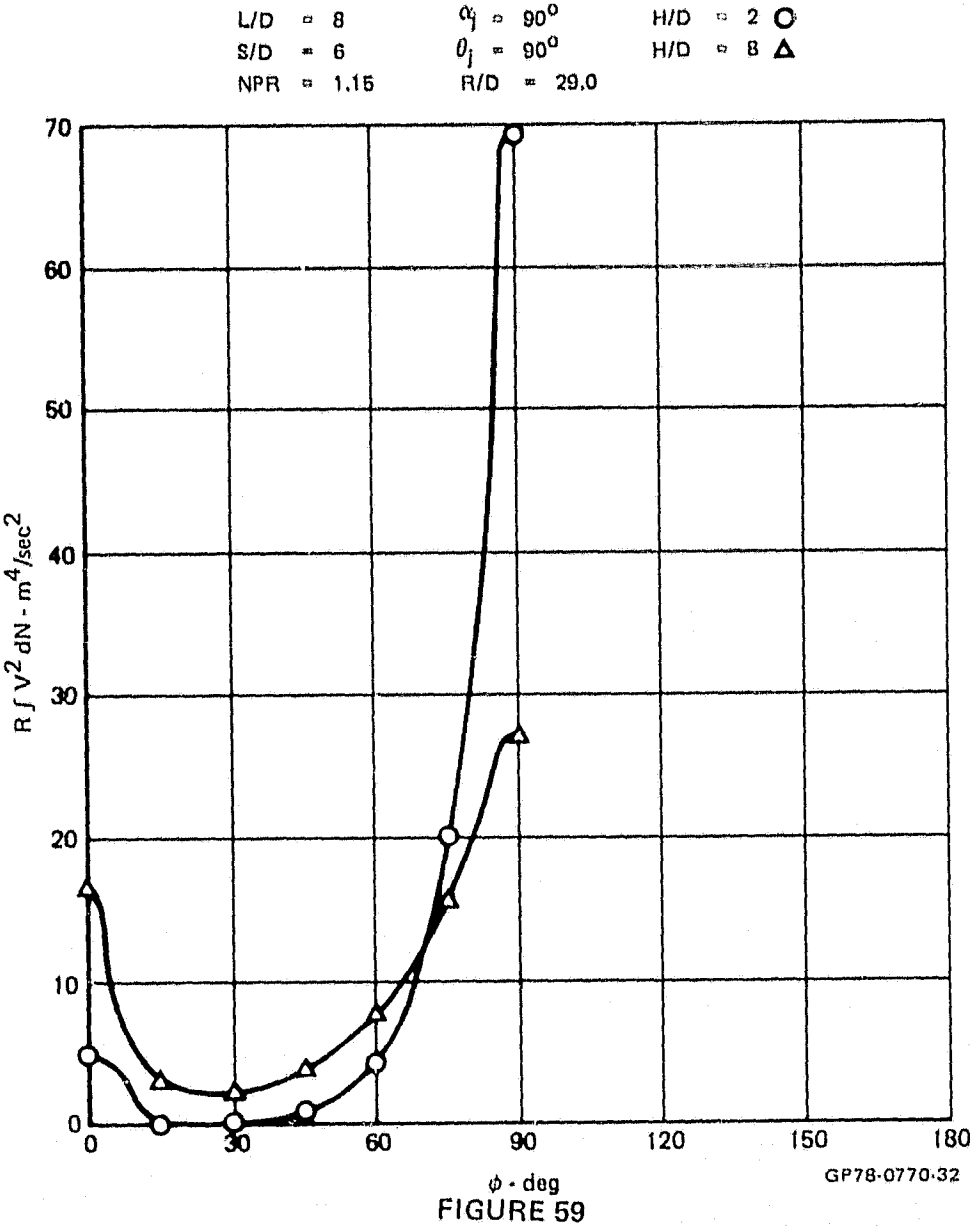

FIGURE 59

AZIMUTHAL DISTRIBUTION OF WALL JET RADIAL MOMENTUM FLUX

Vertical Impingement - Dual Jet

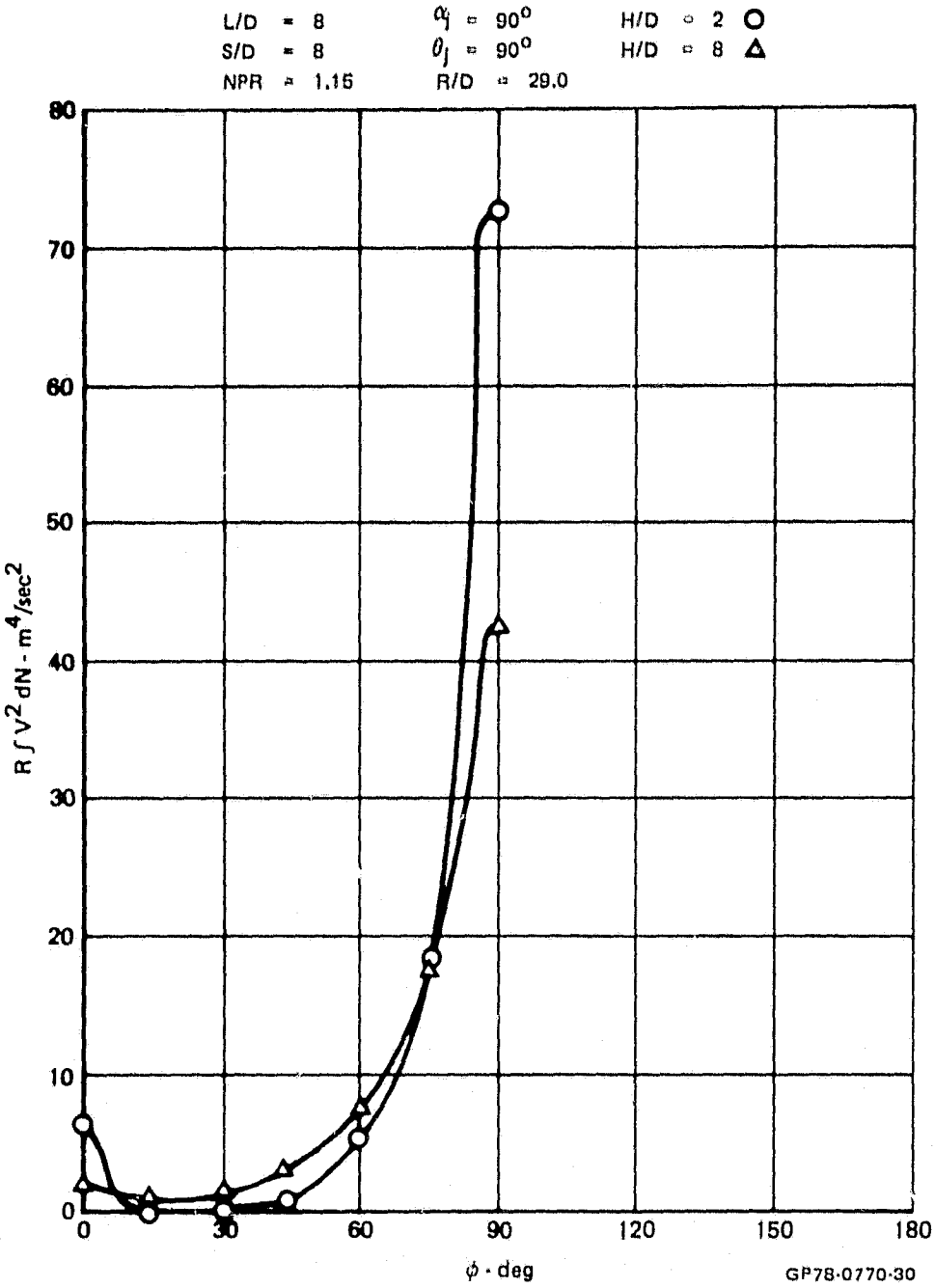

FIGURE 60

AZIMUTHAL DISTRIBUTION OF WALL JET RADIAL MOMENTUM FLUX

Vertical Impingement - Dual Jet

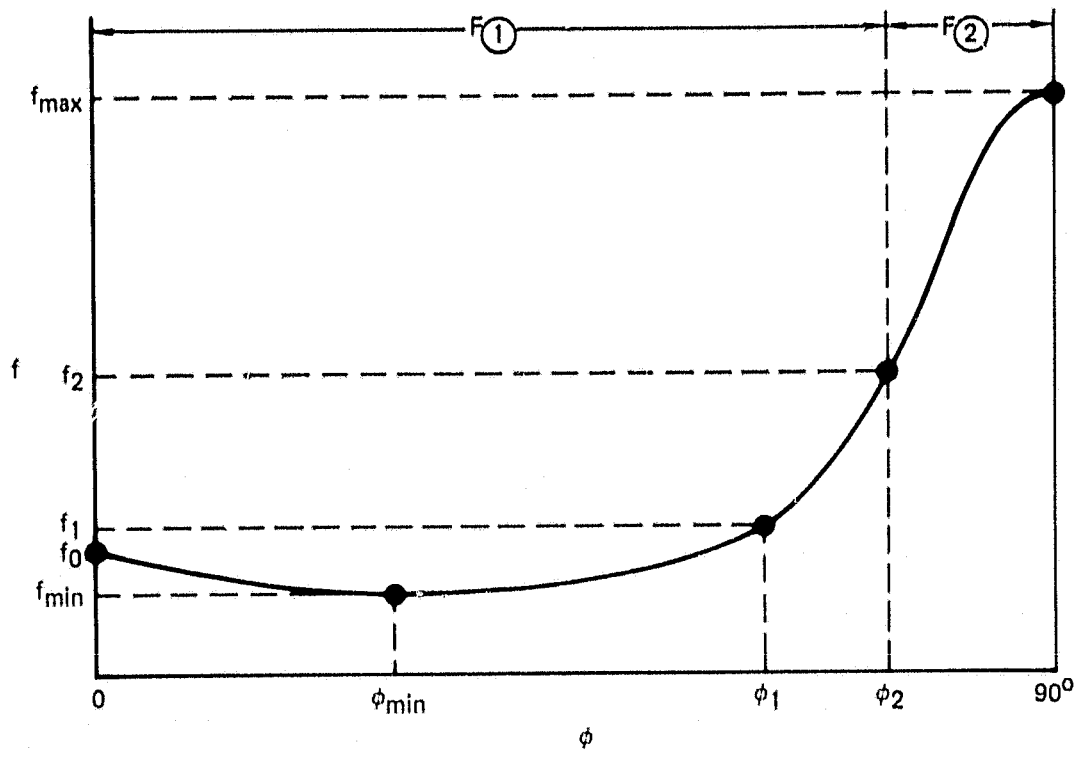

FIGURE 61
MOMENTUM FLUX DISTRIBUTION CURVE-FIT
Vertical Impingement

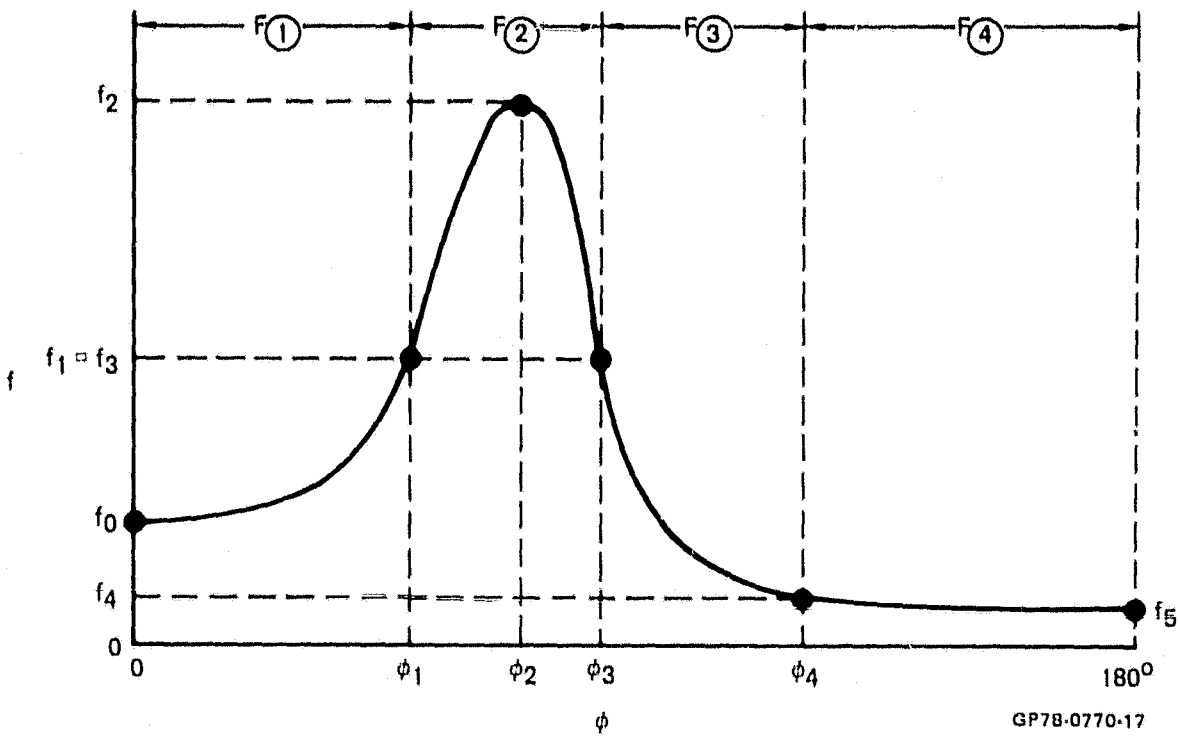

FIGURE 62
MOMENTUM FLUX DISTRIBUTION CURVE-FIT
Oblique Impingement - Pitch

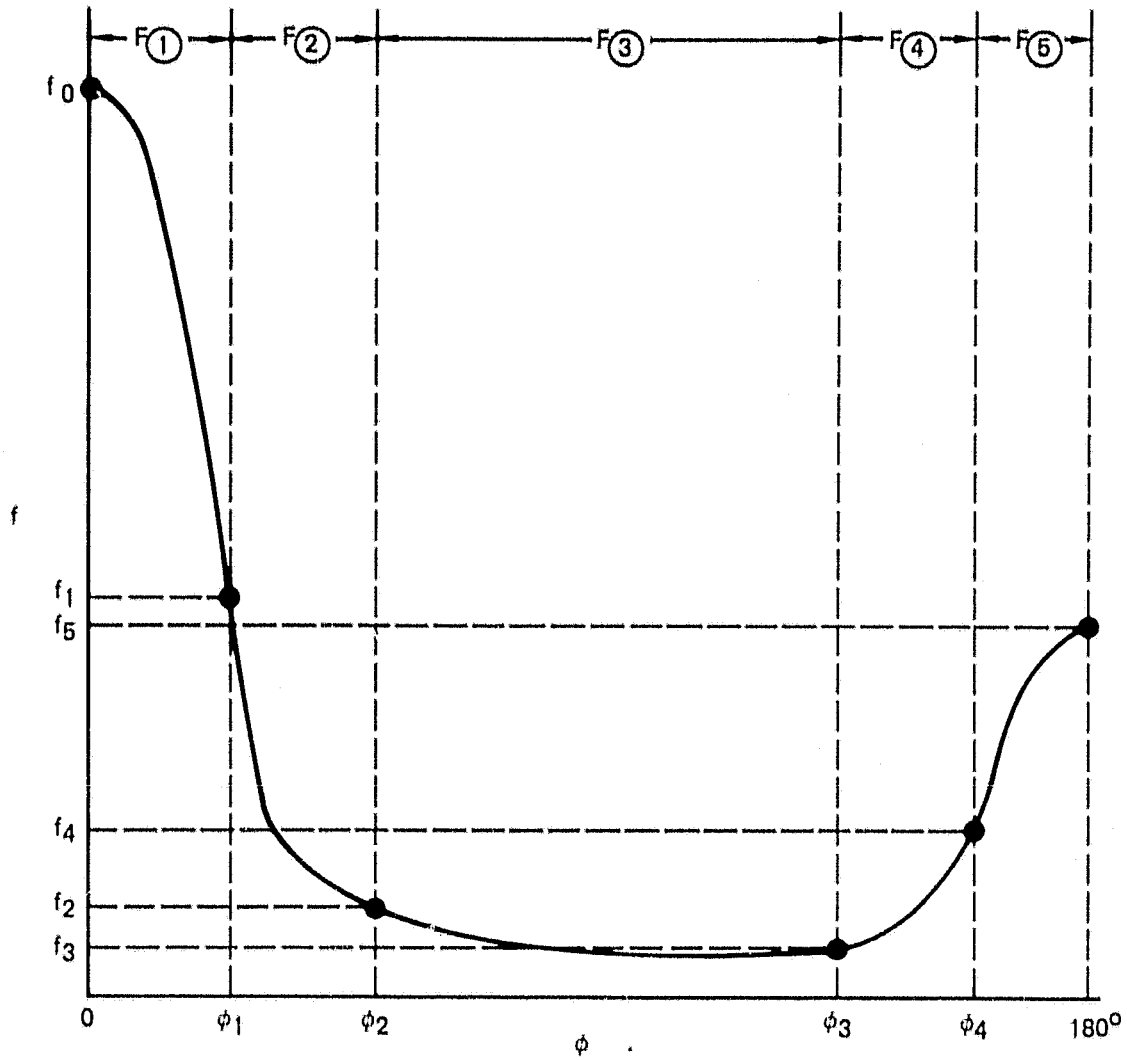

FIGURE 63

GP78-0770-18

MOMENTUM FLUX DISTRIBUTION CURVE-FIT

Oblique Impingement - Roll

REFERENCES

1. Walters, M., and Henderson, C., "V/STOL Aerodynamics Technology Assessment," Report No. NADC-77272-60, Naval Air Development Center, 15 May 1978.
2. Kotansky, D. R., Durando, N. A., Bristow, D. R., and Saunders, P. W., "Multi-Jet Induced Forces and Moments on VTOL Aircraft Hovering In and Out of Ground Effect," Report No. NADC-77-229-30, Naval Air Development Center, 19 June 1977.
3. Kleis, S. J., and Foss, J. F., "The Effect of Exit Conditions on the Development of an Axisymmetric Turbulent Free Jet," Third Year Technical Report, NASA Grant NGR 23-004-068, Michigan State University, 15 May 1974.
4. Donaldson, C. du P., and Snedeker, R. S., "A Study of Free Jet Impingement, Part I - Mean Properties of Free and Impinging Jets," Journal of Fluid Mechanics, Vol. 45, Part 2, pp 281-319, 1971.
5. Saunders, P. W., and Bristow, D. R., "Douglas Neumann Computations for Potential Flow About Arbitrary Three-Dimensional Bodies with Modifications for V/STOL Applications," McDonnell Douglas Corporation Report MDC A4707, 1 March 1977.
6. Ricou, F. P., and Spalding, D. B., "Measurements of Entrainment by Axi-symmetric Turbulent Jets," Journal of Fluid Mechanics, Vol. II, Part 1, p 21, 1961.